

Detection of Hydrothermal Systems on Mars using Remote Sensing

Dissertation

zur Erlangung des mathematisch-naturwissenschaftlichen Doktorgrades

“Doctor rerum naturalium”

der Georg-August-Universität Göttingen

vorgelegt von

Mohamed Ramy El Maarry

aus Kairo, Ägypten

Göttingen 2011

Bibliografische Information der Deutschen Nationalbibliothek

Die Deutsche Nationalbibliothek verzeichnet diese Publikation in der Deutschen Nationalbibliografie; detaillierte bibliografische Daten sind im Internet über <http://dnb.d-nb.de> abrufbar.

Referent: Prof. Dr. Andreas Pack

Korreferent: Dr. Walter Goetz

Tag der mündlichen Prüfung: 18.01.2011

ISBN 978-3-942171-43-4

uni-edition GmbH 2011

<http://www.uni-edition.de>

© Mohamed Ramy El Maarry



This work is distributed under a
Creative Commons Attribution 3.0 License

Printed in Germany

Contents

Summary	7
1 Hydrothermal Systems and Processes on Earth and Mars	9
1.1 Introduction	9
1.2 Hydrothermal fluids	9
1.3 Hydrothermal processes and Wall Rock alteration	10
1.4 Styles and types of hydrothermal alteration	11
1.4.1 Alkali metasomatism and Potassic alteration	11
1.4.2 Phyllic alteration	11
1.4.3 Argillic alteration	12
1.4.4 Propylitic alteration	12
1.4.5 Other types of alteration	13
1.5 Hydrothermal processes associated with meteorite impacts	13
1.6 Hydrothermal processes and systems on Mars	15
1.6.1 The planet	15
1.6.2 Evidence for hydrothermal activity on Mars	16
1.6.2.1 SNC meteorites	16
1.6.2.2 Spectral data	18
1.6.2.3 In-situ data from Landers: Mars Exploration Rovers (MERs)	19
1.6.3 Impact-generated hydrothermal (IGH) systems on Mars	20
1.7 Summary and thesis structure	21
2 Geochemical Studies through Gamma Ray Spectroscopy	23
2.1 Introduction	23
2.2 Case-Study: Impact-generated Hydrothermal Systems	23
2.2.1 Maps used	24
2.2.2 Results and discussion	24
3 Crater Floor Polygons on Mars	29
3.1 Preface	29
3.2 Introduction	29
3.3 Morphology and geographic distribution	31
3.3.1 Geographical distribution	35
3.3.2 Association with periglacial features	36
3.3.3 Terrestrial analogs	38

3.4	Mode of formation: thermal contraction in perma-frost vs. desiccation . . .	40
3.5	The physical model	41
3.5.1	Depth and spacing of tension cracks	41
3.5.2	Method of analysis	43
3.5.3	Results	45
3.6	Discussion	46
3.6.1	Crater paleolakes	46
3.6.2	Survey results	47
3.6.3	Formation mechanism and ages of crater lakes	50
3.7	Conclusions and outlook	51
4	Magmatic-Driven Hydrothermal System Case Study: Apollinaris Patera	55
4.1	Introduction	55
4.2	Geological, physiographical, and environmental settings of Apollinaris Patera	55
4.3	Criteria for locating hydrothermal systems on Mars	58
4.3.1	Action of liquid water	59
4.3.2	Evidence for magma/water interaction	62
4.3.2.1	Mounds	62
4.3.2.2	Possible lahars	71
4.3.3	Magmatic-driven tectonism	75
4.3.4	Craters with fluidized ejecta	75
4.3.5	Mineralogy: context and regional	76
4.3.6	Similarity to terrestrial analogs	80
4.4	Discussion	81
4.4.1	Possibilities for the past presence of a volcanic crater lake	81
4.4.2	Interfingering Apollinaris Patera and MFF materials	82
4.4.3	Implication for exobiology	86
4.5	Conclusion	86
5	Geophysical Investigations by Ground-Penetrating Radar (GPR)	89
5.1	Introduction	89
5.2	Methods and dataset	90
5.3	Results and discussions	93
5.3.1	Calderas of Apollinaris and Arsia	93
5.3.2	Fan deposits	93
6	Conclusions and Outlook for the Future	97
A	Space Instruments used in this Study	99
A.1	Compact Reconnaissance Imaging Spectrometer for Mars (CRISM)	99
A.2	Context Imager (CTX)	99
A.3	Gamma Ray Spectrometer (GRS)	100
A.4	High Resolution Science Experiment (HiRISE)	101
A.5	Mars Orbiter Laser Altimeter (MOLA)	101
A.6	Radar Sounders MARSIS and SHARAD	101

A.7	The Thermal Emission Imaging System (THEMIS)	102
B	Mapped CFPs	103
C	A Numerical Model for Formation of Giant Desiccation Polygons on Mars	115
C.1	Preface	115
C.2	Soil desiccation cracks: A review	115
C.3	Terrestrial analogs: Giant desiccation polygons	116
C.4	Modeling desiccation: principles and challenges	116
C.5	The prefracture model and results	117
D	Used Image Dataset for Apollinaris Study	123
	Bibliography	125
	Publications	149
	Acknowledgements	153
	Curriculum Vitae	155

Summary

This work introduces an interdisciplinary approach to search for hydrothermal systems on Mars. Through this approach, geophysical, geologic, geomorphologic, and mineralogic data are collected from various remote sensing instruments and combined to create tools for detecting magmatic-driven and impact-generated hydrothermal systems on Mars. Highlights of this work include:

- The first ever global mapping and description of polygonal features inside Martian impact craters, along with the production of analytical and numerical models to differentiate between these polygonal features and common permafrost polygons allowing for their identification as desiccation cracks that are remnants of mostly impact-generated paleolakes.
- The use of various remote sensing techniques to identify a volcanic site with high potential for magmatic-driven hydrothermal activity through the detection of evidence for surface venting, lahar events, water activity in the vicinity of the volcano, and possibly a volcanic crater lake.
- A correlation for the first time between the GRS water-equivalent hydrogen map in the mid-latitudes and a map of crater density to assess the role of impact events in forming hydrous minerals on Mars.
- A newly devised approach to look for surface/shallow subsurface manifestations of hydrothermal systems using low frequency ground-penetrating radar.

1 Hydrothermal Systems and Processes on Earth and Mars

1.1 Introduction

The study of hydrothermal systems on Earth and other planets is driven by both academic and economic interests. The understanding of the processes and conditions that drive hydrothermal systems is pivotal to the understanding of the geological, geochemical, and geophysical evolution of our planet (and others) through time. In addition, the ongoing observations of currently active and fossil systems is of interest to the biologists and exobiologists since these systems can be hospitable to certain life forms that thrive on the products and conditions of such systems. Finally, the end products of hydrothermal systems are usually of high economic (and sometimes strategic) value. Common hydrothermal ore deposits are characterized by an enrichment of metals such as iron, copper, molybdenum, tin, tungsten, lead, zinc, lithium, beryllium, gold and rare-earth elements. Hydrothermal systems develop wherever a fluid phase coexists with a heat source to drive convective energy loss. The fluid phase can be defined as a hot aqueous solution that is in chemical disequilibrium with its host rock(s) (Farmer 1996). Hydrothermal fluids alter, leach, transport and subsequently precipitate their primarily metallic mineral load in response to changes in physicochemical conditions. The solutes of hydrothermal systems are derived from primary (usually magmatic) and secondary (host rock) sources. An actively convecting hydrothermal system consists of a recharge system, a circulation cell, and a discharge system. Hydrothermal minerals are usually deposited at shallow depths in the crust along natural conduits, subsurface channels or fracture systems, and at sites of surface discharge.

Hydrothermal systems are active today in the oceanic and continental crusts, and their fossilized equivalents constitute a substantial portion of the geologic record. Although hydrothermal systems can be generated by many types of perturbations, there are two main types that will be described throughout this thesis: magmatic-driven and impact-generated ones. But before going into more detail about these two types, we first discuss some of the fundamental aspects of hydrothermal systems.

1.2 Hydrothermal fluids

The following discussion benefits greatly from the excellent textbook by Pirajno (2009). A hydrothermal fluid can be defined as a hot (≈ 50 to >500 °C) aqueous solution contain-

ing solutes that are commonly precipitated as the solution changes its properties through space and time. Fluids in general, and hydrothermal solutions in specific are subject to variations in temperature, pressure, and density, three key parameters which are needed to be known with a good deal of accuracy in order to understand the evolution of the hydrothermal processes. The water of hydrothermal solutions can be derived from many sources such as seawater, meteoric (rain, lakes, rivers, ground water, snow, etc), connate, metamorphic, and magmatic. Most solutions have a mixed origin in which one of the previous sources may dominate. Seawater dominates mainly in marine environments around mid-ocean ridges and subduction zones. Meteoric sources predominate at continental environments and around subareal volcanoes. The other sources have generally a lesser influence which can be rather significant in certain settings. Connate sources are waters that get trapped during the deposition of sediments and are produced during the diagenetic reactions. Metamorphic waters are derived from the dehydration of water-rich minerals through rising temperatures and pressures. Finally, magmatic waters are those that separate from melts upon cooling, generating a magmatic/hydrothermal system, which is perhaps one of the most significant ore-forming agents. Water is usually the dominant volatile in a hydrothermal system but is rarely the only one. Other important volatile constituents include H_2S , CO_2 , SO_2 , SO_4^{2-} , H_2 , HCL , B , and F . Finally, where older models for hydrothermal systems have concentrated on aqueous fluids as being the main player in the formation of hydrothermal deposits (e.g. Burnham's model, Burnham 1979), recent models (e.g. William-Jones and Heinrich 2005), have drawn attention to the leading role of magmatic vapors as opposed to a liquid phase in forming many hydrothermal ore deposits. Such models are based on extensive experimental studies on the stability of metallic species in aqueous vapors.

1.3 Hydrothermal processes and Wall Rock alteration

A hydrothermal system consists of two main components: a heat source, which provides the necessary energy (magmatic, geothermal gradient, radiogenic decay, metamorphism), and a fluid phase as discussed in the previous section. An actively convective hydrothermal cell consists of: a recharge system, a circulation cell, and a discharge system. Hydrothermal deposits are usually formed at the discharge sites such as faults, fracture networks, and shear zones. The rocks within which the deposits are formed undergo varying degrees of hydrothermal alteration, with an intensity decreasing with distance from the discharge site.

Hydrothermal alteration is a complex process involving mineralogical, chemical and textural changes (Pirajno 2009). In essence, hydrothermal fluids chemically attack the mineral constituents of the wall rocks, which tend to re-stabilize by forming new minerals that are in chemical equilibrium with the new conditions. The process is a form of metasomatism, and as such, it is likely that the hydrothermal fluid itself changes chemically through its contact with the wall rocks. A common parameter used to describe the intensity of the interaction is water/rock ratio (W/R) which is defined as the total mass of water that passes through the system in a unit time, divided by the total mass of rocks in the considered system. In hydrothermal systems, W/R ratios may range from 0.1 to 4 (Pirajno 2009).

1.4 Styles and types of hydrothermal alteration

Many styles and types of hydrothermal alteration exist. To a first approximation, the nature and relative quantities of minerals that constitute various alteration assemblages depend on five factors: (1) temperature, (2) pressure, (3) host rock composition, (4) primary fluid composition, and (5) the W/R ratio (Reed 1997). The most significant types in order of higher temperatures and pressures to lower ones are alkali metasomatism, propylitic, phyllic, and argillic alterations. Understanding the way different alteration schemes affect the final mineral assemblages in a hydrothermal system can add better constraints on the type of minerals to look for by remote sensing techniques in order to detect hydrothermal systems.

In general, the effects produced on the wall rocks by interaction with and the chemical changes in a hydrothermal fluid depend on variations in the aK^+/aH^+ ratio of the system (Pirajno 2009); i.e. the activities of the K^+ and H^+ ions. This ratio decreases as the system moves towards lower temperatures and pressures. In other words, alteration process change from alkalic to argillic with increase of H^+ metasomatism (the process by which water decomposes to H^+ and OH^- ions which are consumed back and forth between the hydrothermal fluids and the host rocks). We further investigate these processes below.

1.4.1 Alkali metasomatism and Potassic alteration

Alkali metasomatism is usually associated with early high temperature fluids in the range of 800-600°C, which are derived from a melt in its late stages of crystallization. Processes in this range include Base Exchange (reactions where a cation is replaced by another in a mineral), changes in the structural state of feldspars, albitisation, microclinasation, and growth of tri-octahedral micas (Pirajno 2009). An example of this reaction type would be replacement of Ca-plagioclase by Na-plagioclase (Na metasomatism) or replacement of plagioclase by K-feldspar and biotite (K-metasomatism, Requía and Fontboté 1999). Potassic alterations however can occur at lower temperatures (600-450 °C). Typical mineral assemblages of that type are orthoclase (or adularia), biotite, quartz \pm albite \pm chlorite \pm anhydrite \pm pyrite.

1.4.2 Phyllic alteration

Phyllic (or sericitic) alteration is characterized by the assemblage quartz-sericite-pyrite. Phyllic alteration is one of the most common types of hydrothermal alteration, as it is present in almost all hydrothermal mineral deposits. This alteration grades into alkali-potassic type by increasing the amount of K-feldspars and/or biotite, and into argillic type by increasing the amount of clay minerals. Usual associated minerals are K-feldspar, kaolinite, calcite, biotite, rutile, anhydrite, and apatite. Phyllic alterations have long been thought to form as a result of mixing of lower temperature and salinity magmatic fluids with meteoric water (e.g., Reynolds and Beane 1985, Taylor 1997). However, more recent work by Harris and Golding (2002) has challenged this notion by concluding through analysis of porphyry¹Cu-Au deposits in Australia that the alteration assemblages are mainly, if not exclusively, related to magmatic fluids that become colder and less saline

after creating the potassic and argillic alteration zones.

1.4.3 Argillic alteration

Argillic alteration is characterized by the formation of clay minerals due to intense H^+ metasomatism and acid leaching, at temperatures between 100 and 300°C. This alteration grades inwards into phyllic and outwards to propylitic. This type of alteration is common in both porphyry and epithermal systems. Clay minerals principally replace the plagioclases and mafic silicates (hornblendes, biotite). Amorphous clays, such as allophane, are also present and replace aluminosilicate phases. The usual mineral assemblages depend on whether the alteration is termed intermediate or advanced.

Intermediate argillic alteration is defined by the presence of montmorillonite, illite, chlorite, kaolin group minerals (kaolinite, halloysite, dickite, hallophane). K-feldspar is basically kept unaltered. Zoning within the intermediate argillic alteration may be present with kaolinite being closer to the phyllic zone, whereas montmorillonite clays occur in the outer zones. Basically, this alteration yields an altered rock depleted in Ca and Na.

Advanced argillic alteration occurs due to intense acid attack, and is characterized by more or less complete leaching of the alkali cations with complete destruction of the feldspars and mafic silicate phases. Main assemblage includes pyrophyllite, kaolinite, dickite, quartz, barite, alunite, and sulfides. Alunitic alteration is one of the minor types of advanced argillic alteration which can become significant, even dominant in the presence of abundant sulfate ions and Al-rich protoliths (e.g. Lerouge et al. 2006) yielding alunite, natroalunite (Na replacing K) and jarosite (Fe replacing Al).

1.4.4 Propylitic alteration

In volcanic and plutonic rocks, low temperature (200-350 °C) alteration at small W/R ratios yields a propylitic assemblage that includes albite, chlorite, and epidote (Reed 1997). Propylitic alteration is characterized by addition of H_2O and CO_2 , and locally S, with no appreciable H^+ metasomatism. Additional minerals that can be found are carbonates, sericite, montmorillonite and zeolites (e.g., Melling et al. 1990). The assemblage matches the classical greenschist metamorphic assemblage. Finally, the key distinction of propy-

¹Economic geologists describe hydrothermal deposits by many names depending on many factors such as the chemical composition, mode of placement, temperature of formation, depth, etc. However, the more common names are porphyry, epithermal, and fumarolic deposits.

Porphyry deposits occur within large bodies of intrusive felsic to intermediate igneous rocks. The host intrusions are typically emplaced at relatively shallow depths of 0.5-3 km and crystallize rapidly - leading to the porphyritic textures (origin of the name). The hydrothermal fluids separate out from the crystallizing magma and their high water and vapor pressures cause abundant shattering of both the intrusive and the country rocks around it; the fractures, often hairline cracks, are then mineralized in a well-zoned pattern. Typical formation temperatures are between 250 and 500 °C. The most famous example of these deposits are the Cu-porphyry deposits.

Epithermal deposits are products of volcanism-related hydrothermal activity at shallow depths (1 -1.5 km from the surface) and low (50 to 200 °C) temperatures. The deposits are usually found in the form of veins, and irregular branching fissures. Finally, fumarolic deposits are surficial deposits that are found associated with fumaroles due to the interaction of fumarolic gases such as H_2S , CO_2 , and SO_2 with groundwater and the wall rocks.

litic alteration is that its mineral assemblages reflect those of the primary host rock, not the fluid since this is usually the outermost zone of alteration.

1.4.5 Other types of alteration

There are other less common but significant types of hydrothermal alteration that are encountered in several types of hydrothermal systems such as serpentinization, hematitization and Fe alteration, dolomitization and carbonitization. Serpentinization for example is one of the most common types of alteration of ultramafic rocks. Serpentine minerals (antigorite, chrysotile and lizardite) are formed from olivine and pyroxene by introduction of H₂O and CO₂ with an exothermic reaction. The temperatures of serpentinization processes range from as low as <100 °C for lizardite, to as high as 500 °C for antigorite. Common mineral assemblage is serpentine + brucite ± magnetite.

1.5 Hydrothermal processes associated with meteorite impacts

While most of the hydrothermal systems on Earth are magmatic-driven, another mechanism, which can create and sustain a hydrothermal system, is meteorite impacts. Impact-generated hydrothermal (IGH) systems occur when a high velocity bolide hits a water rich target. A fraction of the kinetic energy of the bolide is transferred to the target material in the form of heat. The high pressures (>100 GPa) and temperatures (>1600 °C) associated with the impact event can cause the melting of part of the target material leading to a melt sheet. As soon as the temperature of this melt sheet drops to 500-600 °C, a hydrothermal system can initiate assuming the presence of water in the vicinity of the impact crater. The thermal energy transferred into the target rocks causes thermal perturbations and heat release particularly in the central structural uplifts, which bring near the surface deeper and hotter crust. These thermal effects result in a spectrum of phenomena from partial melting to high-temperature metamorphism and hydrothermal fluid flow. In general, the transformation of kinetic energy into heat takes place at sub-crater levels, where hydrothermal circulation would be focused, although IGH circulation can extend well below the crater floor to depths of several kilometers (Komor et al. 1988). It is also likely that hydrothermal fluids can vent at the surface as hot springs or geysers, forming silica rich deposits (Newsom 1980). To date, evidence for IGH activity is known from more than 60 terrestrial craters (Naumov 2005), and many of these have been extensively studied such as Sudbury, Canada (Molnár et al. 1999), Chicxulub, Mexico (Zuercher and Kring 2004), Ries, Germany (Newsom et al. 1986), Puchezh-Katunki, Russia (Naumov 2002), Kardlâ, Estonia (Versh et al. 2005), and Lonar, India (Hagerty and Newsom 2003).

Evidence of IGH activity usually includes: (1) occurrence of secondary mineral assemblages (e.g. ore-forming minerals), (2) chemical alteration of materials at the impact site, and (3) occurrence of fluid inclusions in hydrothermal mineral phases and in shock-generated deformation features (Naumov 2005). Alteration minerals have been observed in terrestrial craters 1.8-300 km in diameter. Hydrothermal minerals occur both in shocked and disturbed target rocks beneath the crater floor (authigenic breccias, Figure 1.1) and within thick layers of impact-melt rocks, lithic breccias in the crater, and in the

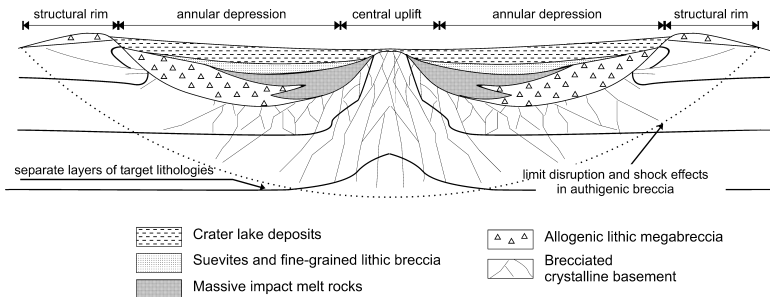


Figure 1.1: Schematic cross-section of a complex impact crater. The distribution of main impact lithologies within the crater is shown. Adapted from Naumov (2005).

crater lake sediments (if one existed). Alteration is best developed in craters where suevites dominate the impact-melt rocks; in these craters, secondary minerals can contribute up to 10-25% of the impact rocks. In craters where massive impact melting occurs, hydrothermal alteration products do not exceed 1-2% of the impact rocks. The degree of dissemination of the impact melt (and, consequently, the formation of either massive or fragmental "suevite" impact melt rocks) is mainly determined by water content in the target (Kieffer and Simonds 1980). Thus, the intensity of hydrothermal alteration is determined by paleogeographic characteristics of the target, that are responsible for both the production of specific impact lithologies which differ in their permeability and reactivity towards hydrothermal fluids, and for the amount of fluids present within impact rocks.

In large (diameter approximately 50 km) craters, secondary mineralization extends down to 5 km in the central uplift and it embraces the entire annular depression (Naumov 2002). Based on this situation, the volume of the circulation cells that may develop could reach 600-1000 km³. This is confirmed by data from the Siljan impact structure (55 km diameter) where impact-generated fluid inclusions (Komor et al. 1988) occur within a rock volume of 800 km³. Based on data from well-studied impact structures, the similarity in hydrothermal mineral associations in the majority of terrestrial craters is apparent. The dominant hydrothermal assemblage is clay minerals (smectite, chlorite, and mixed-layered smectite-chlorite), various zeolites, calcite, and pyrite. In addition, cristobalite, quartz, opal, anhydrite, gypsum, apophyllite, prehnite, epidote, andradite, ferrosalite, actinolite, and albite occur locally. If carbonate rocks are significant in the target, the carbonate-quartz-sulphide association is also widespread.

Combining mineralogical, geochemical, fluid inclusion, and stable isotope data, the distinctive characteristics of IGH fluids were summarized by Naumov (2005) as follows:

- Fluid circulating in the post-impact hydrothermal systems is derived from superficial reservoirs, including lakes or marine basins developed in crater depressions, trapped pore waters and, possibly, products of dehydration and degassing of minerals under shock.
- Fluid temperatures vary from ambient to 350-400 °C.

- Moderate to high rates of filtration (10^{-4} to 10^{-3} m s $^{-1}$) are typical.
- Low salinity and predominantly aqueous composition of fluids. P_{CO_2} values are usually low.
- Hydrothermal solutions are weakly alkaline to near-neutral (pH 6-8) and are supersaturated in silica during the entire hydrothermal process because of the strong predominance of shock-disordered aluminosilicates and fusion glasses in the host rocks. These factors create favorable conditions for the formation of Fe-smectites and zeolites which are the main minerals in the hydrothermal column.
- Mineralogical and geochemical features of impact-generated hydrothermal processes are governed by a combination of both the chemical composition of target and the conditions of the host rock as a result of shock metamorphism.
- From the general succession of mineral crystallization, a uniform retrogressive course of hydrothermal processes is indicated.

In conclusion, products of impact-generated hydrothermal processes are similar to the hydrothermal mineralization in volcanic areas, as well as in modern geothermal systems, because thermodynamic and hydrodynamic conditions are similar. However, the sequence of post-impact minerals formed in a single event by the gradually decreasing temperature is distinct from that in endogenic hydrothermal systems.

1.6 Hydrothermal processes and systems on Mars

1.6.1 The planet

Mars is a terrestrial-type planet that lies fourth from the Sun with a diameter of 6371 km (about half that of Earth), an axis inclined at 25° to the ecliptic and a 24 hours and 40 minutes day. Consequently, Mars has seasons similar to Earth, but with a thin (atmospheric pressure = 6 mbar on average), CO₂-rich atmosphere. While Mars is known to have captivated the human imagination since the dawn of history, it was not until the first images of Mars were acquired by the Mariner flybys in the 1960s, and then the Viking missions (1, and 2) in 1976, that the surface features of Mars were shown with clarity and the geological richness of its surface was revealed.

Today, Mars is geologically mostly inactive, although the range of features on the surface such as valley networks, rift valleys, volcanic edifices, and sedimentary features attests to a more active past. On the basis of its impact cratering size-frequency record, an approximate geological time scale for Mars is subdivided into three main periods: the Noachian (4.6-3.6 to 3.5 Ga), the Hesperian (3.5-2.9 Ga), and the Amazonian (2.9 Ga-present). The Noachian period is characterized by the formation of the northern lowlands and large impact basins such as Hellas, Argyre, and Isidis in addition to the early Tharsis tectonic-thermal activity, and the valley networks in the southern highlands (Figure 1.2). In the Hesperian period, significant volcanism occurred in the Tharsis, Elysium and Syrian regions. In addition, Valles Marineris rift system, and major outflow channels were formed. Other volcanic centers of this period are characterized by a morphology of

low-lying edifices, suggesting magma-water and/or ice interactions and explosive eruptions (Head and Wilson 2002). At least three major trends characterize the Hesperian period (Head and Wilson 2002): (1) change from regional to local volcanism and associated decrease in magmatism; (2) decrease in heat flux and a corresponding increase in the cryosphere thickness; and (3) large water movement with formation of the outflow channels, breaching of the cryosphere and transfer of water from the subsurface to the surface. During the Amazonian both tectonism and volcanism decreased in the Tharsis and Elysium regions and there was a change of style of volcanic eruptions from explosive to more effusive. The Amazonian is also characterized by late phases of channel formation, aeolian activity, and formation of the layered polar deposits.

1.6.2 Evidence for hydrothermal activity on Mars

It is likely that, similar to Earth, the geologic record of Mars includes impact-generated (Newsom 1980, Rathbun and Squyres 2002, Abramov and Kring 2005) and magmatic-driven (Dohm et al. 1998, 2008, Schulze-Makuch et al. 2007) hydrothermal activity. This is deduced from the widespread occurrence of impact, volcanic, and water-related features on the surface, which are often temporally and spatially associated. Martian surfaces of different ages, for example, exhibit hydrological features such as large outflow channels (Baker and Milton 1974), valley networks (Scott et al. 1995), gullies and debris aprons (Malin and Edgett 2001), polygonal-patterned ground (Kargel 2004, Levy et al. 2009, El Maarry et al. 2010), glaciers (Kargel and Strom 1992), rock glaciers (Mahaney et al. 2007), deltas (Ori et al. 2000a, Malin and Edgett 2003, Pondrelli et al. 2008, Di Achille and Hynes 2010), and possible water bodies ranging from lakes to oceans (Scott et al. 1995, Fairén et al. 2003, Di Achille et al. 2006, Dohm et al. 2009a), all of which indicate that Mars had liquid water on its surface at some time during its history, perhaps for considerably long periods. Associated with this diverse and extensive evidence of Martian aqueous activity, is the ubiquitous presence of impact craters (Barlow and Bradley 1990) and massive magmatic complexes such as Tharsis and Elysium, along with their related tectonic features (e.g., Anderson et al. 2001, 2008) in addition to other diverse evidence of volcanism (e.g., Hodges and Moore 1994). Both landforms often interact in space and time (Carr 1979, Newsom 1980, Mouginiis-Mark 1990, Tanaka et al. 1998, Dohm et al. 2001a,b) which is expected to have produced widespread hydrothermal activity on Mars. In the following sections, we look at more direct and indirect evidence for hydrothermal activity on Mars.

1.6.2.1 SNC meteorites

The earliest evidence for hydrothermal activity on Mars derives from studies of Martian SNC meteorites (SNC standing for shergottite, nakhlite, and chassignite; the three main classes of Martian meteorites). Most of these meteorites comprise a geochemically and isotopically related group that have bulk compositions similar to terrestrial basalts (McSween 1994). With the exception of the ALH84001 meteorite that has a crystallization age of ≈ 4.5 Ga, the SNCs are geologically young, falling within the range 1.3-0.18 Ga. Gooding (1992) showed that the SNC meteorites contain trace quantities (<0.01 wt%) of primary hydrous minerals, including amphiboles and micas contained within glassy

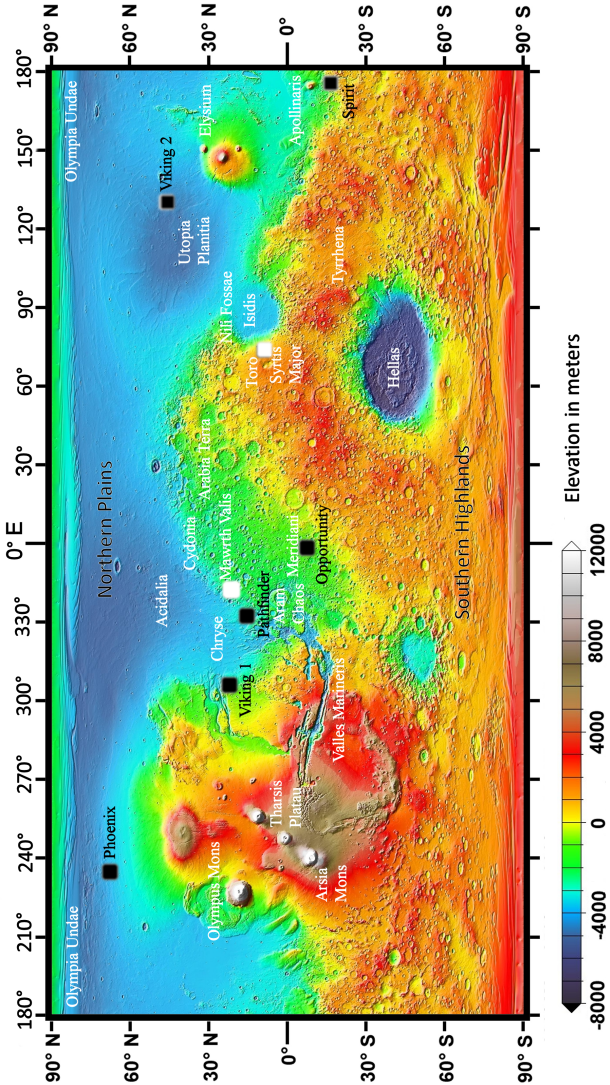


Figure 1.2: A typical Mars elevation map highlighting some of the significant features on the surface, locations of interest that will be discussed in later sections, and locations of all successful lander missions to date.

inclusions of primary igneous origin, as well as post-crystallization aluminosilicates, carbonates, sulfates, halides and ferric oxides formed through interactions with late stage aqueous solutions. The post-crystallization assemblage indicates that oxidizing, hydrous solutions were present in the Martian crust (or some parts of it) sometime after 0.18 Ga. In addition, the analysis of carbonate spherules in ALH84001 suggests that they formed at elevated temperatures from groundwaters that readily interacted with atmospheric reservoirs (Romanek et al. 1994). Plausible mechanisms for the formation of such spherules include hydrothermal systems associated with intrusive bodies, or large impacts (Jakosky and Jones 1994).

1.6.2.2 Spectral data

Mineralogical mapping on Mars was conducted at first by TES, a thermal- mid-infrared spectrometer onboard the Mars Global Surveyor (Christensen et al. 2004a), and OMEGA, a hyperspectral imager on board the Mars Express (Bibring et al. 2004). These were later improved upon by the CRISM instrument (Murchie et al. 2007) on board the Mars Reconnaissance Orbiter. We highlight their major findings related to possible hydrothermal processes (see Appendix A for more information on the instruments used in this study). One of the first discoveries of potentially hydrothermal deposits was reported by Christensen et al. (2004b) using data from TES of coarse-grained grey hematite deposits in two regions on Mars: Sinus Meridiani, and Aram Chaos (refer to Figure 1.2 for locations mentioned in this study), both associated with sedimentary deposits. Christensen et al. (2004b) discussed numerous mechanisms for formation and concluded that the deposits "most likely formed by chemical precipitation from aqueous fluids under either ambient or hydrothermal conditions".

Later, the OMEGA team identified olivine-rich surfaces in crater floors and rims around Syrtis Major and in craters with diameters <20 km in their lobate ejecta in the northern plains (Bibring et al. 2005, Poulet et al. 2005). Sulfate minerals, probably gypsum and possibly bassanite were detected in the north polar regions, correlating with the dark dune fields of Olympia Undae (Langevin et al., 2005). Absorption bands corresponding to other sulfates, kieserite and epsomite, in addition to gypsum, were also found in the light-toned layered deposits of Valles Marineris, Margaritifer Terra, and Meridiani (Gendrin et al. 2005). Such massive sulfate deposits could have been produced by magmatic-sourced S-rich hydrothermal fluids. The OMEGA team also identified water-bearing phyllosilicates scattered in many regions on Mars that are generally dated as Noachian terrains. The identified species include Fe-rich smectites, Fe/Mg chlorite, chamosite, and montmorillonite (Bibring et al. 2006). Fe-rich smectites such as nontronites are usually found in hydrothermally altered mafic rocks on Earth. Such findings indicate that Mars must have had and sustained an active hydrological system in order to alter mafic igneous rock into clays. In addition, clay minerals can also form in the subsurface by hydrothermal activity that can be either impact-generated or magmatic-driven.

Subsequent discoveries were made using the more advanced CRISM spectrometer. Investigations at a higher spectral and spatial resolution revealed that phyllosilicates are relatively common in the southern highlands occurring, apparently without geographical restrictions, in association with hundreds of impact craters (Mustard et al. 2008). Additionally, CRISM data have allowed discovery of the diversity of the hydrated minerals

present through the identification of kaolinite, illite or muscovite, hydrated silica, magnesium carbonate, zeolites, serpentines and prehnite (Mustard et al. 2008, Milliken et al. 2008, Ehlmann et al. 2008a, 2008b, 2009, Murchie et al. 2009). A particular region Mars called Nili Fossae contains clay-carbonate alteration assemblages that have been put forward as an evidence for hydrothermal activity in the region on account of its similarity to terrestrial analogs (Brown et al. 2010). Finally, a more direct evidence for hydrothermal activity (impact-generated in particular) was reported through the discovery of clay minerals associated with the central peak of a Hesperian-aged impact crater (Marzo et al. 2010).

1.6.2.3 In-situ data from Landers: Mars Exploration Rovers (MERs)

In 2004, the Mars Exploration Rover, Spirit, landed on the volcanic plains of Gusev Crater (Squyres et al. 2004, Figure 1.2), and has been in operation ever since. An overview of the mission's results and highlights can be found in the overview papers of the mission's leading scientists (e.g. Squyres et al. 2004, Arvidson et al. 2006, 2008, 2010). Early measurements indicated that the Gusev plains' geology was dominated by relatively unweathered olivine-rich basaltic soils and rocks. The first compelling evidence for significant water-related weathering was the discovery of goethite (Morris et al. 2006), which is a mineral that requires the presence of water for its formation, in addition to hematite and nanophase iron oxides as other alteration products.

Further analysis on a suite of rocks and soil samples using the onboard alpha-particle X-ray, Mössbauer and thermal emission spectrometers revealed a class of rocks with higher abundances of Cl, Br, Zn, and Ge with respect to other basaltic rocks in the area in addition to nanophase iron and volcanic glass. This led Schmidt et al. (2008) to conclude that this type of rock composition and texture (called Barnhill class by the mission scientists) implied interaction with briny groundwater during eruption. These measurements were complemented by similar ones on nearby soils (called Paso Robles soils) reported by Yen et al. (2008) that showed these soils to be dominated by ferric iron sulfates, silica, and Mg-sulfates in addition to Ca-sulfates and phosphates in some samples. Based on the mineralogy, geochemistry, variability and geologic setting, Yen et al. (2008) concluded that the Paso Robles soils likely formed as hydrothermal and fumarolic condensates derived from magma degassing and/or oxidative alteration of crustal iron sulfide deposits. Later observations in the mission added evidence for extensive volcanic activity and aqueous alteration including the discovery of accretionary lapilli, sulfate, silica, and hematite-rich deposits.

The second MER, Opportunity, landed in Meridiani also in 2004 (3 weeks after Spirit at Gusev, Figure 1.2). Most of Opportunity's mission interests have been directed towards nearby impact craters of which the most significant are the 20 meter-wide Eagle Crater (where it originally landed), Endurance (150 m in diameter), and Victoria (1 km in diameter) craters. At the time of writing, the rover is heading to Endeavor Crater; a 22-km-sized crater where sulfates and phyllosilicates have been detected using CRISM (Wray et al. 2009). One of the mission highlights has been the analysis of the first stratigraphic section on a planetary body (Squyres et al. 2006, dubbed the Burns Formation). The rocks of Meridiani are sandstones formed by eolian and aqueous reworking of sand grains that are composed of fine-grained siliciclastics and sulfates. The sulfates in partic-

ular, are dominantly Mg-sulfates and also include Ca-sulfates and jarosite. In addition, the discovery of hematite-rich spherules (known as blueberries) in the eolian bedforms suggests strong interaction with groundwater.

1.6.3 Impact-generated hydrothermal (IGH) systems on Mars

Impact-generated hydrothermal (IGH) systems are expected to develop around the vicinity of an impact event providing that the surface (target material) is volatile-rich. The Martian crust probably contains significant amounts of water (e.g., Clifford 1993), a hypothesis confirmed by the detection of water ice in the near subsurface at high latitudes by the Gamma-Ray Spectrometer onboard 2001 Mars Odyssey (Boynton et al. 2002, Feldman et al. 2002). Additionally, the discharge estimates for the outflow channels (assuming they have been carved by water) range in millions of km³ (Carr 1996) indicating a large subsurface reservoir. On the surface of present-day Mars, water is thermodynamically unstable in most regions due to the low mean temperatures (≈ 180 °K) and atmospheric pressures (≈ 6 mbars). However, the polar ice caps are estimated to contain 1.2-1.7 million km³ and 2-3 million km³ of water ice in the north and south caps respectively (Smith et al. 1999). Finally, the Martian crust is littered with impact craters. Consequently, we can deduce that IGH systems must have been very common on Mars, specially in, but not constrained to, the Noachian period more than 3.5 Ga (Hartmann and Neukum, 2001) which was characterized by high impact activity and probably a hotter planetary interior.

The most significant evidence of IGH activity to date has come from Toro impact crater which is located in the northern margin of the Syrtis Major volcanic province. Toro is a 42-km-diameter and 2-km-deep complex crater, having a central peak and a central pit, both of which mark structural uplift, volatile release, and collapse. In addition, putative hydrothermal mounds are observed on and around the central uplift. Analysis of spectral data in Toro impact crater shows multiple mineralogic signatures that include prehnite, chlorite, Fe-smectites, and opaline material (Marzo et al. 2010). The observed suite of minerals is believed to be hydrothermal in origin, being linked to the impact crater event during the Hesperian Period (Fairén et al. 2010, Marzo et al. 2010).

Several studies, including simple analytic models and 3D numerical porous-flow models, have investigated the behavior of IGH systems on Mars. Early studies focused on potential association with crater lakes. When in communication with a large subsurface aquifer, energy balance calculations show that crater lakes will remain at least partially unfrozen for millions of years due to sublimation removal of ice from the top and release of latent heat of fusion as water turns to ice at the water-ice boundary (McKay et al. 1985 and McKay and Davis 1991). Newsom et al. (1996) demonstrated that the additional heat supplied by a post-impact melt sheet extends lake lifetimes by tens of millions of years. Rathbun and Squyres (2002) were the first to employ numerical models. Their work showed that IGH systems associated with complex craters 180 km in diameter could support a lake up to 1 km deep. Abramov and Kring (2005) modeled IGH systems associated with 30, 100, and 180 km diameter craters exposed to 5 °C surface temperatures and showed that host rock permeability is the main factor affecting fluid circulation, and that these systems provide hospitable conditions for microbial life for 100,000 years. Barnhart et al. (2010) were the first to incorporate freezing into numerical simulations of IGH systems thus constraining the effects of changing permeability and W/R ratio on the system's

longevity. Finally, Schwenzer and Kring (2008, 2009, and 2010) have investigated the resulting mineral assemblages for different IGH conditions, W/R ratios, permeabilities, and parent material composition.

1.7 Summary and thesis structure

As discussed above, a planet such as Mars with its rich hydrologic and volcanic history is expected to display various forms of hydrothermal activity. Indeed, multiple observations by various remote sensing and in-situ missions support this hypothesis. If we are to gain better understanding on how Mars evolved through time, we need to study hydrothermal systems because they give clues on the history of both liquid water and heat production in the planet. The present era of space exploration offers plenty of opportunities for interdisciplinary science with a multitude of instruments that are either on the surface or currently orbiting Mars. In this thesis, the author links information from various remote sensing instruments to search for hydrothermal systems on Mars. In the context of this thesis, a hydrothermal system will usually refer to sites of high potential for hydrothermal activity in the past that are in high probability extinct nowadays (unless stated otherwise). The remote sensing techniques that are discussed in this thesis are geochemical, mineralogic, geomorphologic, geologic, and geophysical in nature. However, they are by no means the full extent of techniques that are/can be applied on Mars but are rather a subset which the author was able to use during his studies. The goal of this study will be showing that looking at data from various instruments at once can lead to a better understanding of the processes that act, not just on Mars, but also on Earth.

Chapter 2 will deal with the geochemical aspect through the use of Gamma-ray spectrometry along with a case study to highlight the advantage and limitations of such a technique in detecting IGH systems. Chapter 3 deals with geomorphological and geological surface manifestations highlighted through an extensive case study that was carried out to search for signs of IGH systems too. Chapter 4 is an extensive case study combining all the techniques that have been discussed to search this time for a magmatic-driven hydrothermal system in the Apollinaris region. Finally, Chapter 5 acts as a follow-up to the work highlighted in chapter 4 by introducing a geophysical technique, ground-penetrating radar, and showing how it can be used to search for certain shallow subsurface manifestations of hydrothermal systems in both magmatic driven and IGH systems.

2 Geochemical Studies through Gamma Ray Spectroscopy

2.1 Introduction

The Gamma Ray Spectrometer (GRS) onboard the 2001 Mars Odyssey is currently the only instrument invoking such a detection technique on Mars. Gamma ray spectroscopy is generally practical for planetary bodies that have little or no atmosphere which can attenuate the gamma ray signal. The Martian atmosphere is thin enough to allow the detection of gamma rays produced in the near-surface rocks and materials. A major advantage of this technique is its sampling depth (≈ 1 meter on Mars, Boynton et al. 2004) as opposed to other techniques such as IR spectroscopy that can only sample the uppermost 100 microns of the surface limiting heterogeneity effects due to surface coatings.

The GRS comprises 3 instruments (Boynton et al. 2004): The Gamma Subsystem (GS), the Neutron Spectrometer (NS), and the High Energy Neutron Detector (HEND). The GS provides elemental abundances at a near-global scale with a footprint of 5° (≈ 300 km at the equator). Important instrument calibration and data reduction steps are discussed fully in Boynton et al. (2007). Currently, the GS has supplied the scientific community with elemental maps of hydrogen, chlorine, iron, silicon, potassium, thorium (Boynton et al. 2007), and more recently sulfur (McLenan et al. 2010), in addition to other elements at a poorer resolution or as a global average such as uranium, aluminum, calcium, sodium, chromium, and manganese (Evans et al. 2008). Due to presence of ice in the near surface which masks the signals from other elements, the GS elemental maps are usually confined to the mid latitudes (45° , and 75° for K and Th). Despite that, it is this near global mapping in addition to the deep sampling of the GRS instrument that has made it an excellent tool in determining significant regional-scale chemical variations in the mid-latitudes of Mars (e.g., Taylor et al. 2006, Keller et al. 2006, Newsom et al. 2007, El Maarry et al. 2009, Karunatillake et al. 2009). More technical aspects of the instrument can be found in Appendix A. We now look at a case study on IGH systems that was published by the author as a Lunar and Planetary Science Conference (LPSC) abstract and poster (El Maarry and Gasnault 2009).

2.2 Case-Study: Impact-generated Hydrothermal Systems

Hydrous minerals such as phyllosilicates and zeolites have been reported before in the mid latitudes on Mars (Poulet et al. 2005, Bibring et al. 2006, Mustard et al. 2008).

In many cases, these hydrous minerals are found associated with impact craters either in the ejecta lobes, crater walls, or central peaks. Large impact events in water rich terrains such as those on Mars are known to generate hydrothermal systems with long enough lifetimes, even under current Martian conditions, to form hydrothermal alteration products such as clay minerals, zeolites and carbonates (Newsom 1980). In addition, neutron and gamma-ray elemental maps show that the surface of Mars is rich in the mid-latitudes with chemically bound Hydrogen (Boynnton et al. 2002, Feldman et al. 2002) since water ice is not expected to be stable at such low latitudes (Mellon and Jakosky 1993). This work aims at correlating the GRS hydrogen maps for the mid-latitudes, i.e. areas with high probability of chemically bound Hydrogen, with another map depicting crater density in bins similar to those of the GRS maps ($5^\circ \times 5^\circ$ bins).

2.2.1 Maps used

A simple method of crater counting was used for constructing a $5^\circ \times 5^\circ$ gridded map. Each bin was given a value that is dependent on the number of craters larger than 20 km in diameter inside the grid, since craters smaller than this size are not expected to form large enough hydrothermal systems that would yield considerable amounts of hydrous minerals. Moreover, the grid score is indicative of the total area of the grid that is covered by craters. This map was limited only to the mid-latitudes to have the same dimensions of the gamma-ray elemental map of hydrogen. Finally, the crater density (Figure 2.1) map was correlated with the most recent hydrogen elemental map from the GRS suite (available online at <http://grs.lpl.arizona.edu/home.jsp>) which is mapped as equivalent water through the assumption that most of the hydrogen is linked to oxygen atoms either as water molecules or OH ions as part of the chemical structures of certain minerals (Figure 2.2).

2.2.2 Results and discussion

The results of the correlation are shown in Figure 2.3. As a first estimate, the map shows good positive correlation for many regions. Figure 2.4 shows a chi-square test map for the region. On Mars, impacts have long been recognized as triggers to water-related events such as hydrothermal alteration of melt sheets and small outflow channels. Furthermore, craters that are large enough (>20 km in diameter) are expected to have sustained long-lived hydrothermal systems, and even crater lakes (Newsom et al. 1996). The resulting products from such systems are commonly hydrous rich and altered minerals such as clay minerals (most notably nontronite and montmorillonite), zeolites, quartz, and even carbonates. In addition, areas with low crater counts (associated with young extensive volcanism) correlate strongly with areas of poor hydrogen, notably, the Tharsis rise, Elysium, and Tyrrhena.

A similar work has been carried out before to correlate the GRS data with age units on Mars (Hahn et al. 2007), where the authors report that H-rich areas in the mid-latitudes lie mainly within Noachian terrain. Our analysis can provide a geological and geochemical reasoning to this correlation. The most notable geomorphic feature that is currently visible in the Noachian terrains is impact craters and basins. The good correlation between areas of high crater density and H-rich regions and the corresponding trends in Amazonian and

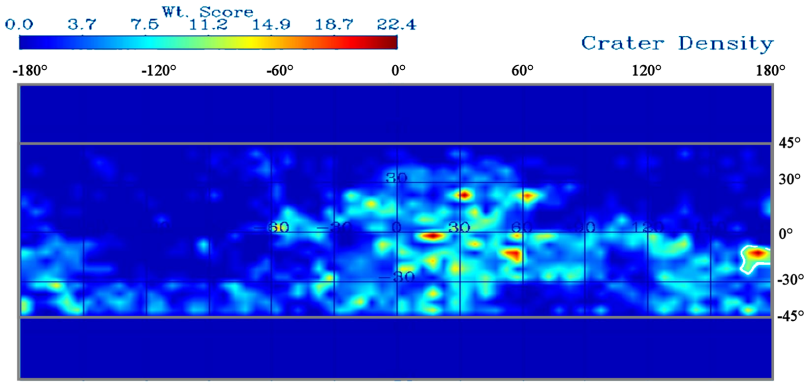


Figure 2.1: Map of crater density in the mid latitudes. The weighting score is directly proportional to the surface area covered by impact craters larger than 20 km in diameter in a given grid. The map is smoothed for clarity.

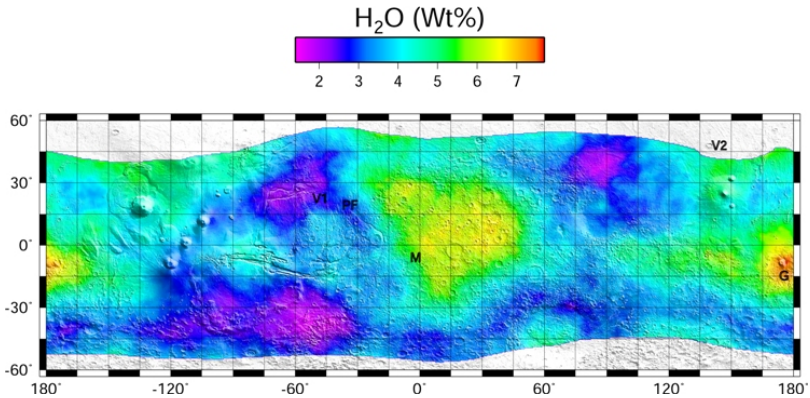


Figure 2.2: 5°x5° map of water-equivalent hydrogen in the near subsurface as measured by the GRS. The map covers only the mid latitudes due to the masking effects of near sub-surface ice in the higher latitudes.

H-poor regions imply that hydrothermal systems formed by impact crater events could be a major contributor in forming the hydrous minerals that are apparent on the surface of Mars today.

Nonetheless, despite the good overall correlation, the use of GRS as a tool for detecting hydrothermal systems can be problematic. The main strength of the GRS lies in its ability to penetrate deeper into the surface than conventional spectrometers that are limited

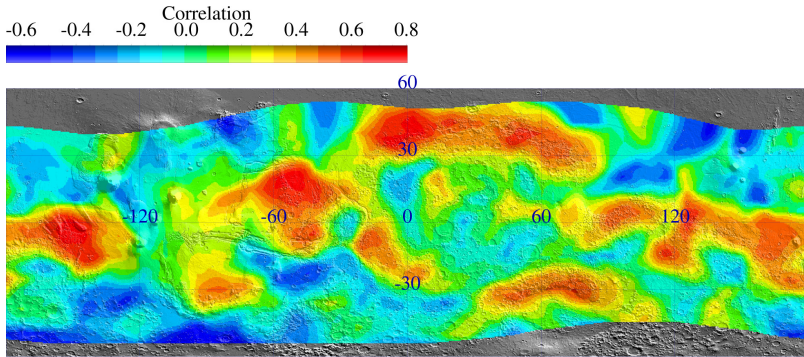


Figure 2.3: Correlation map of GRS equivalent water in the mid latitudes with crater density superimposed on a Mars MOLA map. Red/Orange regions signify high positive correlation between number of craters and concentration of chemically-bound water.

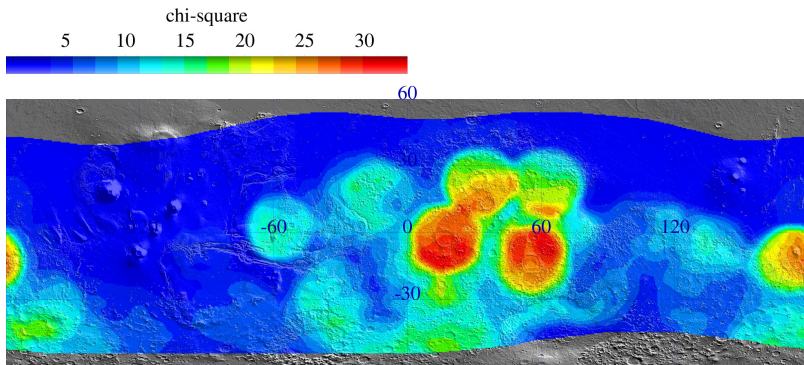


Figure 2.4: Map of Chi-square test on the datasets. Lower values (regions in blue) signify a high degree of confidence.

to the first few microns of the surface, and its regional context. However, it is this regional context that limits our ability to pinpoint accurate sources for the GRS reading. The GRS footprint is ≈ 300 km at the equator. In addition, the data reduction step leads to cross-correlation effects between each pixel and its neighbors. Consequently, while the GRS may be inefficient in detecting small-scale activities, it can be used more effectively with huge impact basins, in addition to the detection of possible indicators of magmatic-driven systems. For instance, The GRS detects high chlorine and hydrogen over the Medusa Fossae Formation that covers large areas in the Northern Plains of Mars. Such deposits could be ignimbrite deposits related to hydrothermal/magmatic systems that led to explo-

sive eruptions and the generation of large-scale pyroclastic flows as is seen at Apollinaris Patera which is an important target area that will be discussed later in the thesis.

3 Geology & Geomorphology through High Resolution Images-Case Study: Crater Floor Polygons

3.1 Preface

Since In-situ exploration remains in principle not possible yet for Mars except for very limited exceptions such as the Landers and Rover missions, one has to rely heavily on remote sensing from orbiting data (or Earth-based observations) to search for not only evidence of hydrothermal activity, but also for numerous clues on the geological and geochemical evolution of Mars. One of the most important obstacles that a human remote observer has to deal with is the principle of equifinality: Various geological processes can take different evolutionary paths and yet end up with morphologically similar structural manifestations. For that, it is important for the observer to derive means to strengthen or eliminate some of the proposed formation mechanisms in order to constrain the possibilities and have a more accurate hypothesis. A similar problem arises during the search for hydrothermal systems when trying to identify key geological features that would indicate such an activity existed (or is still ongoing).

Desiccation cracks can act as an important indicator of the past presence of a water body or lake. Indeed, as previously discussed, IGH systems are expected to generate lakes in the crater basins which could be sustained for an amount of time depending on the size and duration of the driving hydrothermal system. A major problem in identifying these features on Mars is the morphological similarity of desiccation cracks to thermal contraction permafrost polygons that are ubiquitous on the Martian surface due to the high thermal fluctuations and extremely low temperatures. In this chapter, a case-study that was published by the author (El Maarry et al. 2010) is presented in which a physical model is put forward to differentiate between thermal contraction polygons and desiccation ones, and in doing so, identify potential hydrothermally-generated paleolakes on the surface of Mars.

3.2 Introduction

Polygons are one of the most common features in the high latitudes of Mars. They have been observed by both landing and orbiting spacecraft. The mode of formation of these polygons has been disputed among various workers in the field, and generally has de-

pended, on their size scale. Polygons on Mars may range in size from 2 to 3 meters all the way up to 10 kilometers in diameter. Consequently, different formation mechanisms have been proposed depending on the size of the polygons of interest, and simple morphological investigation which include thermal contraction, desiccation, volcanic and tectonic processes. (e.g., Mutch et al. 1976, 1977, Lucchita 1983, Pechmann 1988, Seibert and Kargel 2001, Mangold 2005).

Thermal contraction polygons form when an ice-cemented soil undergoes seasonal contraction resulting in high tensile stresses, which when large enough, can overcome the tensile strength of the soil, thus creating a network of fractures to relieve the stress. Repeated opening and closing of these fractures every season may lead to filling of these cracks with materials such as dust and loose sand to form sand-wedges (Mellon et al. 2008). In the case where liquid water occurs in shallow surface thaw zones, ice wedges can form by percolation into the open cracks. In either case, repeated seasonal cycles further widen the wedges and develop a distinct surface signature (Lachenbruch 1962).

The first physical investigation of the feasibility of thermal contraction in forming small-scale polygons (5 to 10 meters) on Mars was carried out by Mellon (1997) who showed, given the current thermal regime on Mars, that thermal stress builds up in the near surface at high latitudes (down to almost 2 meters beneath the surface at $\pm 60^\circ$ latitude) to high enough values to cause fractures to occur assuming an ice-cemented ground's tensile strength of 2 to 3 MPa. More recent works by Mangold (2005) and Levy et al. (2009) concentrated primarily on the morphological classification and distribution of these small-scale polygons (<25m in diameter).

Desiccation cracks form when a volatile-rich material dries up creating stresses through changing surface tension between soil grains. These stresses form a network pattern of cracks similar to thermal fractures. Desiccation crack patterns can be morphologically similar to fractures formed by thermal contraction processes, and thus the two mechanisms are difficult to differentiate based on morphology alone. Indeed, the physical processes can be described by almost the same mathematical equations by replacing thermal diffusivity with hydraulic diffusivity, and temperature profiles with volatile-concentration profiles (Müller 1998). Desiccation crack polygons however, while usually millimeter-sized, can grow up to 300 meters in width, as shown in some terrestrial examples, depending largely on the hydraulic regime (Neal et al. 1968).

Volcanic processes can also form polygonal crack patterns through a single event of thermal contraction such as is often observed in basaltic columns. Tectonic processes on the other hand, can vary and may explain km-sized polygons located in the northern plains of Mars (Pechmann 1980, McGill and Hills 1992). Faulting and rebound of sediment fill in a basin after the removal of a water/ice load, for example, may have contributed to the formation of giant polygons in Utopia (3 to 10 km-sized).

This work focuses on a peculiar group of intermediate-sized polygons that range in size from 15 to 350 meters in diameter, which are associated almost exclusively with the floor materials and occasionally, the ejecta deposits of impact craters (thereby giving them the name Crater Floor Polygons), and are usually found to exhibit more fracturing with time. We discuss the morphology of these polygons, and their similarity to desiccation patterns and permafrost polygons on Earth and Mars. In addition, we investigate possible formation mechanisms for these polygons. For this work, we are neglecting smaller sized polygons that are 5 to 10 meters in diameter on account of their usual association to certain

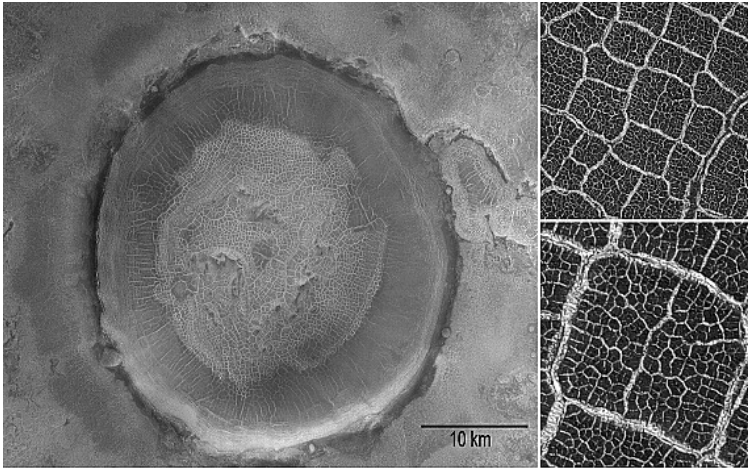


Figure 3.1: Typical crater floor polygons. (left) CTX image of a 14 km-sized crater. (upper right) High-resolution HiRISE subimage of same crater. Two distinct size groups can be inferred: A large 70 to 350 m-sized polygons with an average polygon diameter of 120 m, and a smaller group, not always present, ranging in size from 5 to 20 m. (lower right) HiRISE subimage of a single 100 m-wide polygon (Image IDs: CTX: P16_007372_2474, HiRISE: PSP_007372_2475).

rock units rather than the crater floor and their abundance at other areas not associated with impact craters.

3.3 Morphology and geographic distribution

Crater Floor Polygons (here and after referred to as CFPs) have been discussed, albeit briefly, by previous workers (e.g., Seibert and Kargel 2001, Kuzmin and Zabalueva 2003, Mangold 2005). These previous efforts have been limited to morphological investigations and classification, and did not benefit from the currently available high-resolution imagery. For this work, the complete set of MOC (Malin and Edgett 2001) narrow angle high-resolution images (1.5 to 12 meters/pixel) targeting impact craters were used. In addition, we used the images from the Context (CTX) camera (Malin et al. 2007) which has a 6 m/pixel resolution, and the High Resolution Imaging Science Experiment (HiRISE) camera (McEwen et al. 2007) with its impressive 25-32 cm/pixel resolution that were available at the time of our mapping effort (until November, 2009).

As can be seen through the different imaging systems (Figure 3.1), CFPs are characterized by a network of regularly spaced troughs surrounding an interior region of relatively level ground. Often seasonal CO₂ frost accentuates the patterns. The troughs extend around the perimeter of each polygon. Their dimensions are variable but tend to display widths that range from \approx 1 meter up to 10 meters. The polygonal pattern is created by the

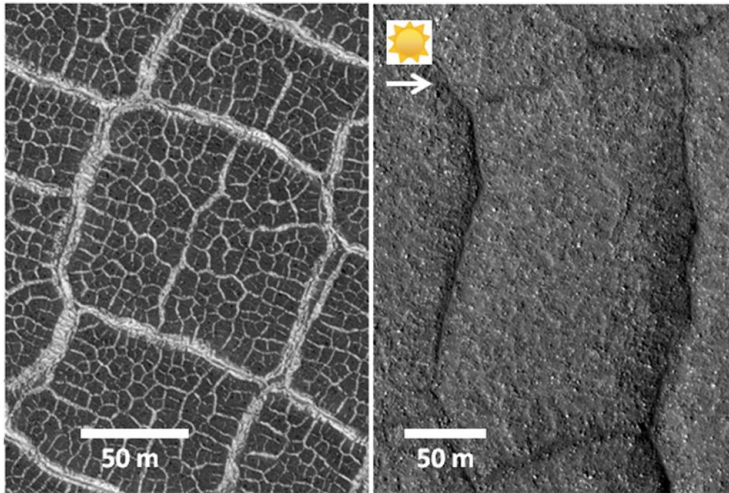


Figure 3.2: HiRISE subimages of crater floor polygons. (left) 100 m-wide polygon with a 6 to 8 m-wide, frost-filled troughs surrounding it. Secondary troughs within the primary polygons form polygons with an average diameter of 10 m. Image ID: PSP_007372_2475 (67.2°N, 47.8°E). (right) 125 m-wide polygon with frost-free troughs. Note the lack of secondary troughs. Image ID: PSP_001942_2310 (50.7°N, 341.6°E).

intersection of these troughs in a commonly orthogonal manner; though some irregular and semi-hexagonal patterns also occur. Such pattern is common among fractures formed through thermal contraction or desiccation processes (Lachenbruch 1962). The features may cover the entire crater floor, but occasionally they occupy isolated patches or regions, especially in large (>50 km in diameters) craters.

There are different ways to measure the size of a polygon. For example, Levy et al., (2009) employed a technique of averaging the distance between the center of a polygon and its closest 6 neighbors. Mellon et al. (2008) used both the average of long and short axes and the average of X and Y image axes, finding statistically the same result and that axis orientation did not matter. In this work, the variance in polygon size was observed to be low, and thus the polygons could be adequately approximated to be squares. As a result, polygons were counted inside a region of interest with a known surface area followed by taking the square root of the average polygon area, yielding a satisfactory average for the CFPs inside a given crater. It can be seen from the high resolution images (Figure 3.2) that the polygons may form two distinct size groups: the main or primary troughs form polygons that range in size from 15 to 350 meters in diameter, with an average global size of 120 meters (Figure 3.3). This group represents the prime focus of the current work. Secondary troughs, when present, are narrower and embedded within the larger polygons and thus subdividing them. These troughs tend to intersect in a more random manner. The smaller polygons range in size from 4 to 20 meters, and as such resemble

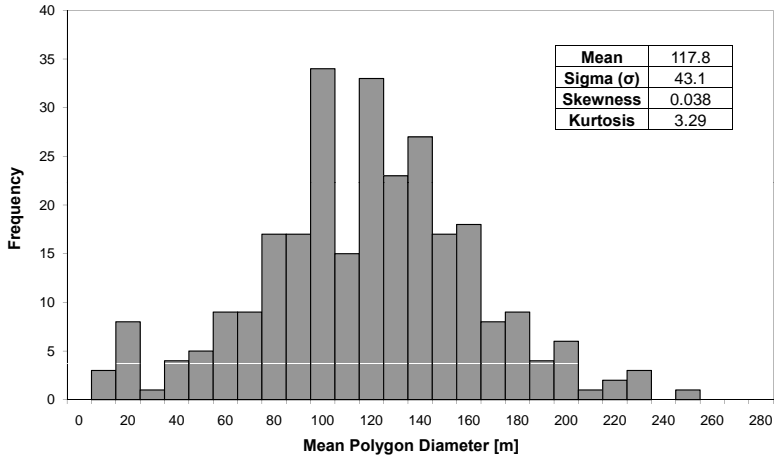
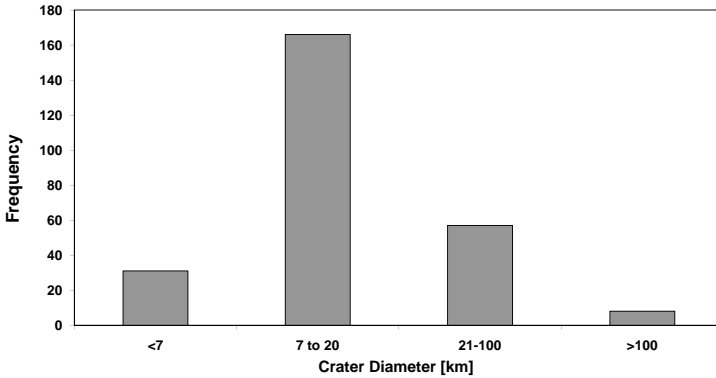


Figure 3.3: A histogram of the average polygon diameter of the main (primary population). Each point represents an average of polygon size in a certain crater (or locality in the case of Hellas and Argyre basins). Most polygons are 100–120 m in diameter. Inbox: A list of important statistical parameters for the database. Sigma stands for the population standard deviation.

more closely thermal contraction (ice or sand wedge) polygons that are widespread in the Martian high latitude and circumpolar regions. However, they may also represent progressive subdivision common in terrestrial mud cracks.

CFPs are found almost exclusively in impact crater floor material and less frequently along crater walls or associated with ejecta deposit materials. With few exceptions, they lack raised rims. Some however, show uplifted centers (Figure 3.2), which are features common to ice-wedge or sand-wedge polygons due to incremental seasonal wedge growth. On the other hand, numerous craters at low (warmer) latitudes show simple, almost unfilled troughs, which is more indicative of "one-time" desiccation processes. Finally, the above mentioned characteristics of CFPs are used to distinguish them from common rock fractures that usually show more random forms of cracking which includes shapes and sizes, as opposed to both the orthogonal geometry and the local uniformity of polygon sizes of CFPs.

Craters containing CFPs are variable in size (Figure 3.4) with no visible correlation between the polygons and crater diameters. In other words, a large crater does not appear to have larger polygons than a smaller one. Figure 4b shows the ratio of craters containing CFPs to the global population of the same size class (Barlow Crater Database: Version 1). It can be seen that with the interesting exception of large impact basins (>100 km), the CFP-craters seem to show similar frequency distributions to the global population (thus limiting imaging coverage biases). However, CFPs appear to be more common among

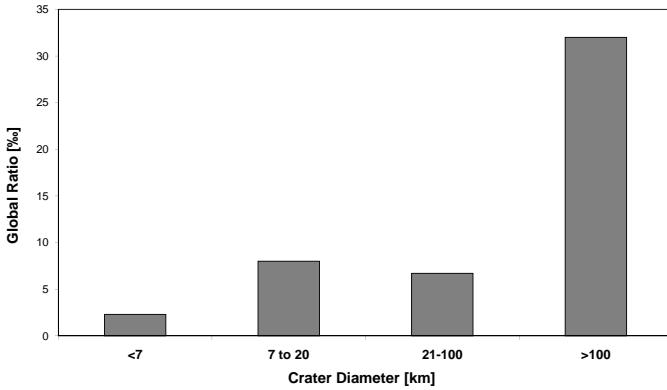


[a]

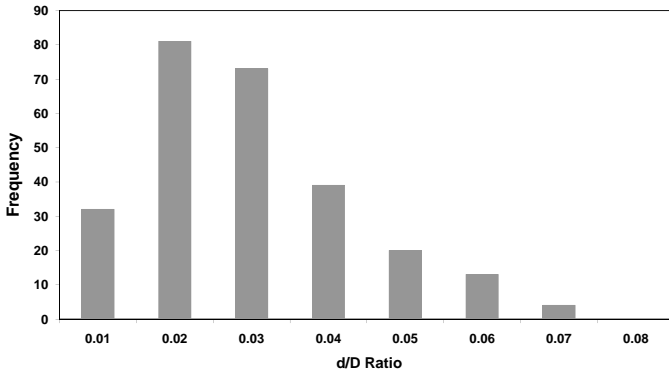
Figure 3.4: (a) Histogram of diameters of craters containing CFPs. Most features are located in complex craters ranging in size from 7 to 100 km in diameter (83%). A smaller, albeit significant population is located in small (<7 km) simple craters (15%). (b) Plot of CFP-filled craters as a ratio of the global crater population (over 42,000 craters) with the same diameter. It can be seen that CFPs are indeed more common in complex craters than in simple ones. (c) A histogram of depth-diameter (d/D) ratios for impact craters in this study. Of total craters, 59% have a d/D ratio between 0.02 and 0.03, and more than 93% are less than 0.06. The average d/D for fresh craters on Mars is 0.09 for simple craters and 0.11 for complex ones.

craters that are larger than 7 km in diameter. Such craters are termed complex since gravity causes the initially steep crater walls to collapse downward and inward, forming a complex structure with a central peak or peak ring (Melosh 1989). This preference could be attributed to the fact that complex craters have a larger probability of creating a post-impact lake due to the higher energies involved (Abramov and Kring 2005). There is a preference to small and middle-sized complex craters (7-20 km in diameter). This could indicate an age bias, since most craters in this range are expected to be younger than larger craters, thus maintaining a higher probability for the features' preservation. The large discrepancy with respect to the large basins can be attributed to an imaging bias, since most of the large basins are extensively imaged due to higher scientific interest.

Depth to diameter ratios (d/D) of variable-sized impact craters containing CFPs (Figure 3.3) are usually lower than the nominal ratio for "fresh" craters on Mars (Barlow 1993, 1995). d/D ratios for fresh craters on Mars can differ markedly depending on location due to the heterogeneity in surface properties thus rendering the use of a single d/D relationship for fresh impact craters on Mars impractical (Barlow 1995). As a result, d/D ratios can vary from 0.06 to 0.35 for simple craters (with a considerable error margin), and 0.04 to 0.23 for complex craters (Barlow 1993). However, the rather low values are confined to certain localities on Mars such as Maja Valles and Acidalia, regions where there has been significant emplacement of rock materials (Tanaka et al. 2005) and as a re-



[b]



[c]

sult an average of 0.09 for simple craters and 0.11 for complex craters is considered to be globally acceptable for this analysis. Such values are markedly higher than d/D ratios for the craters in this study since almost 60% of them fall in the range between 0.02 and 0.03, while 93% of the craters have d/D ratios less than 0.06. This indicates that the polygonal patterns are usually occurring in infill deposits that have accumulated inside the craters after their formation.

3.3.1 Geographical distribution

Figure 3.5 shows the locations of 262 impact craters that have been observed in this study to contain CFPs (For the full list, see Appendix B). The northern lowlands show an apparent preference to high latitudes. In the case of the southern highlands, while

high latitudinal preference is similarly visible to a certain degree, locations seem to be more scattered. Interesting to note is that the features extend down to the equator in both hemispheres. In addition, clustering of the features is evident in many localities. Notable examples are Nili Fossae and Utopia in the north, and Hellas basin in the south.

Utopia Planitia is centered at 49.7 °N 118 °E in the northern lowlands. The landscape comprises an assemblage of landforms that is consistent with aqueous processes that could be related to the formation of large bodies of water and of periglacial activity (e.g., Parker et al. 1993, Scott et al. 1995, Fairén et al. 2003, Soare et al. 2005, de Pablo and Komatsu 2009). The Nili Fossae region, centered at ≈ 22 °N, 75 °E and located northwest of the Isidis Basin, records a significant hydrologic/lacustrine history (e.g., Fassett and Head 2005), including mineralogical signatures of olivine (Hoefen et al. 2003), hydrous minerals (e.g., Mangold et al. 2007, Mustard et al. 2008, Ehlmann et al. 2008a, 2009), and more recently, carbonates (Ehlmann et al. 2008b). Centered at 42.7 °S, 70 °E, Hellas Basin is one of the largest impact craters in the Solar System with a diameter and an average depth of 2300 km and 7 km, respectively. Its rich array of deposits and various geomorphological features point to numerous episodes of hydrologic activity, including the formation of possible lakes and glaciers (e.g., Moore et al. 2001, Bandfield 2008), as well as aeolian deposition (Tanaka and Leonard 1995).

Finally, some well-known impact craters containing CFPs that have been discussed before in literature due to their significant history of liquid water processes and/or interesting mineralogy include Gusev (Grin and Cabrol 1997), Gale (Cabrol et al. 1999), Holden (Pondrelli et al. 2005) Bakhuisen (Malin and Carr 1999), Antoniadi (Bandfield 2006), Miyamoto (Wiseman et al. 2008), Jezero (Ehlmann et al. 2009), Endeavour (Wray et al. 2009), and Morella (Komatsu et al. 2009).

3.3.2 Association with periglacial features

Notably, most polygons in the high latitudes are filled with a high-albedo material (either permanent ice or seasonal frost) that highlights the features aiding in their detection. This feature enhancement could be responsible for creating an "apparent" latitudinal bias when compared to warmer locations. The CFPs have been described as periglacial features formed by thermal contraction processes acting on a water ice-rich substrate (Kuzmin and Zabalueva 2003, Mangold 2005), in part influenced by this latitudinal bias coupled with a limited number of identified CFPs during previous investigations, although other studies have pointed out the difficulty of ruling out desiccation processes (Seibert and Kargel 2001). While the basic assumption behind identifying these features as periglacial has been on the grounds that they were not observed below 60° in both hemispheres, our mapping shows that more than 37% of the observed features are located below this latitude extending to the equator (Figure 3.6). A significant reason for these features escaping detection has to do with the resolution limit of previous imaging instruments. Indeed, most of the observations in the lower latitudes are possible due to the very high resolution of the HiRISE camera, which can resolve sub-meter features. This permitted the detection of 1 meter-wide-troughs, thus expanding the dataset considerably. Nonetheless, we cannot rule out possible contributions from periglacial conditions in enhancing CFP distribution in the high latitudes.

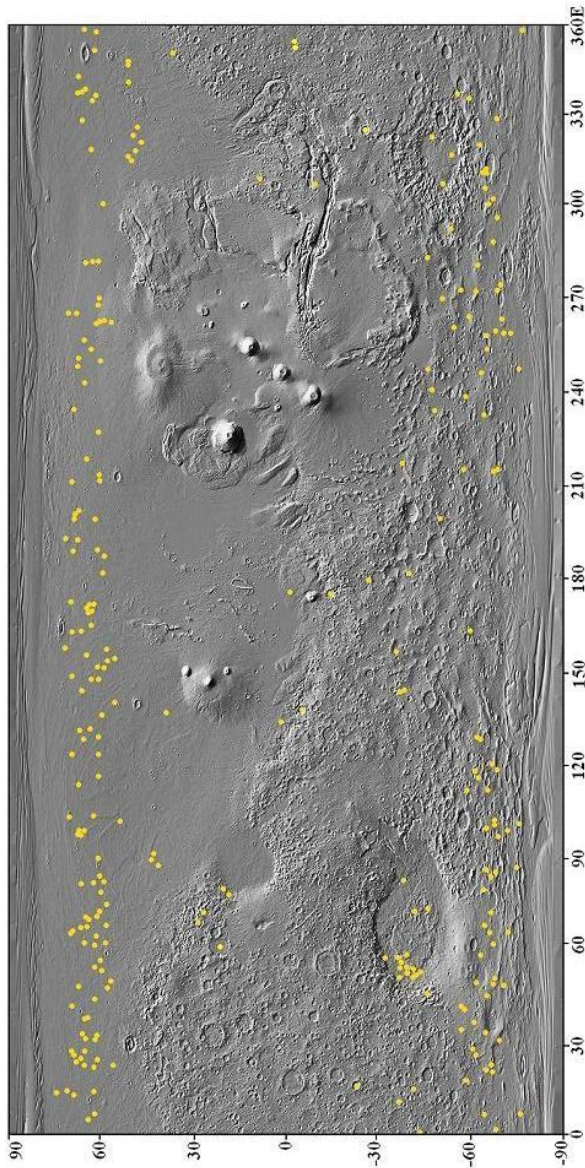


Figure 3.5: Distribution of craters with CFPs shown on a Mars Orbiter Laser Altimeter topography map of Mars. Features appear to be concentrated at high latitudes. However, a considerable number extends equatorward. Note the regional clustering at Utopia, Nili Fossae in the Northern Hemisphere, and Hellas in the south.

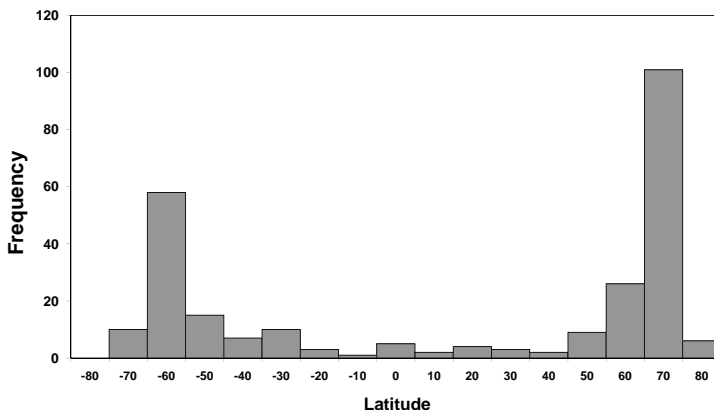


Figure 3.6: Histogram of CFP distribution. A dominant occurrence of CFPs is observed at higher latitudes. However, the features extend down to the equator and more than 35% can be found below Lat 60° in both hemispheres.

3.3.3 Terrestrial analogs

On Earth, thermal contraction polygons in the form of ice and sand wedges, are located in both Arctic and Antarctic environments. They are generally 20 meters wide (Yoshikawa 2000), but can grow up to 45 meters such as the giant polygons in Iceland (Friedman et al. 1971). While individual cracks may only be millimeters wide in a given season, many years of cracking can cause wedges to grow to meter-scale.

Though desiccation cracks are commonly sub-meter in scale, a comprehensive work on giant desiccation polygons (Neal et al. 1968) lists numerous localities in the Great Basin playas in the United States that have desiccation-crack polygonal patterns attaining a width of up to 300 meters. Interesting examples are Coyote Lake in California (Figure 3.7; 35° 05'N, 116° 45'W), Black Rock Desert in Nevada (Willden and Mabey 1961) (40° 45'N, 119° 12'W), Guano Lake in Oregon (42° 07'N, 119° 31'W), and the Indian Springs Playa (36° 42'N, 115° 38'W). These locations show desiccation cracks ranging in size from 30 to 75 meters with some of the polygons reaching 300 meters in diameter, approximating the CFP dimensions. In addition, the cracking patterns show similar orthogonal intersections, as well as polygons that occasionally grade into striped patterns observed in some CFP cases (Figure 3.8). On Earth, such features usually occur in clay playas, but can also occur in other geological materials such as sandstone. The formation of these polygons is attributed to desiccation of the once water-rich materials related to the lowering of the ground water table. If the material initially contained a significant water volume, the loss of this water would result in major shrinkage and related tensile stresses, leading to rupturing and formation of fissures to relieve the stress. In colder regions, desiccation and thermal contraction processes can work together. Prime examples include



Figure 3.7: Desiccation cracks in Coyote Lake in California, US (35.1°N, 116.7°W). Crack spacing ranges from 30 to 75 m. These cracks have formed through the lowering of the water table. (Image credit: Google Earth).

dry karst lake basins in Tuktoyaktuk, Canada (Mackay 1966, Soare et al. 2008). As a thermokarst lake loses its water through evaporation or drainage, wet lake sediments are exposed to freezing temperatures (Mackay 1966). A freezing front forms and migrates in a downward direction, eventually forming thermal contraction polygons. These polygons, however, are considerably smaller (≈ 40 m in diameter) than the CFPs.

Many volcanic rocks, especially basaltic flows, are divided by fractures into slender prismatic columns. In plain view, these column-bounding fractures form remarkable polygonal patterns that vary from being orthogonal to nearly hexagonal (Aydin and De-graff 1988). The columns are usually tens of meters long with diameters that range from ≈ 0.2 to 2 meters at most (Grossenbacher and McDuffue 1995). Such a small diameter range makes it unlikely that such a process could be responsible for the formation of CFPs. In addition, as described above, most of the craters with CFPs show d/D ratios that indicate deposits that partly infill the impact crater. However, the general morphology of these deposits is not indicative of lava flows. As a result, taking into account the morphology, physical dimensions, and geologic context of the CFPs, we are left with thermal contrac-

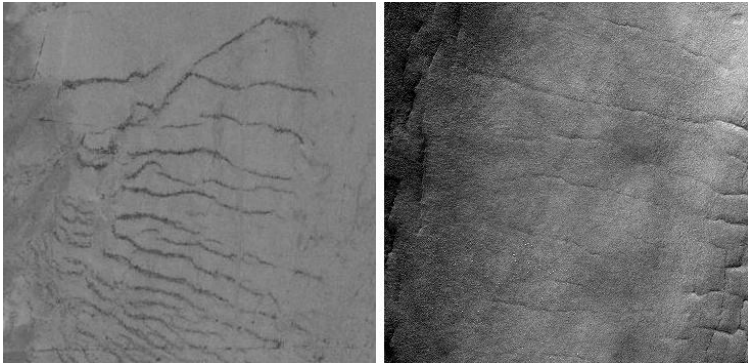


Figure 3.8: (left) Desiccation stripes in the Indian Springs Playa, Nevada ($36^{\circ}42'N$, $115^{\circ}38'W$). Fractures are 400 m in length on average (Image: Google Earth). (right) Morphologically similar patterns associated with CFPs in some Martian craters. Sun is in the top right of the image. Stripe-like patterns are 600 m in length (Image ID: PSP_001942_2310, centered at $50.7^{\circ}N$, $341.6^{\circ}E$).

tion in permafrost and desiccation processes as viable mechanisms for the formation of CFPs. In the following section we discuss these two processes in more detail.

3.4 Mode of formation: thermal contraction in permafrost vs. desiccation

Differentiating between different polygon formation mechanisms using remote sensing and limited in-situ data has been, and remains to be, a difficult task. Ever since polygons were observed at the Viking 2 Lander site, it has remained elusive to pinpoint a specific formation mechanism. This has been largely due to the sole reliance on remote morphological investigations. An example of an early investigation is Mutch et al. (1977), who favored thermal contraction as a mechanism for forming the polygons at the Viking lander site. However, they could not rule out desiccation processes. This was not the case with km-sized polygons located in the Utopia basin (Mutch et al. 1976). Several authors (e.g., Pechmann 1988, McGill and Hills 1992) have shown that thermal contraction among other periglacial processes and desiccation could not be responsible for the formation of these giant polygons since that would involve a relatively deep stressed zone (almost 500 meters deep), which cannot be due to thermal or desiccation tensile stresses. As such, they concluded that regional tectonic processes were most likely responsible for the formation of the polygons. The debate has remained, however, for smaller (10 to 200 meter-sized) polygons. Baker (2001), for example, favored ice-wedging as a process for forming the 40 to 100 meter-sized polygons that were seen in Mars Orbiter Camera (MOC) images. Seibert and Kargel (2001) favored the same mechanism, but did not rule

out mud desiccation.

The first physical investigation of thermal stresses on Mars and their role in forming polygonal troughs in permafrost was done by Mellon (1997). Using a standard thermal model for Mars (Mellon and Jakosky 1993), he was able to show that diurnal thermal fluctuations on Mars were capable of generating enough thermal tensile stress in the higher latitudes (from 45° and upwards) to overcome an assumed tensile strength (2 to 3 MPa) of a frozen soil (linear mixture of basalt and ice with a porosity of 45%) creating polygonally fractured terrains. Mellon et al. (2008) modeled thermal contraction polygon size using a more sophisticated finite element model than was used in Mellon (1997). Though their work focused on 68°N latitude (in preparation for the Phoenix mission), a key support of this work is that they showed that small polygons (roughly 5-20 meters) are the norm on Mars, larger ones (>20 meters) require very specific conditions, and very large polygons ($\gg 20\text{m}$) are difficult to form at best. A first step in our physical modeling is to use the results from the previous studies to deduce the maximum physically achievable fracture depth, and consequently, the fracture spacing to answer an important question: with the current knowledge of Martian meteorology and soil properties, can thermal stresses alone be responsible for the formation of 20-250 meter-sized polygons with current climatic conditions on Mars?

3.5 The physical model

3.5.1 Depth and spacing of tension cracks

Tension or contraction cracks develop in different materials of geological interest, such as basalts, mud, and permafrost. They occur in response to the buildup of stress in a material by different mechanisms such as tectonic extensional forces, cooling, or loss of volatiles (desiccation). If the material is not allowed to contract (or strain), stresses may build up until they exceed the tensile strength of the given material, in which case, fractures develop to relieve the stress. The amount of relieved stress will depend on many factors related to the material's physical properties, but to a first order, it is directly dependant on the depth of the crack. The depth of the crack in return, is mainly dependant on the thickness of the stressed zone (hereafter, "stress" implies tensile stresses unless stated otherwise). The tensional crack is not expected to propagate much deeper beyond the stressed zone. Nonetheless, Maloof et al. (2002) showed that fractures may propagate 3-15 times the depth of the thermally stressed layer if the ground is cold and brittle. However, they modeled diurnal thermal variations which form a 10-20 cm-thick stressed layer under terrestrial conditions at ≈ 600 Ma during a Neoproterozoic glacial episode (Maloof et al. 2002). For such thin stressed layers, both gravitational loading and geothermal gradients are not significant. On the other hand, variations on a seasonal scale create a thicker meter-scale stressed zone, and fractures in that case do not extend far beyond the stressed layer due to compressive stresses and viscous relaxation associated with transition to warmer temperatures.

For a given initial stress distribution, the width of the zone of stress relief (i.e. crack spacing) increases with the depth of the fracture (Lachenbruch 1961, 1962) as deeper fractures allow more strain to occur at the surface which elastically relieves more stress.

The extent of this dependence varies according to the mechanism under investigation. Lava cooling columns usually have fracture depths several times the fracture spacing. But this is a special case, because the fracture spacing is set in the top layer that has hardened, while the deeper and hotter parts of the flow are still fluid (Müller 1998, Toramaru and Matsumoto 2004). In the case of thermal contraction polygons and desiccation cracks in mud and various soils, the ratio of fracture depth to spacing varies from 1:3 up to an upper limit of 1:10 (Lachenbruch 1962, Corte and Higashi 1964, Neal et al. 1968, Parker 1999). From the above we can infer that the size of the fractured network of polygons is directly indicative of the thickness of the stressed zone. Thin stressed zones can only lead to relatively shallow fractures which in turn have a small stress-relief effect making the fracture spacing small. On the other hand, thick stressed zones lead to the formation of deeper, more stress-relief-efficient fractures, thereby increasing the crack spacing and the overall size of the polygonal network.

In order to estimate the maximum depth a fracture can penetrate, two approaches are possible: the energy criterion and the stress intensity approach (Anderson 2005). These two approaches are usually equivalent, and so both will be used simultaneously. The energy-criterion approach states that crack extension occurs when the energy for crack growth is sufficient to overcome the resistance of the material. Assuming linear elastic material and following Anderson (2005), the energy released during crack formation per unit area, G , is given by:

$$G = \frac{\pi\sigma^2 d}{E} \quad (3.1)$$

where d is fracture depth in meters, E is the Young's modulus in pascals, σ is the remotely applied stress in pascals, and G is in J/m^2 . For every material there is a characteristic G_c , such that as long as the energy release rate of the growing fracture is larger than this critical value G_c , the fracture continues to grow. The maximum depth of the crack will be the point at which $G = G_c$ which is given by,

$$G_c = \frac{\pi\sigma_f^2 d}{E} \quad (3.2)$$

where σ_f refers to the failure stress or as it is referred to commonly in literature, the ultimate tensile strength (UTS) of the material. Equation (3.1) and (3.2) state simply, that as long as the tensile stresses around the crack are surpassing the tensile strength of the material, the fracture will continue to grow. The stress-intensity approach involves the use of a single constant called Stress-Intensity Factor K , which when known, can be used to compute the whole stress-strain distribution around a fracture tip (Anderson 2005). K was expressed adequately for vertical fractures in a given material by Lachenbruch (1962) who considered both thermal stresses and hydrostatic ones caused by the weight of ground to compute K_I . Where the "I" subscript refers to Mode I cracking which is a shear-free tensional crack. The expression for K is written as:

$$K_I = \sum_i \sigma_i d^{1/2} \gamma \left(\frac{a_i}{d} \right) - 0.68 \rho g d^{3/2} \quad (3.3)$$

where the first term in the right hand side of the equation is the thermal contribution to the stress-intensity factor ($K_{thermal}$). γ is the "normalized crack-edge stress intensity factor",

Table 3.1: Normalized crack-edge stress-intensity factor γ . Adapted from Lachenbruch (1962).

a/d	$\gamma(a/d)$
0.05	0.04
0.1	0.08
0.2	0.16
0.3	0.24
0.5	0.41
0.75	0.64
1	1.1

which is a dimensionless quantity that has a value dependent on the fraction of the stressed zone in question to the total fracture depth [$\frac{a}{d}$] (Lachenbruch 1962). The values of γ are given in Table 3.1 for different fractions ($\frac{a}{d}$). So as an example, for a fracture depth of 1 meter, the ($\frac{a}{d}$) fraction of 0.05 would correspond to $a = 5$ cm. Consequently, the i^{th} component of K_{thermal} would be computed by multiplying d (1 meter) by 0.04, then multiplying the square root of that product by the value of σ at a depth of 5 cm. The summation over the whole crack length gives the final K_{thermal} value.

The second term depicts the hydrostatic contribution (K_{hydros}) where ρ is the soil density, and g is the gravitational acceleration constant. Similar to our definition of G_c , if we assume that the material fails locally at some critical combination of stress and strain, then it follows that fracturing must occur at a critical stress intensity K_{Ic} . K_{Ic} is what is termed in fracture mechanics as "fracture toughness", which is a size-independent material property with the SI units of $\text{Pa m}^{1/2}$. Finally, K_I can be related to G in the following manner,

$$G = \frac{K_I^2}{E'} \quad (3.4)$$

where,

$$E' = E \quad (3.5)$$

for the case of plane stress, and

$$E' = \frac{E}{1 - \nu^2} \quad (3.6)$$

for the case of plane strain.

In equation (3.6), ν is Poisson's ratio. For our case, the plane strain case is adopted, since all the principle stresses are taken into account and the normal strain, which is small compared to the horizontal stresses, is neglected. So in theory, if the stress distribution in the ground and the fracture depth can be estimated, it should be possible to compute the stress intensity factor and strain energy release during the formation of the crack.

3.5.2 Method of analysis

In order to estimate the thermal stress distribution in the ground, we adopted the stress profiles computed by Mellon (1997) using a time-dependent viscoelastic model (Figure

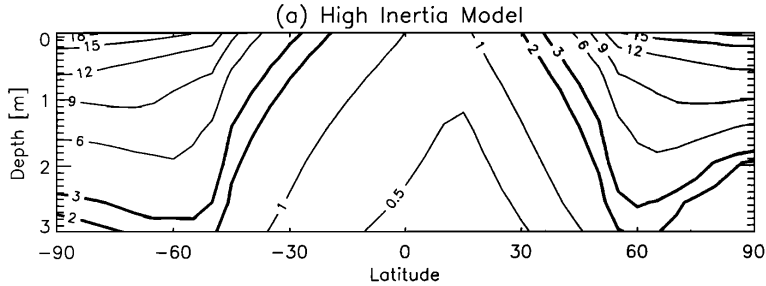


Figure 3.9: Peak tensile stress (in MPa) as a function of depth and latitude. High thermal inertia and low albedo values are assumed in subsurface temperature calculations (Adapted from Mellon 1997).

Table 3.2: Basic Parameters used in the model

Parameter	Value
Mean Soil Temperature	180 °K
Young's Modulus E	1.172×10^{10} Pa
Poisson's Ratio ν	0.4
Soil Density ρ	1800 Kg/m ³
g_{Mars}	3.82 m/s ²

3.9). Interested readers are referred to that paper for a thorough description of the model. Mellon (1997) computed depth and latitude dependent stresses using three different models of thermal inertia and albedo. In order to assess the role of thermal stresses we adopted the values at latitude 60°N for the high inertia/low albedo ($420 \text{ J/m}^2 \text{ K s}^{1/2}$ and 0.15, respectively) model since they serve as an upper limit with regards to thermal stress values and thickness of the stressed zone. In addition, we made the same calculations at latitude 45°N for comparison. The stress values were used to compute stress intensity factors K_I for different fracture depths using equation (3.3). Young's modulus for polycrystalline ice (an approximate estimate to a frozen soil) at Mars-like temperatures is given by the relation given by Gold (1958)

$$2.339 \times 10^{10} - 6.48 \times 10^7 T Pa \quad (3.7)$$

where T stands for temperature. For the depths under investigation in our analysis, temperature is not expected to vary, and so, T is chosen to be 180 °K, which is assumed to be the mean temperature of the Martian soil (Mellon and Jakosky 1993). Table 3.2 lists the values of the other parameters in our model. Equation (3.2) is used to compute the critical crack extension energy G_c for different depths. Finally, G is computed from K_I using equation (3.4) assuming plane strain conditions.

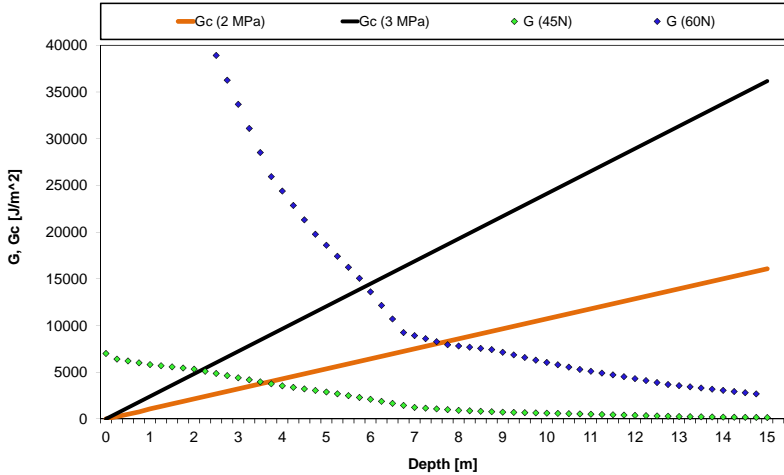


Figure 3.10: Variation of crack extension energy (G) with final crack depth for a high inertia case in latitude 60°N (blue diamonds) and 45°N (green diamonds). The depth where $G = G_c$ is assumed to be the final depth a crack can reach, which in the 60°N case is ≈ 6 m for a material with 3 MPa tensile strength (black solid line), and ≈ 7.5 m for a weaker 2 MPa material (yellow solid line). Similarly for the 45°N case, the final depths are 2 and 3.5 m, respectively. Lower latitudes or lower thermal inertias would lead to shallower crack limits.

3.5.3 Results

Figure 3.10 shows a plot of the results of the above described computation for a frozen soil with a tensile strength of 2 MPa and 3 MPa. The solid lines represent the crack extension energies computed from Mellon's results for thermal stress at latitudes 60°N and 45°N for various maximum depths of fracture penetration. The point of interest is the depth where the crack extension energy is not enough to sustain the crack extension process, or in other words, where G drops below G_c . The figure shows these depths to be 7.5 meters in the case of a 2 MPa material and 6 meters for a 3 MPa one at 60°N . At latitude 45°N these values are 2 meters and 3.5 meters respectively. Note that in either case, extension energies approach zero at a given depth. This signifies the transition from a tensile regime to a compressive one for the area under investigation, and represents to close approximation the maximum depth a crack would extend if the tensile strength of the material was completely ignored. This however, is not an accurate simulation of the problem at hand, and as such, our attention is focused on the lower realistic values. Considering the ratios reported in the literature ranging from 1:3 to 1:10 for crack depth versus crack separation, an upper limit of 18-23 meters in the 1:3 case and 60-75 meters in the 1:10 one can be determined for a frozen soil ranging in tensile strength between 2

and 3 MPa.

It should be noted that these are not absolute values; the maximum limits of polygon sizes should be related to the thermal stress fields (i.e. latitude and location in general), as well as material strength and its physical properties such as density and thermal conductivity. However, the fact that this analysis is made for latitude that exhibits one of the highest computed thermal stresses in addition to the model assumption of a high inertia (thus a thick stress field) means that the preceding values can act as upper limits to thermal contraction polygon diameters at current Martian climate conditions. It is also worth mentioning that the first set of results (assuming the 1:3 ratio) are in excellent agreement with a previous finite-element modeling of thermal contraction polygon sizes at the Phoenix landing site at 68° N (Mellon et al. 2008) in addition to mean diameters of such polygons on Mars (Levy et al. 2009). Similar calculations at 45° N strengthen our conclusions. Note how the upper limits for polygon size decrease considerably to 6-10 meters in the 1:3 case, and 20-35 meters in the 1:10 case. Similarly, lower thermal inertia values will lead to lower limits on polygon diameters since the high stresses will be concentrated at a shallower depth. A point worth mentioning at this stage is that our model assumes soil homogeneity. Heterogeneities within the material in question and zones of weaknesses are believed to be present but they are not expected to affect the overall soil properties by orders of magnitude.

From these results it can be concluded that most of the CFPs are simply too large to have formed with thermal stresses alone under current climatic conditions, and as such, require a higher and deeper stress regime to form. The remaining mechanism that fits the morphological investigations is desiccation. In that case, CFPs can act as excellent markers of dried-up bodies of water inside impact crater basins. This is an interesting outcome which is further discussed in the following section.

3.6 Discussion

We start this section by reviewing previous research on Martian paleolakes in general and impact crater lakes in particular. Next, the implications of our results are discussed, which includes highlighting other lake features that have been observed in craters among the CFPs. Finally, we discuss different formation mechanisms for crater lakes.

3.6.1 Crater paleolakes

Research on Martian lakes has always been linked to our understanding of the history of water on Mars. Ever since the discovery of channels and valleys on Mars in 1972 by the Mariner 9 (Masursky 1973), and the growing agreement in the scientific community that water must have been the key player in forming them, a large body of work has suggested that lakes or long standing bodies of water could have existed on the Martian surface having addressed the questions of their stability under current and past (perhaps warmer and wetter) conditions (e.g., Carr 1983, Carr et al. 1987, Squyres 1989, Altheide et al. 2009) as well as their possible locations (e.g., Scott et al. 1995, Wharton et al. 1995, Forsythe and Blackwelder 1998, Cabrol and Grin 1999, Orofino et al. 2009).

Soon afterwards, it was realized that compared to open, unconfined basins, lakes in

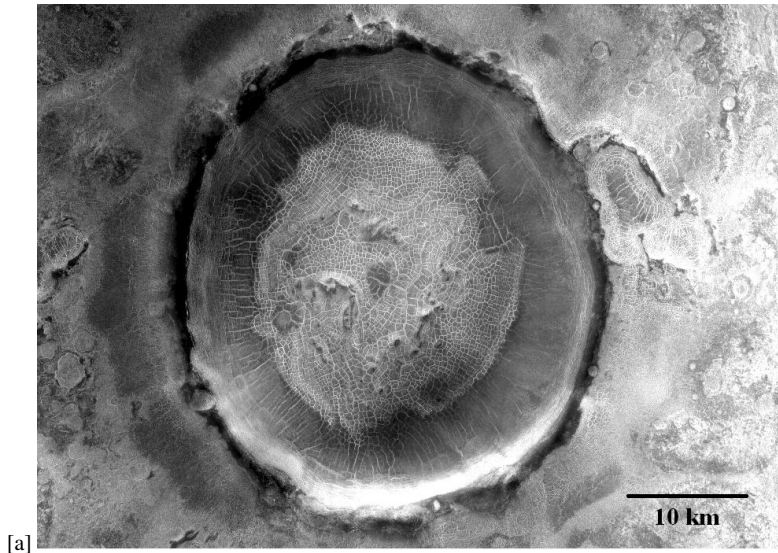
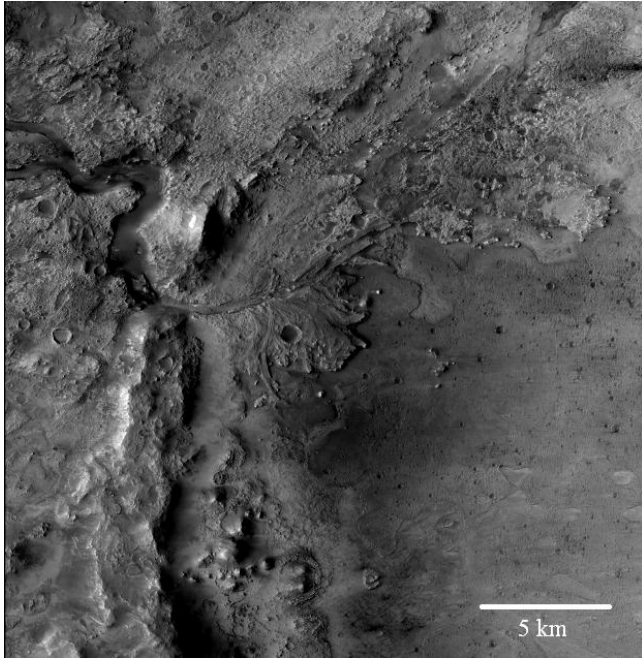


Figure 3.11: Examples of the features discussed in section 4.6.2. (a) An endogenic lake forms in a crater without inlet or outlet channels. (b) An exogenic lake has an inlet channel acting as a source like for example Jezero crater. The image also shows an example of a deltaic fan that shows distinctive layering in the high resolution images. (c) A clear example of a putative shoreline can be seen in Galdakao crater. Shorelines can be detected through a distinctive change in surface textures. (d) An example of a mound associated with CFPs in an unnamed crater. The mound is almost 150 m across. (Image IDs: (a) CTX: P16_007372_2474, (b) P03_002387_1987, (c) P17_007816_1652).

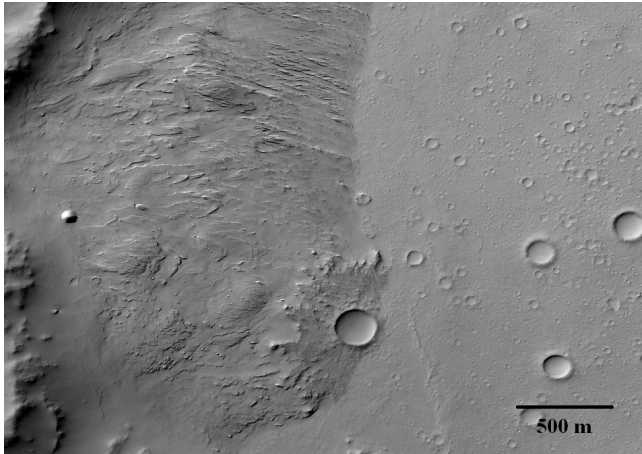
impact craters were more interesting targets from an exobiological point of view (Newsom et al. 1996, Grin and Cabrol 1997, Cabrol et al. 1999), in addition to facilitating the limnologic analysis due to their well-defined topography, clearer sedimentary features, better depth/diameter models, and more accurate estimates of sediment ratio content (Cabrol and Grin 1999). Detailed analysis has identified many sedimentary structures that can act as indicators of paleolakes. Examples include channels, lacustrine deltas, terraces, shorelines, mounds, evaporites, and layered sedimentary deposits (Cabrol and Grin 1999).

3.6.2 Survey results

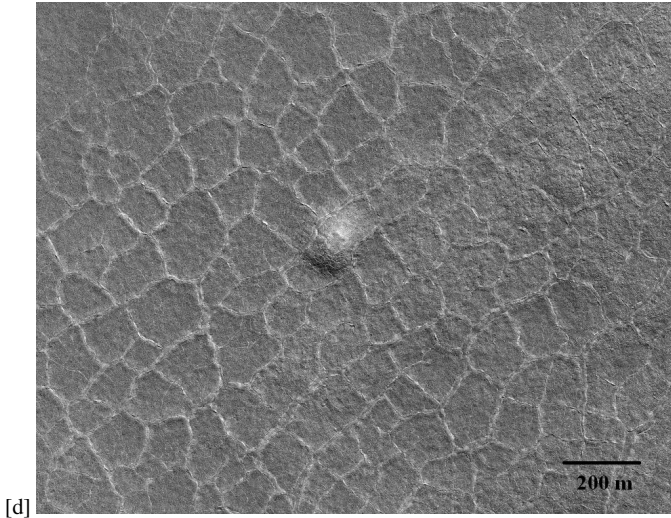
We conducted a search for paleolake-related sedimentary features as highlighted above using our CFP-containing crater database, including differentiating the craters that showed inflow channels breaching the crater walls from those that appeared to be closed isolated basins with no visible external source of water. Since such features are occasionally kilometer-sized, additional higher spatial images from the Thermal Emission Imaging



[b]



[c]



System (THEMIS) (Christensen et al. 2004) were used to facilitate detection. The survey reveals that out of the 262 craters in our database, only 20 craters (7.6%) show wall breaching by channels, with the rest being closed basins (Figure 3.11). Despite that, over 40% of the craters in the survey (109 craters) show at least one of the previously highlighted lake features, with 12.5% (33 craters) of them showing multiple features. Almost all breached craters show layering, terraces, lacustrine deltas and putative shorelines. Closed-basin craters however, are not expected to show features of running water such as deltas, and as such, they show mostly mounds, layering, and putative shoreline features such as ridges, bars, and troughs parallel to the crater rim. In addition, some craters in the high latitudes (especially in Utopia) show features similar to thermokarst pits (Costard and Kargel 1995). Since most of the sedimentary features are expected to be present only in breached craters, we also searched for gullies and fluidized ejecta. While gullies can be good indicators of ground water sapping, which can act as a potential internal source (Malin and Carr 1999), rampart craters directly indicate that the impact occurred in a liquid water/ice-rich environment (Mouginis-Mark 1987). Our survey shows that 88% (224) of the craters are rampart. Most of the non-rampart craters are large basins breached by channels. In addition, 12% (31) of the craters are gullied, with most of them situated between 40°N to 70°N and 35°S to 65°S. Additionally, almost all craters show small depth to diameter ratios in relation to fresh craters, and as such, it can be concluded that most of them contain sedimentary deposits which again suggests the existence of a water-enriched environment such as a paleolake.

3.6.3 Formation mechanism and ages of crater lakes

In light of these results, we can infer that most of the surveyed craters were occupied by lakes for some part of their history supporting the desiccation hypothesis for the formation of CFPs. Such crater lakes can be divided into two types depending on the source of water: 1) Exogenic lakes are formed by breaching of the crater wall with inflow channels and later settling of water and sediment in the crater basin. In some cases, the volume of inflowing water would exceed the holding capacity of the crater, and thus overflow or form outflow channels. A well-known example from this category is the MER Spirit landing site, Gusev Crater, where Ma'adim Vallis debouches (Grin and Cabrol 1997). Scott et al. (1993) produced a geologic map of the distinct volcano, Apollinaris Patera, and its surroundings, showing that Ma'adim Vallis may have breached the northern rim of Gusev Crater and emplaced fluvial deposits to the north of the impact crater basin. 2) Endogenic lakes are formed shortly after the impact process and can be the result of ground water sapping if the impact was relatively small, but sufficient in size to breach the ice/water table; alternatively, a lake could result from an impact-generated hydrothermal system if the target material was volatile rich, and the impact was large enough to sustain such a system (Newsom 1996, Rathbun and Squyres 2002, Abramov and Kring 2005). Considering that most of the craters in this study are isolated basins, we infer that impact-generated hydrothermal systems are the main formation mechanism for most of the putative lakes, though further investigation is merited to see whether processes such as precipitation or melting in a transient period of high obliquity could have contributed to the CFPs.

Determining the age of a crater lake with any degree of certainty is a difficult task. Exogenic lakes can form through various rates of ground water discharge ranging from slow to catastrophic. In addition, they can also form through episodes of glacial melt (Cabrol and Grin 2002). In either case, such lakes are expected to have formed during the Noachian Period (more than 3.5 Ga, Hartmann and Neukum 2001), coinciding with the formation of valleys and channels more prevalent than later periods (Carr and Head 2009). Other possibilities include certain periods of time when liquid water was allowed to persist on the Martian surface, perhaps through obliquity changes (Haberle et al. 2000) or transient changes in climate through magmatically-induced flooding such as related to the development of the Tharsis magmatic complex and ponding to form water bodies ranging from lakes to oceans in the northern plains (Baker et al., 1991, 2000; Fairén et al. 2003). Endogenic lakes, on the other hand, are expected to form shortly after the impact event, where there is still enough thermal energy to cause melting in the nearby cryosphere or generation of a hydrothermal system. This means that such lakes may have been present as recently as the Amazonian (3.4-2 Ga to present, Hartmann and Neukum 2001), which is the accepted age for most of the geologic features in the northern plains (Tanaka et al. 1995).

A key issue from an exobiological point of view is the lifetime of a crater lake. While we cannot infer with high certainty the life time of exogenic lakes, better estimates can be made for the endogenic ones, assuming a hydrothermal system to be the driving agent. In this case, the lake and the lifetime of the hydrothermal system are mainly dependant on the impact size, surface permeability, and water-rock ratios among other, but less significant factors. Considering the size distribution of craters containing CFPs, we can infer that hydrothermally-generated lakes can persist, even under current climatic conditions for

60,000-300,000 years such as in the case of an impact crater with diameters ranging from 30 to 180 km (Newsom et al. 1996, Abramov and Kring 2005). This may have significant consequences on the habitability of such lakes early in the Martian history.

Another point worth mentioning is the average trough spacing of CFPs in breached craters (i.e. exogenic lakes), which is ≈ 40 meters, remarkably lower than the global mean (≈ 120 meters). This could indicate that the eventual stressed zone after desiccation in the case of endogenic lakes was much thicker as it would have involved a lowering of the water table (similar to terrestrial cases) as the hydrothermal system cooled down, while in the case of exogenic lakes, if they were not as long-lived as their hydrothermal counterparts, the water-saturated crater infill deposits may have been significantly thinner, and as such, shallower troughs and smaller polygonal networks would be expected following desiccation. In a general context, polygonal sizes may deviate from the median size (≈ 120 meters) depending on the specific soil properties of the region, hydrologic history and ground permeability among other factors that influence the thickness of the stressed zone. Similar arguments may explain variations in desiccation polygon sizes on Mars that are not associated with impact craters. Two notable examples are the desiccated chloride-bearing deposits in the southern highlands (Osterloo et al. 2008, 2010) and clay-bearing layered deposits at Mawrth Vallis (Wray et al. 2008).

Chloride deposits are found scattered in many regions in the southern highlands. They are light toned, polygonally fractured, and lie within Late Noachian to Early Hesperian geological units. Polygons are 30 to 40 meters wide on average, with some reaching 75 meters (Figure 3.12). They frequently show subdivision into smaller 10-meter polygons. Chlorides commonly precipitate during the evaporation of surface water or groundwater and during volcanic outgassing. However, the polygonal fracturing makes a stronger case for evaporation of a standing body of water. On the other hand, the clay-bearing layered deposits in Mawrth Vallis (an outflow channel debouching into the Chryse basin) are also polygonally fractured. However, the polygons are 2 to 10 meters wide (Figure 3.12, right), with the overlying Al-clay-bearing strata showing even smaller polygonal fractures (referred to by Wray et al. (2008), as Units 3 and 2 respectively). Wray et al. (2008) conclude that these units post-date the Hesperian-aged outflow channel and may represent a later sedimentary layer draping the topography.

The larger polygonal fractures in the chloride-bearing deposits (Figure 3.12, left) point to a thicker stressed zone that formed as a result of evaporation of a standing body of water, and subsequent desiccation of water-saturated rock materials. Conversely, the layered deposits of Mawrth Vallis imply a thinner stressed zone and thinner water-rich sediments, thus probably more short-lived. The geological and historical context described above is in agreement with this hypothesis. While other factors should be affecting the thickness of the stressed zone such as material composition and permeability, nevertheless, this case study demonstrates how the size range of desiccation polygons can be indicative of the water history and conditions at the time of deposition.

3.7 Conclusions and outlook

A global mapping of CFPs was carried out using high-resolution images from MOC, CTX, and HiRISE cameras. We have also searched for geomorphologic evidence of aque-

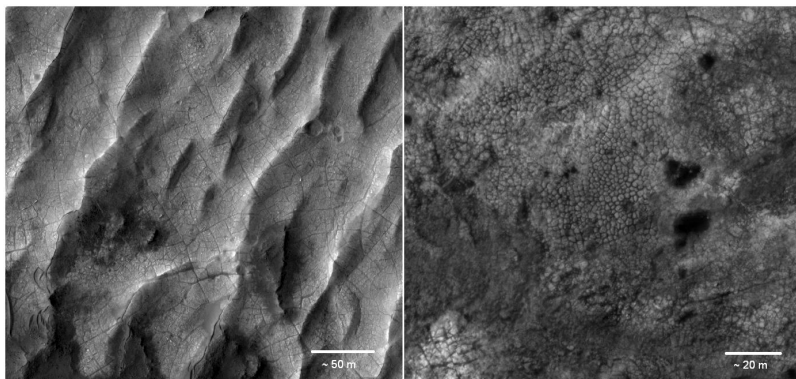


Figure 3.12: Other desiccation polygonal fractures on Mars. (left) Chloride-rich deposits at 38°S, 121°E. Polygons are 30-40 m wide (HiRISE image: PSP_003160_1410). (right) Mawrth Vallis, clay-bearing deposits. Polygons are 2-10 m wide (HiRISE image: PSP_002140_2025).

ous activity in the CFP-containing impact craters such as the formation of lakes through THEMIS data. The CFPs morphologically resemble thermal contraction polygons and desiccation cracks. Their global distribution extends to regions where water-ice is not expected to be stable near the surface. Past climatic variations due to obliquity changes can account for this distribution in principle. However, their size distribution is significantly different from that of thermal contraction polygons that are ubiquitous in the Martian high latitudes.

The analytical model based on fracture mechanics of crack extension in a frozen soil under current climatic conditions on Mars suggests that it is not possible to form polygonal networks with diameters larger than 75 meters with thermal stresses alone even under extreme conditions of thermal inertia, and ratios of fracture spacing to maximum fracture depth. More reasonable diameters fall between 18 and 22 meters, which is in the range of thermal contraction polygons on Mars, and in agreement with previous modeling attempts. As a result, we propose desiccation to be a primary contributor to the formation of intermediate-size polygons inside craters, while not ruling out contributions from thermal stresses. In fact, thermal stresses are thought to be the main mechanism in formation of the smaller polygonal fractures that subdivide the larger 100-200 meter polygons.

The desiccation mechanism entails that crater lakes or water-rich sediments existed inside impact craters. Such lakes are mostly endogenic with no apparent external source of water (i.e. those that are not breached by channels), and as such, are proposed to have been formed by hydrothermal processes or ground water sapping shortly after the impact event, though more work is necessary to determine other possible sources of water such as from the atmosphere or through melting at a transient period of high obliquity. The often identification of other geomorphologic features related to lake bodies associated with CFPs corroborates that the impact craters once contained lakes, and that their eventual desiccation significantly contributed to the polygonal-patterned ground.

The size variation of desiccation polygons can act as a proxy to the hydrologic conditions at the time of desiccation as has been discussed for the chloride deposits in the southern highlands and clay-bearing sedimentary units such as those in Mawrth Vallis and many breached craters, making it an innovative tool in studying Mars hydrologic history.

One of the plans to extend the work on CFPs was to look into the database of craters containing these features and further analyze those that had CRISM coverage (See Appendix A). It was hoped that it would be possible to emulate Marzo et al.'s (2010) efforts in CFP-filled impact craters (see section 1.6.3 for more details). However, as has been discussed earlier, most CFPs can be seen at high latitudes where seasonal frost or permanent ice highlights the features and aids in their detection. As a consequence, the presence of large quantities of water ice masks the weaker signals from hydrous minerals. In addition, the atmospheric contributions at higher latitudes are more complex limiting the efficiency of available data reduction tools that remove the atmospheric signal from the CRISM surface one. Another issue specifically related to Mars is that it is a very dusty planet. Dust storms have been observed for centuries. They tend to recur in southern spring and summer. Most are regional in extent, but in some years, as in 1971, they can be truly global. This results in the burial of rocky surfaces by thin dust layers, but may also lead to exposure of previously dusted terrains. Indeed, global thermal inertia studies indicate that almost 50% of the surface is covered by either bright unconsolidated fines or duricrust (Putzig et al. 2005). In addition, further analysis using high resolution visible images indicates that some regions of Mars even when exhibiting high thermal inertia values (as would be expected of bedrock as opposed to fine material) show high percentages (55-85%) of mantling (Newsom et al. 2007). Consequently, none of the craters in the high latitudes yielded significant results due to the previously mentioned reasons. However, some of the craters in the lower latitudes do show interesting mineralogic signatures and as such have been reported already by other workers in the field. For example, Antoniadi (Bandfield 2006), Jezero (Ehlmann et al. 2009), and Endeavor craters (Wray et al. 2009).

As a follow up in a different direction, we have been working on producing a numerical model for desiccation under current Martian climatic conditions to investigate the general conditions and soil properties that could allow CFPs to form on Mars. Since the results of this work are beyond the scope of this study, an outline of this work is presented in Appendix C for the interested reader. We now turn to magmatic-driven systems using another case study that is (at the time of writing) in the process of being published (El Maarry M.R et al. 2010, Searching for evidence of hydrothermal activity at Apollinaris Patera, Mar using Remote Sensing, Icarus, submitted).

4 Magmatic-Driven Hydrothermal System Case Study: Apollinaris Patera

4.1 Introduction

The geologic record of Mars, as on Earth, likely includes magmatic-driven hydrothermal activity (Dohm et al. 1998, 2008, Schulze-Makuch et al. 2007). This is deduced from the widespread occurrence of impact, volcanic, and water-related features on the surface, which are often temporally and spatially associated, as has been discussed in chapter 1. The presence of massive magmatic complexes such as Tharsis and Elysium in addition to other diverse evidence of volcanism, along with the rich hydrologic history, point to long-term hydrothermal activity.

Both impact- and magmatic-driven hydrothermal systems represent locations of exobiological interest due to the ability of such environments to sustain life on Earth (Valentino et al. 1999, Glamoclija et al. 2004, Parnell et al. 2010). As a result, many efforts have been devoted to locating optimum hydrothermal targets on Mars for exploration (e.g., Newsom 1980, Newsom et al. 2001, Dohm et al. 2004, Schulz-Makuch et al. 2007). The work presented here is inspired by such efforts, particularly focusing on Apollinaris Patera, which has already been identified as a site of potential magmatic-driven hydrothermal activity on Mars (Schulze-Makuch et al. 2007). In this study, we test the hydrothermal hypothesis by looking for key indicators of such activity using multiple remote sensing datasets.

4.2 Geological, physiographical, and environmental settings of Apollinaris Patera

Apollinaris Patera (Figure 4.1) is a prominent 200 km-wide and 5 km-high shield volcano located near the boundary between the northern plains and southern highlands (174.4°E, 9.3°S) and approximately 200 km north of Gusev Crater, the target of investigations by the Spirit rover (Squyres et al. 2004, Arvidson et al. 2006, 2008, 2010). It contains a multi-stage caldera complex approximately 80 km in diameter. The northern and eastern flanks of the edifice are surrounded by the Medusae Fossae Formation (MFF, Scott et al. 1993) and terminate with clear scarps. The southern flank, however, is characterized by extensive fan deposits that drape parts of the volcano from summit to base. The western

flank is surrounded by mounds and knobs forming a terrain similar to the chaotic terrain found elsewhere on Mars such as those that source the channels of the circum-Chryse outflow channel system (e.g., Rodriguez et al. 2005) which debouch into Chryse Planitia.

Apollinaris Patera is reported to have been constructed by both pyroclastic and effusive eruptions (Robinson et al. 1993). The age of emplacement is estimated to range from the Late Noachian epoch to the Late Hesperian epoch based on both stratigraphic relations and impact crater statistics (Scott et al. 1993, Robinson et al. 1993, Greeley et al. 2005), or 3.8-2.9 Gyr, estimated absolute ages based on Hartmann and Neukum (2001). The first detailed geologic mapping of Apollinaris Patera was carried out using Viking images (Robinson et al. 1993, Scott et al. 1993). Robinson et al. (1993) concluded that the volcano has two surface materials: old, easily eroded edifice material, and more recent, and competent fan deposits draping the southern flank (Figure 4.2). Consequently, they have proposed that large-scale explosive activity occurred during the formation of the main edifice while the fan deposits were subsequently emplaced by lavas with low eruptive rates similar to pahoehoe lavas on Earth. On the other hand, Scott et al. (2003) concluded that the initial lava flows were effusive at first forming the lower dome followed by more explosive pyroclastic events forming the upper steeper part of the edifice. At some point, depletion of the magmatic chamber led to caldera collapse, and later eruptions filled the collapsed caldera and overflowed through a small notch in the southern margin to form the fan deposits.

The Viking-era mapping investigations pointed to the Apollinaris Patera shield volcano and surrounding region as a potential environment of significant magma and water interactions. This includes possible presence of pyroclastic deposits, breaking up of parts of the volcano to form chaotic terrain, and a network of valleys along the southern margin of the above-mentioned Hesperian-aged fan deposit (Scott et al. 1993). Evidence for water enrichment in the Apollinaris Patera and surrounding region also includes a prominent scarp that forms part of the base of the volcano, similar to the basal scarp of Olympus Mons which has been interpreted as a wave-cut platform (Scott et al. 1993), and numerous valleys that dissect the caldera walls at the summit of the prominent volcano. A long-term, magma-water interaction hypothesis is consistent with Gamma Ray Spectrometer-based elemental information that indicates elevated hydrogen and chlorine when compared to the rest of the equatorial region of Mars (Boynton et al. 2004, Keller et al. 2006, Dohm et al. 2008). A hypothesized ancient ocean existing during at least part of the Noachian Period and possibly extending into the Early Hesperian epoch, would have covered approximately 1/3 of the surface of Mars (Clifford and Parker 2001, Dohm et al. 2009a, DiAchile and Hynek 2010), and would have inundated the Apollinaris Patera surroundings.

Follow-up works on Apollinaris have utilized higher-resolution image data and new observation techniques to examine its relationship with the basalts of the Gusev crater plains (Lang et al. 2010), assess possible contributions of Apollinaris to the MFF deposits (Kerber and Head 2010), and study the magnetic anomalies associated with the region (Langlais and Purucker 2007, Hood et al. 2010). In this work, we build upon the earlier mapping efforts which focused on the volcano and its surroundings making use of the existing image databases (appendix D and Figure 4.1) from the Thermal Emission Imaging System (THEMIS, Christensen et al. 2004), the narrow angle Mars Orbital Camera (MOC, Malin et al. 1992), the Context Imager (CTX, Malin et al. 2007), and the

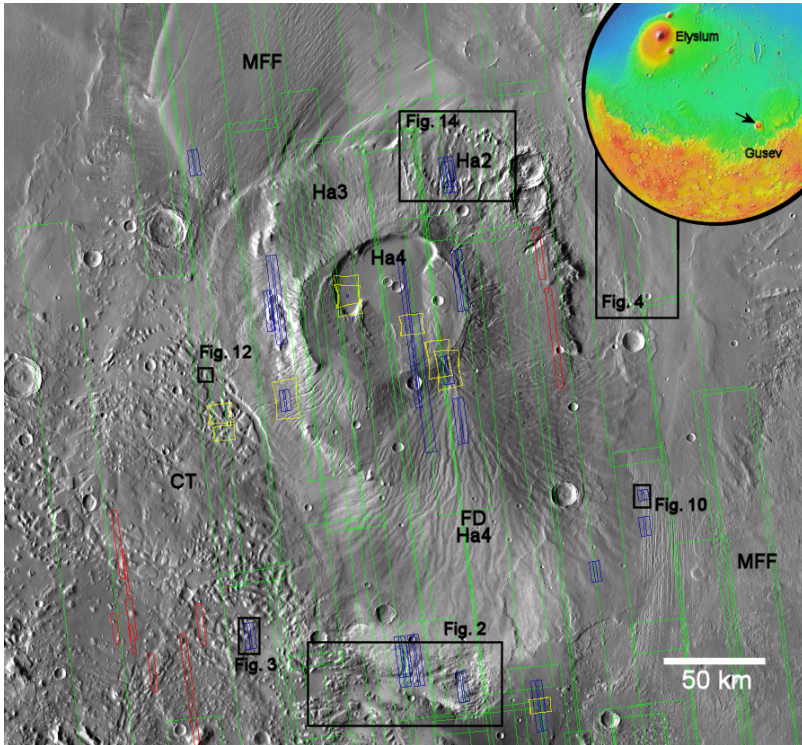


Figure 4.1: Visual THEMIS mosaic of the Apollinaris Patera and surrounding terrain. Apollinaris occurs near the boundary that separates the northern plains from the Southern highlands. Medusa Fossae Formation (MFF) partly surrounds the shield volcano to the north and east, and chaotic terrain (CT) is prevalent to the west of the volcano. The main construct is almost 200 km wide, displaying a caldera complex at its summit that is almost 80 km in diameter. The volcano is also notable for the extensive fan deposits (FD) that drape the southern flank and appear to originate from a small channel that dissects the southern rim. Also visible are the ground tracks of high resolution data used in this study. Blue, green, yellow, and red tracks correspond to HiRISE, CTX, CRISM, and MOC data, respectively. As can be seen, while the main edifice is well covered, there is a considerable lack of images in the chaotic terrain located to the west of the shield volcano, and to a lesser degree, the proximal parts of the eastern MFF deposits. MOC images were used when needed to compensate for the lack of CTX images or bad visual conditions. As result, only a partial subset of the entire MOC database was used (See Appendix D for information on the image datasets).

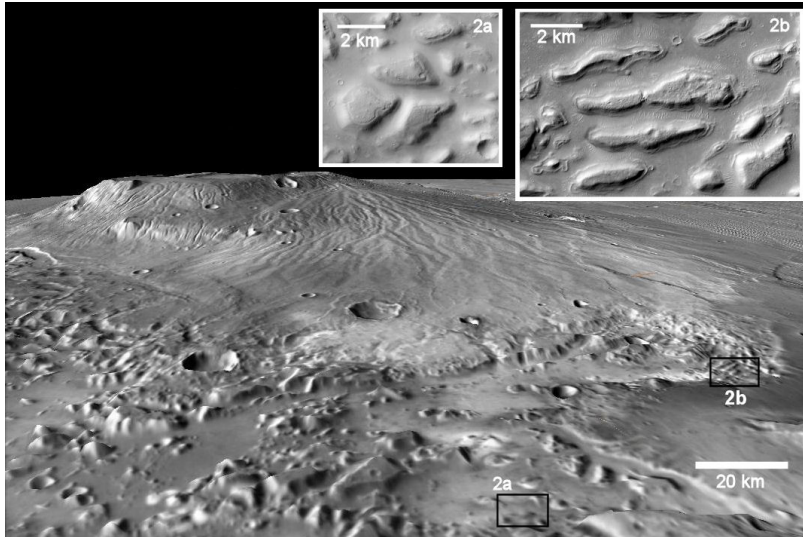


Figure 4.2: Digital terrain model (vertical exaggeration: 3x) for the Southern flank of Apollinaris Patera, the associated fan deposits and the large valley system resembling out-flow channels in the circum-Chryse region. The valley system is a wide depression reaching 20 km wide at some areas and 500 meters deep, extending westward for almost 120 km (Image Credit: Google Mars). Inset: Several large blocks situated in the valley show streamlined features and possible terracing. Image IDs: (2a): CTX P15_007091_1668 and (2b): CTX P18_007882_1703.

High Resolution Imaging Science Experiment (HiRISE, McEwen et al. 2007) cameras (approximately, 16-40m/pixel, 1.5-20m/pixel, 6 m/pixel, and 25 cm/pixel, respectively), topographic data from the Mars Orbiter Laser Altimeter (MOLA, Smith et al. 2001), and spectral data from the Compact Reconnaissance Imaging Spectrometer for Mars (CRISM, Murchie et al. 2007). Our primary objective is to assess the role of Apollinaris in forming an extensive hydrothermal system in a region that could be of significant interest for future in-situ exploration. We address this objective through a detailed examination of a set of criteria used for identifying candidate hydrothermal sites on Mars such as Apollinaris Patera (Schulze-Makuch et al. 2007). A discussion of the relevant criteria is followed by our findings.

4.3 Criteria for locating hydrothermal systems on Mars

Schulze-Makuch et al. (2007) made use of the recent improvements in data quality (i.e., Mars Global Surveyor and Mars Odyssey) to observe distinct geologic, paleohydrologic, paleotectonic, topographic, geophysical, spectral, and elemental signatures on the surface

of Mars in search of sites of potential hydrothermal activity. In doing so, they proposed a set of criteria that a certain location should display in order to be deemed a location with high hydrothermal activity potential. These criteria include: (1) evidence of action of liquid water through erosion; (2) evidence of volcanic constructs and/or lava flows; (3) evidence for a center of magmatic-driven tectonism; (4) topographical depressions hypothesized to be the result of structurally controlled collapse and/or rifting; (5) evidence for impact events in ice-rich regions; (6) presence of minerals that usually have a hydrothermal origin or that are indicative of hydrothermal alteration; (7) geological similarity to hydrothermal analog environments on Earth; and (8) geomorphological evidence for magma/water interaction. We have added criterion (8) to the previously published ones by Schulz-Makuch et al. (2007). In the following sections, we discuss how these criteria apply to Apollinaris Patera and its close surroundings.

4.3.1 Action of liquid water

One of the most prominent features around Apollinaris is the large valley system at the distal margin of the southern flank and the chaotic terrain located to the west of the shield volcano. The valley system has widths and depths reaching 20 km and 500 m, respectively (Figure 4.2), and appears to spread out from a single source region at the southern margin of the fan deposits and then extends westward for almost 120 km. Its morphology is comparable to the outflow channels surrounding Chryse Planitia, although being orders of magnitude smaller. This includes scattered islands within the valleys, which display flow features such as tear-drop shapes and terraces. Parts of the fan deposits appear to have been separated from the volcano related to the formation of the channel system.

Chaotic or knobby terrain (Scott et al. 1993), which occurs to the west and southwest of the shield volcano, is characterized by mesas with heights and widths that range from 200 to 300 m and 5 to 10 km, respectively. The orientation and shape of blocks nearest to the western flank strongly suggest that they broke off from the main edifice. The southwestern mesas occasionally display terraces, possibly attributed to differential erosion by wind and/or water. Topographic lows among the mesas are usually smooth in appearance, but are occasionally marked by small pedestal or rampart craters (Figure 4.3).

Another feature, which marks water activity in and around the shield volcano, is a valley system dissecting the MFF deposits east of the main edifice (Figure 4.4). Scott et al. (1993) mapped and characterized this system using Viking data as "material deposited by flowing water surrounding ridges that are eroded remnants of the MFF" and assigned it an Amazonian age. Close inspection using CTX images supports this hypothesis and allows us to further track the extent and source of the channel system (Figure 4.5). The system, which has a length nearing 90 km, appears to source from a ≈ 40 -m-deep depression (Figure 4.6), extending northwards with an average slope of 0.5% (i.e. decreasing by 5 m in elevation per km). Narrow (≈ 100 m wide) valleys (Figure 4.7) radiate from the depression and coalesce to form the wider (≈ 1 km wide) part of the valley system that appears to empty into another depression located northeast of Apollinaris. In addition, the main valley displays features that indicate a fluvial origin such as meandering, braiding, and streamlined structures (Figure 4.8). The overall morphology of the valley system is strongly indicative of a groundwater-fed sapping system (Gulick 2001).

There are many driving forces that could initiate this channel system with the most

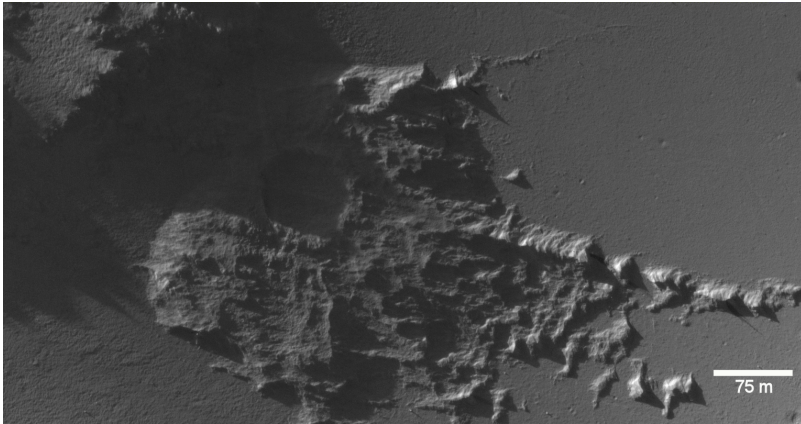


Figure 4.3: An excellent example of a 70-meter pedestal crater. Image is taken with HiRISE camera. The crater is situated in the chaotic terrain, and shows considerable erosion (probably by wind) of the ejecta deposits. Such craters are indicative of the presence of volatiles in the near surface. Image ID: HiRISE, PSP_009451_1675.

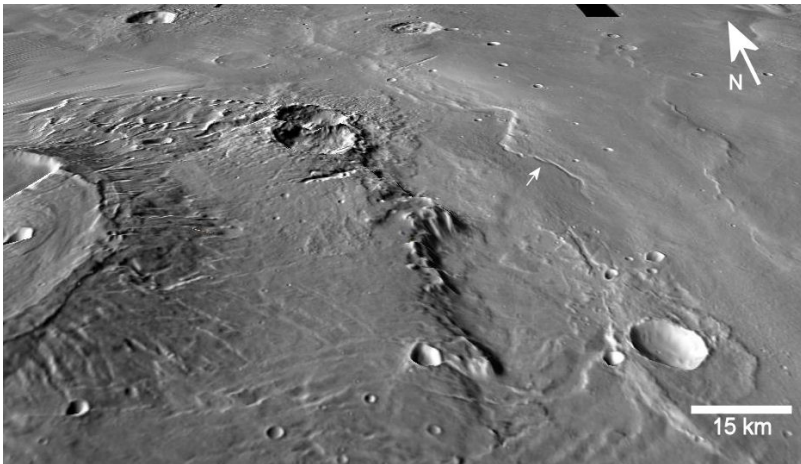


Figure 4.4: Digital terrain model (vertical exaggeration: 3x) of the valley system dissecting the MFF east of Apollinaris. The large valley system previously described by Scott et al. (2003) using Viking images is visible here. Higher resolution CTX images show that smaller tributaries coalesce to form a larger valley. The possible source region of the channel is located near a fault system and a 12 km-wide impact crater (see text). Image credit: Google Mars.

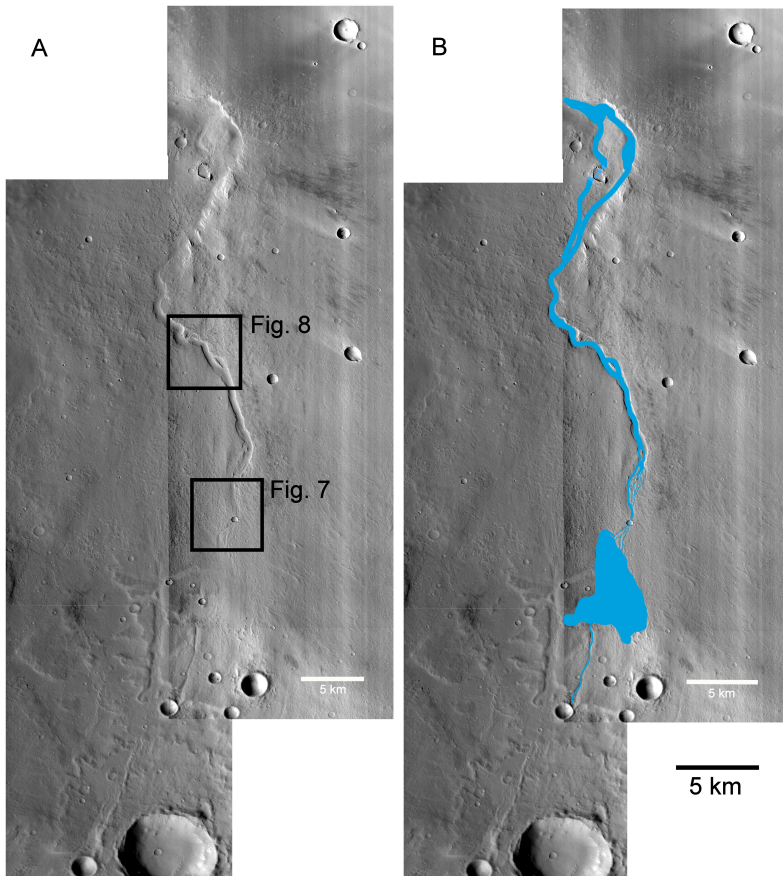


Figure 4.5: (a) CTX mosaic of the putative fluvial channel that occurs east of Apollinaris. High-resolution data facilitates the tracing of this channel and its possible source. (b) Highlight of the putative channel system which extends more than 90 km in length. Such a system may have originated through magmatic- or impact-driven hydrothermal activity or tectonic instability. The overall morphology of the valley system is strongly indicative of a groundwater-fed sapping channel system (see text). Image IDs: B09_013288_1724, and P12_005535_1732.

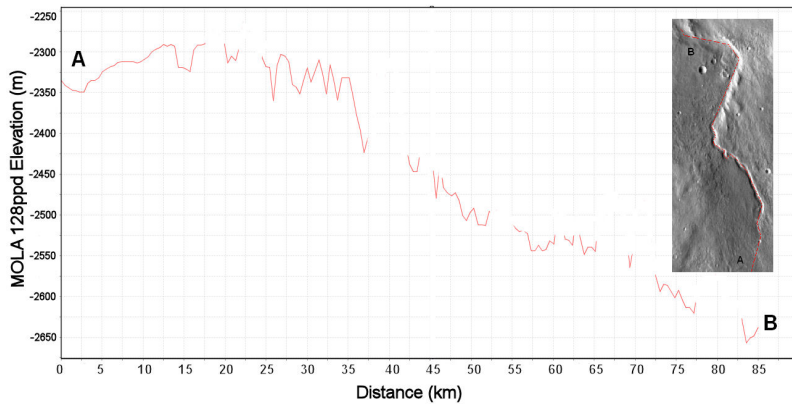


Figure 4.6: MOLA profile of the channel system, including the putative source region that can be seen at point "A" in the profile. The total average slope is 0.5%. The apparent missing points have been manually removed, as they show abnormal spikes as a result of the MOLA resolution limitations and errors arising from the manual aligning of the profile to coincide with the valley floor.

significant being a hydrothermal system formed by magmatic intrusions from Apollinaris Patera. Previous works have discussed the possible role of magmatic-driven hydrothermal systems in forming fluvial channels on Mars due to the apparent spatial and temporal correlation of fluvial erosion with volcanic activity (e.g., Gulick and Baker 1989, 1990, Tanaka et al. 1998, Baker et al. 2001) in addition to numerical simulations supporting this hypothesis (Gulick 1998). Other possibilities would be tectonic instabilities caused by seismic activity related to a system of faults and/or the formation of a 12-km-wide impact crater (10 km and 20 km to the west, respectively). The impact crater event could have triggered the reactivation of basement structures and associated hydrothermal activity-induced flooding, and dissection of the MFF deposits.

An alternative hypothesis for the origin of the channel is dissection through volcanism. Indeed, fluvial and volcanic channels can display similar characteristics such as sinuosity, braiding, and terracing (Leverington 2004, Bleacher et al. 2010). However, we favor a fluvial origin based on the presence of the abovementioned features, which are more common among fluvial channels than volcanic ones, in addition to the absence of compelling evidence for volcanism such as the presence of a topographic "cap" in the source region of the channel or any visible rootless vents along the channel (Bleacher et al. 2010).

4.3.2 Evidence for magma/water interaction

4.3.2.1 Mounds

Mounds occur on the flanks of the Apollinaris Patera shield volcano and its surroundings. Several display distinct central depressions (Figure 4.9). They form two distinct groups:

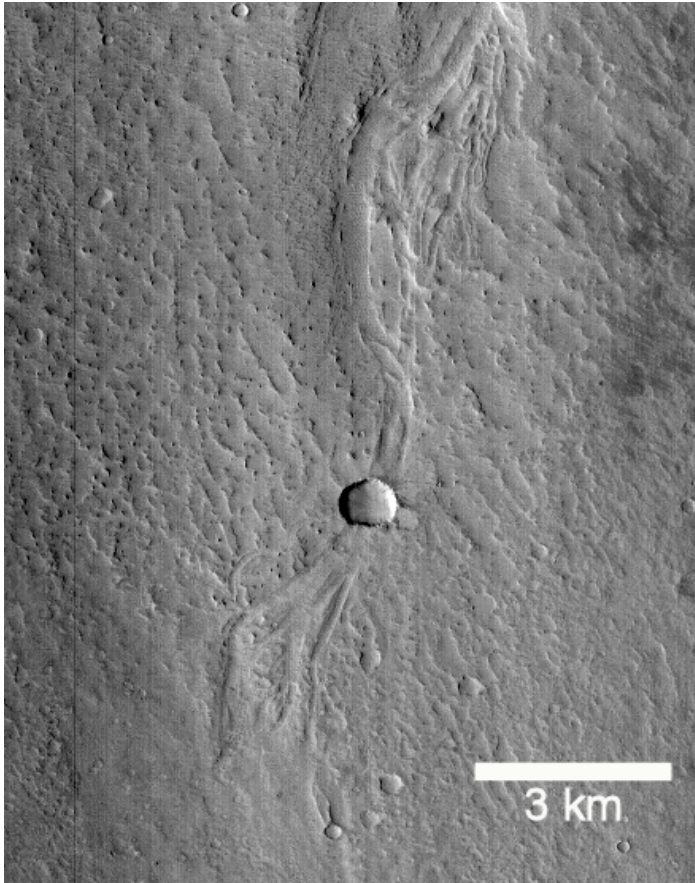


Figure 4.7: CTX image displaying evidence of small branching channels that appear to source from an ancient lake that coalesced into the larger channel, consistent with Viking-based observations (Scott et al. 2003). The channels have been modified by the impact crater event. Image ID: CTX: P12_005535_1732_XI_06S183W.

large (200m to 3 km in diameter) isolated structures mainly situated in the chaotic terrain and smaller (100m-sized) mounds forming distinctive clusters situated on the northern and eastern flanks of the volcano and in the MFF deposits located to the north of the volcano (Figure 4.10). Mounds and pitted cones are a common feature on the Martian surface, especially prevalent in the Vastitas Borealis Formation of the northern plains (Tanaka et al. 2005). Tharsis-derived floods are proposed to have contributed to the inundation of the northern plains to form large water bodies ranging in size from lakes

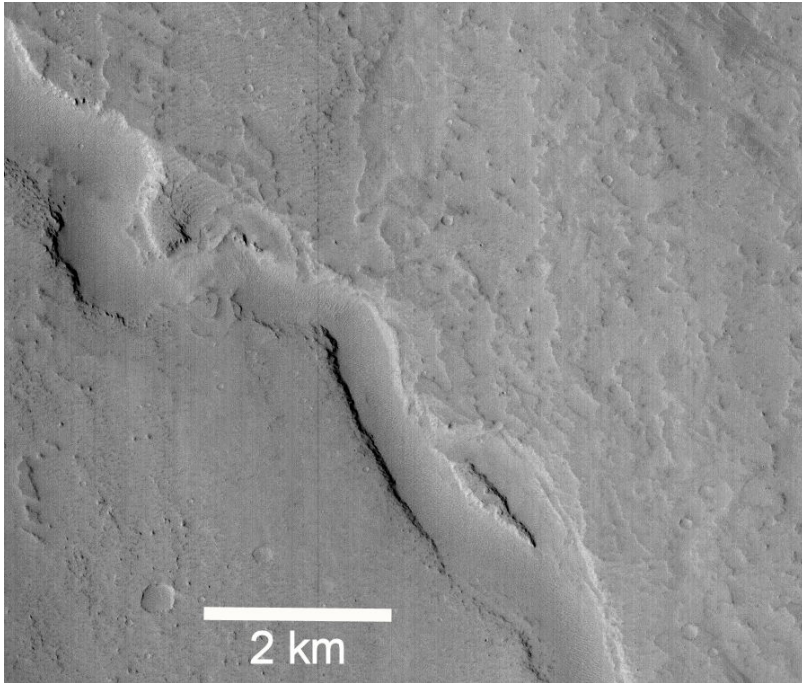


Figure 4.8: CTX image showing the channel system with typical fluvial signatures such as braiding, streamlined features, and meandering. Image ID: CTX: P12_005535_1732.

to oceans (Baker et al. 1991, Fairén et al. 2003, Dohm et al. 2009a). These flooding events, which resulted in the dissection and removal of kilometers-deep crustal materials in the cratered highlands, are suspected to have contributed to the emplacement of hyperbyssal flows and related constructional landforms such as mud volcanoes (e.g., Ori et al. 2000, Skinner and Tanaka 2007, Allen and Oehler 2010) and associated piping structures (Mahaney et al. 2004), particularly in the Vastitas Borealis Formation, from the release of entrained volatiles to the surface. While volatile-release features may aptly explain many of the constructional features, cinder cones (Scott et al. 1995), pseudocraters related to the interaction of ground ice or water with volcanic flows (Carr 1986), pingos and ice-cored ridges (Lucchitta 1981, Rossbacher and Judson 1981), or mounds formed by the disintegration of stagnant ice covers (Grizzaffi and Schultz 1989), are some of the Viking-era-proposed mechanisms that cannot be ruled out as possible explanations for the formation of some of the conical hills.

Viking-era hypotheses for the possible formational mechanisms of the mounds can be improved through detailed investigation of the morphology, geological context (e.g., spatial and temporal associations among materials and other landforms), and surface features such as thermal inertia, albedo, and distinctive mineralogical signatures, using higher

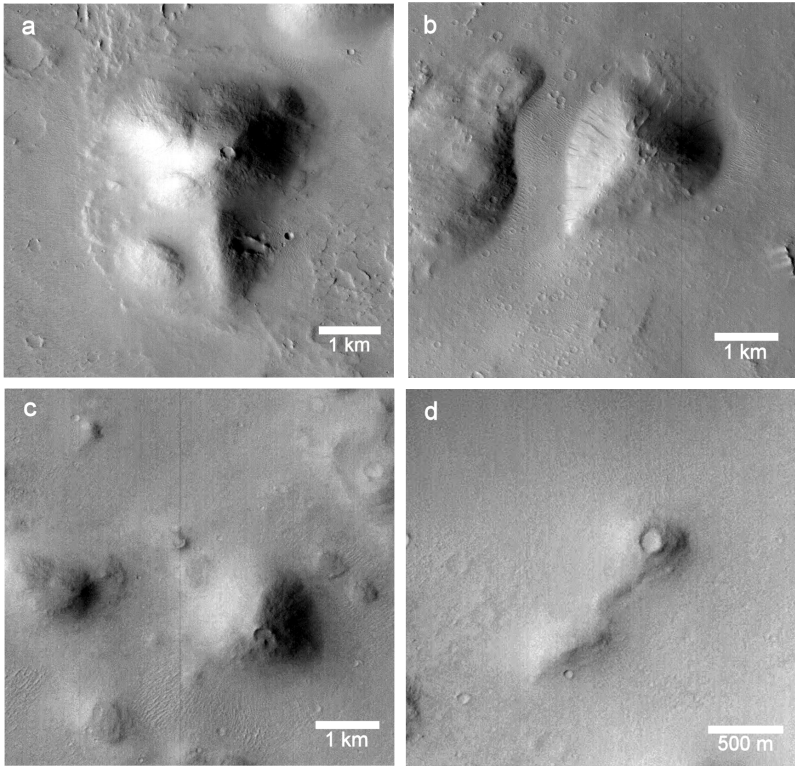
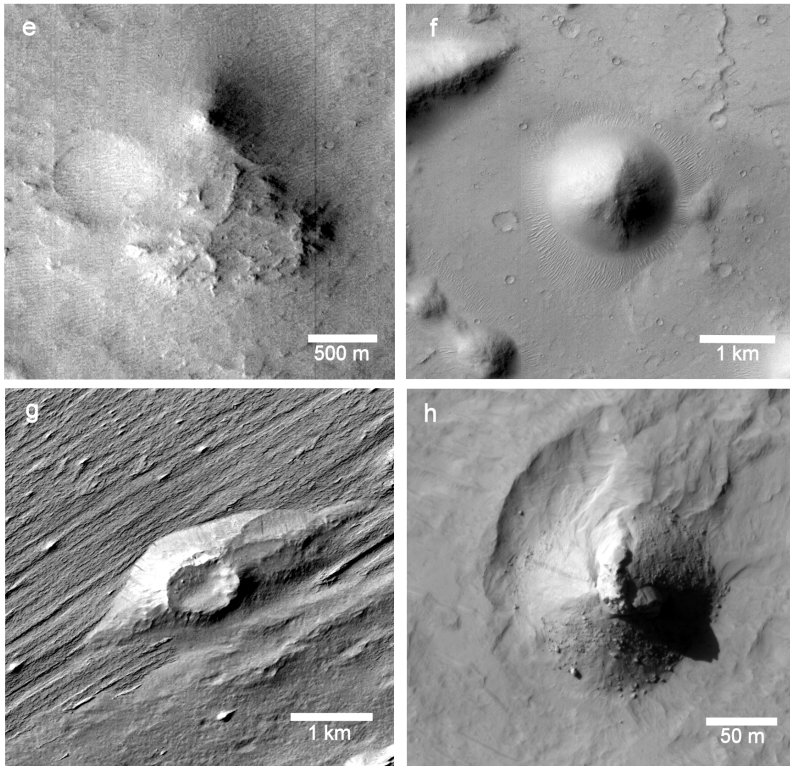


Figure 4.9: Examples of mounds observed at Apollinaris. The mounds range in size from 0.1 to ≈ 3 km in diameter and have variable shapes. Shadow analysis reveals a variation in width to height ratio, though quantitative information cannot be determined. The mounds form two distinct groups: Large 0.2 to 3 km-sized isolated structures that are pitted at times (d, e, and g), and clusters of smaller (100 m-sized) cone-like structures located on the northern flank of the main edifice and close to the MFF. Some appear to be spatially associated with faults and fractures, possibly indicating basement structural control. The variable morphologies can be indicative of different formation mechanisms. Image IDs: (a, b and e): P08_003966_1721, (c and d): P13_006234_1664, (f): P15_007091_1668, (g): P16_007236_1754, (h): PSP_007671_1695, and (i): P18_007882_1703. All images are CTX images except for (h) which is an image taken by HiRISE for a 100m-wide mound located on the boundary which separates the fan deposits and the wind-etched MFF materials in the east. Materials appear to be pyroclastic in origin. This structure could be either a cinder cone or a tuff cone.



quality and resolution data. Though the mounds on and close to the volcano are generally too small to accurately determine the geometric shape using MOLA topography, in addition to a lack of CRISM coverage of the mounds, the thermal inertia and albedos can give clues to their origin.

The mound-like features are characterized, in general, by relatively higher brightness temperatures with respect to their surroundings in night-time THEMIS images (Figure 4.11). This likely indicates that the mound-forming materials have higher thermal inertia values than those of the surrounding materials. However, quantitative measurements of thermal inertia derived from the THEMIS images (Ferguson et al. 2006) for some of the mounds yield low thermal inertia values in the range of $90\text{--}215 \text{ J m}^{-2}\text{K}^{-1}\text{s}^{-1/2}$ (Table 4.1). Such values correspond to a dusty component or indurated fine sand at best covering at least the top 2 cm of the surface. These values argue against igneous volcanism as a strong candidate for the formation of the mounds because relatively fresh solidified lava flow and pyroclastic (e.g., bombs) materials are expected to yield relatively higher thermal

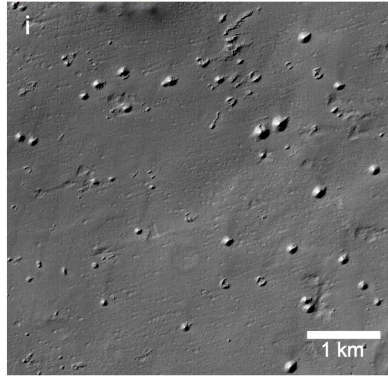


Table 4.1: Derived thermal inertia values for a number of the mounds found around Apollinaris. Generally, thermal inertia values are low indicating fine-grained sand or variably-indurated dusty material. Images used for derivation of thermal inertia are THEMIS-IR images I31987009 for first two mounds and I172000013 for the third one. Thermal Inertia values supplied by Robin Ferguson.

Latitude	Longitude	Thermal Inertia ($\text{J m}^{-2} \text{K}^{-1} \text{s}^{-1/2}$)
-7.39	172.36 E	112 ± 22
-8.94	172.62 E	187 ± 17
-11.91	173.82 E	153 ± 13

inertia values when compared to surrounding materials. Such features make cinder cones, tuyas, tuff cones, maars, and rootless cones weak candidates. In addition, tuff cones and maars are usually characterized by large vent to base diameter ratios (≈ 0.5 , see Farrand et al. 2005) as a result of their explosive formation. Similar to their possible terrestrial counterparts, large vent structures which occur in the northern MFF deposits (see figure 4.9g) have vent to base diameter ratios of ≈ 0.7 . The rest of the mounds in the Apollinaris Patera region, however, exhibit an order of magnitude smaller ratio (0.09 on average). Nonetheless, we cannot rule out the previous possibilities since explosive eruptions are expected to yield large quantities of fine material that would mask the underlying surface.

Non-volcanic candidates are also possible such as mud volcanoes, pingos, and piping structures formed from the migration of fluids such as in the case of springs. Mud volcanoes are the result of gas discharge which is usually accompanied with non-explosive effusion of soft and wet sediments. Some mud volcanoes on Earth are known to reach diameters of 4 km and heights of ≈ 500 m such as the ones in northern Irian Java, New Guinea (Williams et al. 1984) and the submarine Gelendzhik mud plateau in the crest of the Mediterranean Ridge (Limonov et al. 1996) in addition to exhibiting small pits or vents. As such, a mud volcano origin for the Apollinaris Patera mounds is a strong possibility. Mud volcanoes, for example, should exhibit low thermal inertia, similar to the

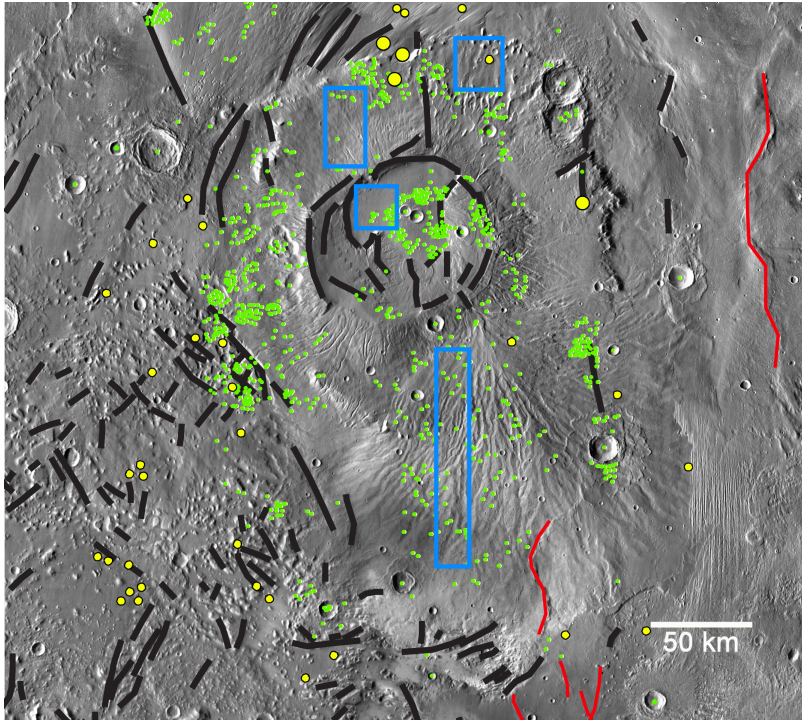


Figure 4.10: Visual THEMIS mosaic of the Apollinaris Patera and surrounding terrain showing distributions of isolated mounds (small yellow circles) and clustered ones (large yellow circles), impact craters with associated fluidized ejecta (green) which were identified using CTX images, thereby explaining the apparent lack of craters in the chaotic terrain where CTX images are nonexistent (see Figure 4.1), lineaments interpreted to be faults, fractures, and scarps formed by tectonism, collapse, and/or erosion (black lines), wrinkle ridges (red lines), and areas where crater counting was performed (blue boxes).

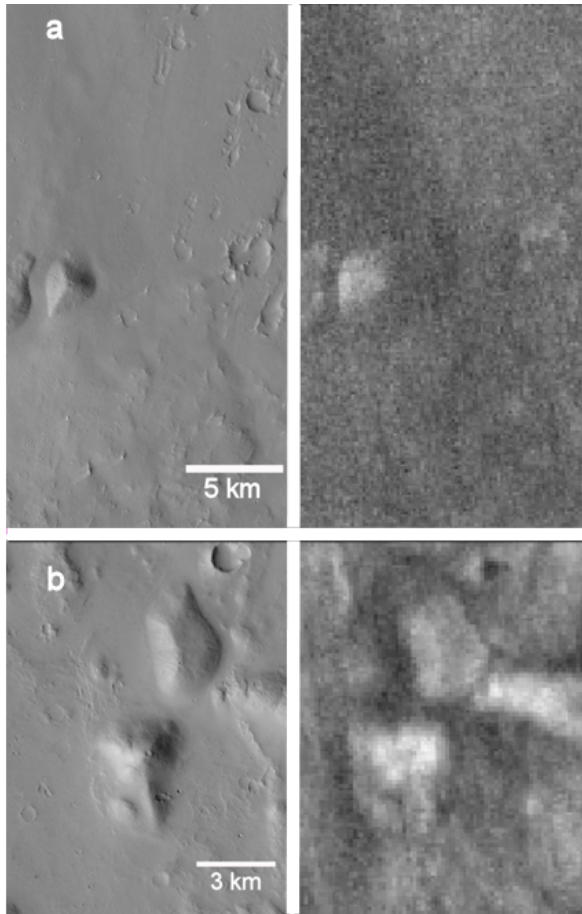


Figure 4.11: Night-time infra-red data for some of the Apollinaris mounds (locations: 7.39°S, 172.36°E, and 11.91°S, 173.82°E, respectively). Mounds appear to have a higher temperature than the surrounding terrain thereby implying a higher thermal inertia. Nevertheless, quantitative estimates reveal low absolute thermal inertia values (see Table 4.1) corresponding to fine sand material or variably indurated dust covering the upper 2-4 cm of the surface. Images IDs: THEMIS-IR (a) I31987009 and (b) I172000013.

Apollinaris Patera mounds as noted above. Indeed, our thermal inertia values correlate well with previous estimates of putative mud volcanoes in Acidalia Planitia and Cydonia Mensae (Farrand et al. 2005). Additionally, some mounds exhibit flow features similar to those associated with mud volcanoes on Earth and possible mud volcanoes on Mars (Fig-

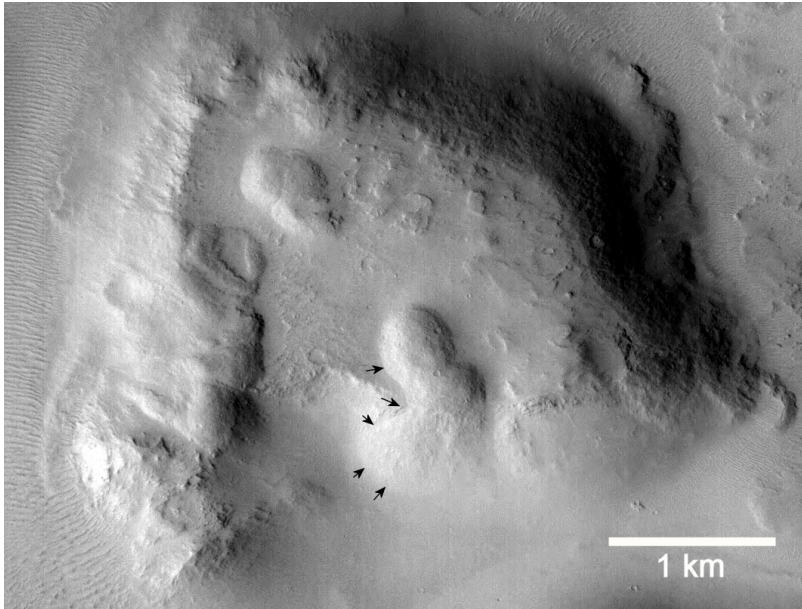


Figure 4.12: Possible flow features at the top of a mesa within the chaotic terrain, materials appear to originate from a point source or a fissure which is now completely buried, and extending outwards to produce a flow-like feature over the mesa's scarp.

ures 4.9 and 4.12, Oehler and Allen 2010, Komatsu et al. 2010), however, the mounds do not appear to be associated with sedimentary basins.

Pingos are small hills with cores of ice in periglacial environments, formed by the injection and freezing of pressurized water (Dundas and McEwen 2010). Though they have similar dimensions to the ones in the Apollinaris Patera region, there are several reasons why a pingo origin is unlikely. For example, whereas pingos usually often exhibit radial fractures due to its growth, such features have not been observed in the Apollinaris mounds. In addition, the surfaces of terrestrial pingos are composed of the same materials as their surroundings, therefore exhibiting uniform albedo and thermal properties, which is not the case for the Apollinaris Patera mounds. Finally, other periglacial features associated with Apollinaris have yet to be identified using existing data. However, a pingo origin cannot be ruled out, as Apollinaris Patera and its surroundings have been noted to be a water-enriched region (Scott et al. 1993).

Finally, both hot and cold springs can form extensive evaporite deposits around their sources. Hot springs can also erupt water in the form of geysers. As described and interpreted in Vernal crater of the Arabia Terra region (Allen and Oehler 2008), geysers and springs can have various shapes and sizes similar to the ones in Apollinaris Patera region. On Earth, they can display pits at their summits, and they usually have high

albedos on account of their mineralogy with respect to the hot materials. As a result, springs and geysers may be good candidates for the smaller mounds.

In conclusion, the distribution and variable morphologies of mounds in the Apollinaris Patera region may suggest multiple formation mechanisms, with most of them pointing to past and possibly recent hydrothermal, phreatic, or glacio-volcanic activity. The spatial association among other features such as faults and fractures and materials such as those that compose the construct and the chaotic terrain and MFF suggests that there is likely more than one progenitor with many candidate mechanisms indicating volatile enrichment at some time in the past.

4.3.2.2 Possible lahars

Volcanic mudflows (lahars) have been documented on Earth where eruptions have occurred in water/ice-rich zones, some with catastrophic results. Lahars can be produced through 5 mechanisms (Major and Newhall 1989): (1) scouring and melting by flowing pyroclastic material, (2) surficial melting by lava flows, (3) basal melting of glaciers and snow packs through subglacial eruptions or geothermal activity, (4) ejection of water by eruption through a crater lake, and (5) deposition of tephra deposits on ice packs thereby decreasing their albedo and enhancing melting. On Mars, records of significant water enrichment and magmatism are often interrelated (Dohm 1998, 2009a,b), and the formation of lahars associated with the growth of volcanoes such as Apollinaris Patera are envisaged. Indeed, The Elysium region northwest of Apollinaris contains similar features that have been identified as lahars (Christiansen 1989, Russell and Head 2003). Our mapping efforts show two candidate lahar sites: the northeastern flank of Apollinaris Patera (Figure 4.13) and the fan deposits draping its southern flank. The first candidate site is discussed below, while the fan deposits are further explored in the next chapter.

The distinctive unit on the northeastern flank has been previously mapped and described as a volcanic unit of Apollinaris Patera (hereinafter referred to as unit Ha2 to match Scott et al. [1993] terminology) that underlies more extensive flank-forming materials, also described as a volcanic unit (unit Ha3). The Ha2 unit is affected by a 5-km-sized impact crater with highly deformed fluidized ejecta material. In addition, the unit is dissected by small channels in places (Figure 4.14) and appears smoother than the adjacent (stratigraphically younger) volcanic materials, comprising mostly subdued impact craters. At the bottom of the flank, many km-sized blocks appear to have slumped from the flank-forming materials, possibly being entrained during the formation of the putative lahar flow. Based on high-resolution images, the putative lahar deposits appear to overly deposits that are interpreted to be older MFF deposits (Figure 4.15), a stratigraphic relation which has already been reported with the lahar-like deposits referred to as simply "Apollinaris materials" (Kerber and Head 2010). This stratigraphic relation indicates that there was time separation between the emplacement of the older, flank-forming materials and the event which resulted in the distinctive materials, unit Ha2. Mass movement such as a lahar and associated morphologic expression could have been initiated through a number of processes such as the interaction of snow and volcanism or impact-generated tectonic instability and related geothermal activity associated with the formation of two relatively large craters (18 and 20 km in diameter) located 30 km to the east of the unit.

In order to test this hypothesis, crater counts were produced for different geological

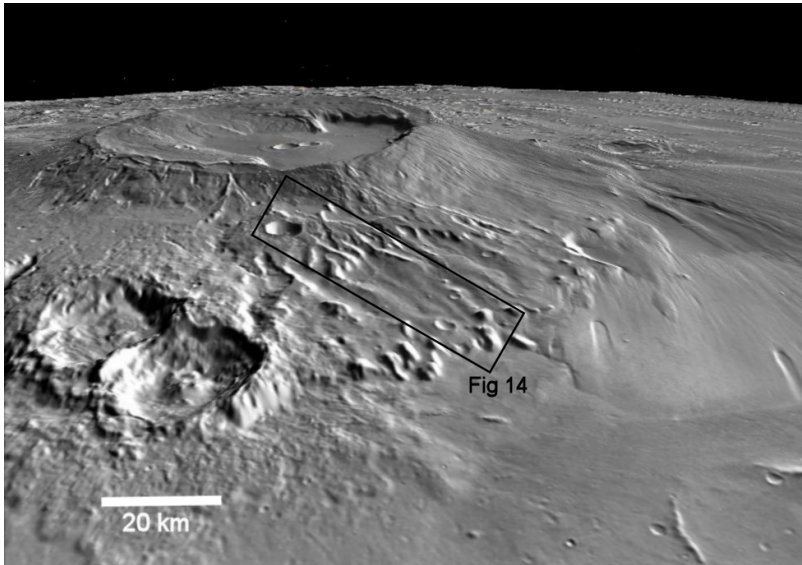


Figure 4.13: Digital terrain model (vertical exaggeration: 3x) of the putative lahar deposits previously interpreted as a volcanic unit. Notice the degradation of the old ejecta deposits of a 5 km-sized impact craters into dendritic landforms. Image credit: Google Mars.

Table 4.2: Crater count statistics for four different units in Apollinaris Patera which are highlighted in Fig. 11. D250 and D500 represent the cumulative total number of craters larger than 250m and 500m respectively. Images used for the crater counts are P06_003544_1703 (inner caldera), B01_010163_1712 (flank material), P18_007882_1703 (fan deposits), and P02_001645_1726 (putative lahar unit).

Unit	D500	D250	D250-500	Area(km ²)	D500 (per km ²)	D250 (per km ²)
Inner Caldera	19	98	79	364	0.052	0.26
Flank material	39	123	84	733	0.053	0.167
Fan deposits	130	476	346	2581	0.05	0.184
Putative Lahar	12	43	31	372	0.032	0.115

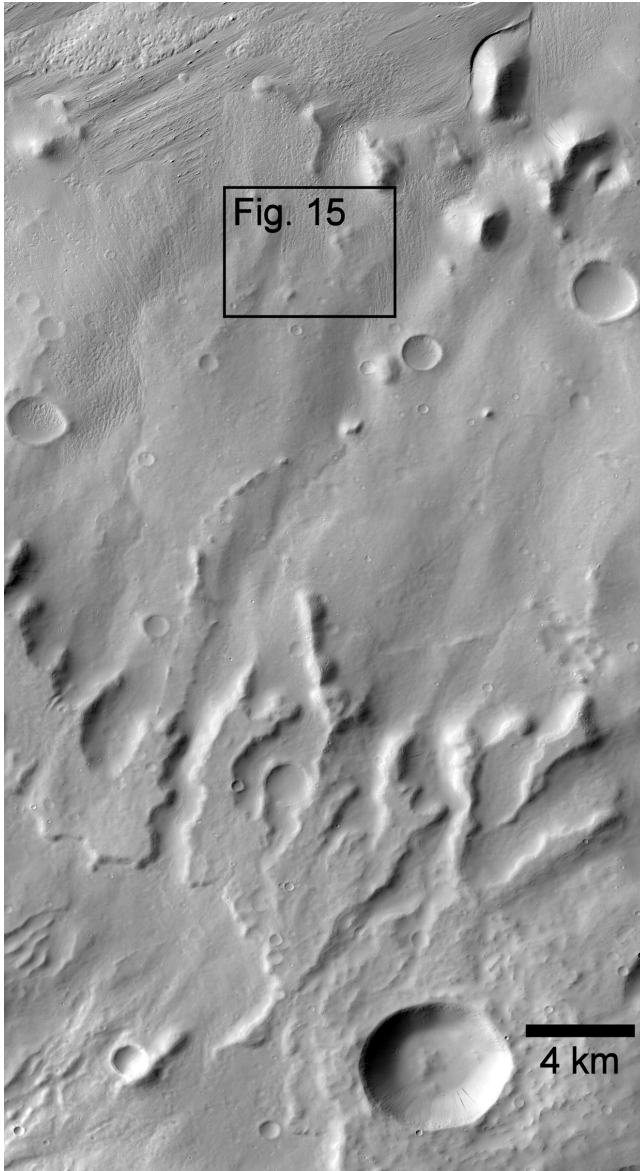


Figure 4.14: CTX image for the putative lahar deposits. The unit appears smoother than the surrounding terrain with most impact craters appearing degraded or subdued, and many channels dissecting the unit. Image ID: P02_001645_1726.

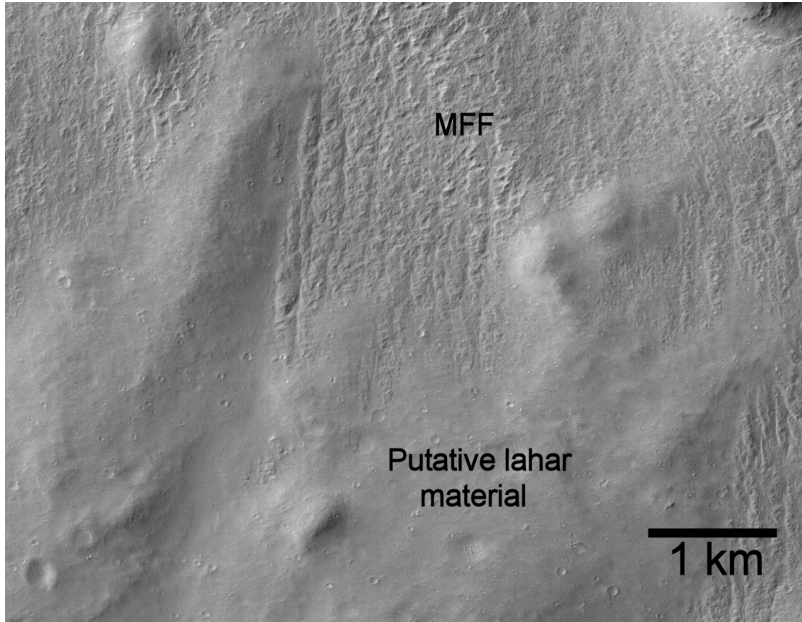


Figure 4.15: Close up of the relation between the putative lahar material and northern deposits interpreted as MFF deposits. The MFF deposits clearly underlie the putative lahar material. Image ID: P02_001645_1726.

units at Apollinaris Patera (from oldest to youngest): Ha2 (putative lahar unit), Ha3 (flank material), and Ha4 (inner caldera and fan deposits, also matching Scott et al.(1993) terminology, Figure 4.1). The crater count was carried out by measuring the cumulative density of craters larger than 500 m and 250 m for these units. We have ignored smaller crater counts in order to minimize the contribution of secondary craters to the overall population. Our results summarized in Table 4.2 validate the relative-age relation between the inner caldera and fan deposits. The Ha2 deposits however, give a clear relative younger age than all the other counted units as opposed to the conclusions of Scott et al. (1993). This further corroborates our hypothesis that the lahar flow has covered the older unit at a later stage masking a significant number of the older impact craters. Alternatively, the unit's deviation in crater statistics could indicate that the deposits are more friable than the rest of the volcanic units and thus readily degraded by processes such as wind erosion. While this hypothesis ignores the morphological evidence such as the dissecting channels, and apparent flow products and entrained material, it cannot be ruled out.

4.3.3 Magmatic-driven tectonism

The Apollinaris shield volcano is an isolated major vent structure¹. In addition, regional digital paleotectonic mapping investigation highlights primary and secondary centers of magmatic- and impact-induced driven tectonic activity in the eastern hemisphere, including Elysium, Hadriaca/Tyrrhena, Isidis-Syrtis, and Arabia Terra, but not in the Apollinaris and surrounding region (Anderson et al. 2007). Viking-based geologic investigations point to the Elysium volcanic province as a region of possible magma-water interactions (e.g., Greeley and Guest, Mouginitis-Mark). Such activity, which would result in hydrothermal activity, is being corroborated and greater detailed through post-Viking data (Tanaka et al. 2005). Hadriaca/Tyrrhena (Crown et al. 1992.) and Isidis-Syrtis (Mustard et al. 2006, 2008), which are volcanic provinces associated with the large impact basins, Hellas and Isidis, respectively, also show evidence of magma-water interactions, and thus are also considered prime targets of hydrothermal activity along with the Elysium volcanic province (Schulze-Makuch et al. 2007). The Arabia Terra region, which is hypothesized to have been influenced by a long-lived basin/aquifer system (Dohm et al. 2007), comprises evidence of magmatic-tectonic activity, which includes structurally-controlled, terrestrial spring-like mounds such as within the Vernal impact basin (Allen and Oehler 2008).

In the case of Apollinaris Patera, in addition to an identified northwest-trending prominent structural zone of crustal/lithospheric weakness near the northeastern flank of the shield volcano (Dohm et al. 2007), there are dominantly northwest- and northeast-trending structures, several of which occur among some of the mounds, possibly indicating basement structural control (Figure 4.10). As on Earth, tectonic structures can control the migration of fluids such as magma, water, and other volatiles, as well as heat energy, in the subsurface, influencing hydrogeologic and volcanic activity such as observed within the Thaumasia region (Dohm et al. 1998, 2001, Tanaka et al. 1998) and for Earth such as in the San Francisco and Mormon volcanic fields of northern Arizona near the Grand Canyon (Dohm 1995, Holm 2001), the Chilean Atacama Desert (Warren-Rhodes 2007, Hock et al. 2007), and Solfatara Crater, Italy (Chioni et al. 1984).

4.3.4 Craters with fluidized ejecta

Martian craters are known to display layered ejecta deposits (Barlow et al. 2000) that appear fluidized. These observations were made as early as the Mariner 9 and Viking eras (e.g., McCauley 1973, Carr et al. 1977, Allen 1979, Mouginitis-Mark 1979, 1987). Depending on morphology, these ejecta were historically given different names such as pedestal, rampart, lobate, and pancake. However, the current general consensus is to use the term "Layered Ejecta Deposits" (LED) for craters with rampart, lobate, and pancake shaped ejecta, while the term 'pedestal' is conserved for layered ejecta patterns that have undergone substantial erosion, resulting in the crater and ejecta being perched above the surrounding terrain (Barlow et al. 2000). While eolian activity has been suggested to be responsible for the modification of these ejecta deposits (McCauley 1973, Arvidson

¹The work in this section (magmatic-driven tectonism) was jointly carried out by a co-author (James Dohm) on the paper submitted to Icarus presenting the results in this chapter, and while this section is inserted here for clarity and completeness, the author cannot take sole credit for it

1976), it is generally accepted that LED craters are evidence of impacts into ice- or liquid water-enriched target materials (e.g., Carr et al 1977, Mouginis-Mark 1979, Barlow 2001, 2004, Oberbeck 2009).

We have mapped LED impact craters using the CTX data (resolution $\approx 6\text{m}$ /pixel), as it provides sufficient resolution with the greatest spatial coverage. The image resolution facilitated the detection of impact craters with LED morphology down to $\approx 20\text{ m}$ in diameter (Figure 4.16), while the spatial coverage of the CTX images allowed for the mapping of the entire volcanic edifice and some of its surroundings (see Figure 4.1). The distribution of impact craters with LED morphology (Figure 4.10) shows their prevalence in the region, with a significant amount of these craters being pedestals, while the rest being single layered ramparts with few exceptions showing multilayered ejecta (Barlow et al. 2000). The nature of the ejecta deposits of small (< 50 meters) impact craters, however, is difficult to determine.

The resulting map (Figure 4.10) points to volatile enrichment in and surrounding the shield volcano for at least part of its history, including the caldera complex, the shield-forming materials, and the surrounding materials including the MFF. In fact, two medium-sized impact craters are located in the central part of the caldera, which have diameters and depths, of 4.8 and 6 km and 100m and 400 m, respectively. This hints at volatile enrichment of the caldera floor materials at the time of impact crater formation that most likely post-dates Apollinaris Patera's complex volcanic activity.

4.3.5 Mineralogy: context and regional

Magmatic-driven hydrothermal systems are expected to form a rich suite of minerals. As a result, an effort was made to locate mineral signatures that could be indicative of hydrothermal alteration such as clay minerals, zeolites, serpentines, sulfates, carbonates, and silica-rich deposits. CRISM is a hyperspectral imager that measures reflected radiation in the visible and near infrared (VNIR) from the surface of Mars, providing the ability to recognize both primary (e.g., olivines and pyroxenes) and secondary minerals (e.g., clay minerals). The spatial resolution of the instrument in its full-resolution configuration is $\approx 15\text{-}19\text{ m}$ /pixel with 544 spectral channels and with a footprint $\approx 14\text{ km}$ across.

Nine CRISM observations at different spatial resolution are currently available for the region, sampling part of the caldera and the western flank of the volcanic edifice. These observations were converted to apparent I/F (the ratio of reflected to incident sunlight), then divided by the cosine of the incidence angle to correct for the illumination geometry (Murchie et al. 2007, 2009). The atmospheric contribution was removed using an improved volcano-scan correction proposed by McGuire et al. (2009). A de-spiking and de-stripping algorithm (Parente, 2008) was applied to improve the overall quality of the observation by removing artifacts. Evaluation of the CRISM data used the spectral parameters of Pelkey et al. (2007). We investigated a variety of the parameters, including those associated with hydrated and/or hydroxylated silicates, sulfates, and carbonates. Each parameter map was visually evaluated using one, or more, threshold value(s) in search for a spatially coherent pattern that potentially suggests positive identification. However, no spatially coherent patterns were found in the eight observations considered.

A visual inspection has been carried out for each observation revealing the absence of obvious absorption bands that might have helped to assess the mineralogy of Apollinaris

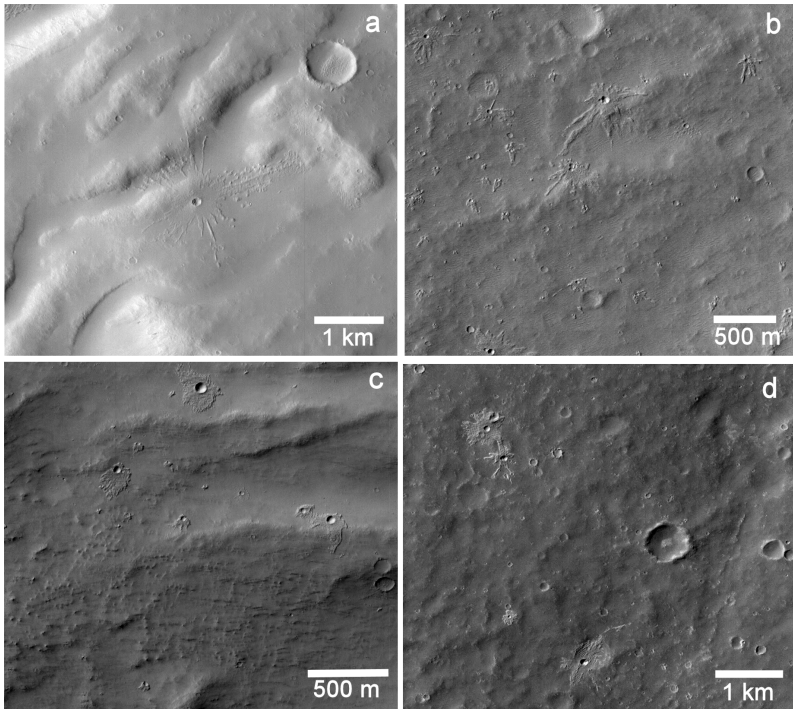


Figure 4.16: Examples of small (20-200m-wide diameters) single layered ejecta (SLE) craters at Apollinaris Patera. Most craters are either rampart or pedestal. The distribution of these craters is uniform throughout the volcano as they are located on the main edifice (a, b and c), the fan deposits (d), and even in the caldera complex (e and f).

Patera. The spectra appear featureless across the entire structure, from the caldera to the base of the flank sampled by the CRISM observations (a typical spectrum is shown in Figure 4.17). The slight positive slope in the spectral range 1.0-2.5 μm could be suggestive of iron oxides (e.g., hematite $\alpha\text{-Fe}_2\text{O}_3$) and the reduced spectral contrast is consistent with the presence of fine particles (e.g., Hapke 1981, Mustard and Hays 1997) that cover the surface, probably masking the underlying composition. Iron oxides can be a marker of water-related alteration of the rock materials.

Another spectroscopic data source is the lower-resolution Mars Odyssey Gamma Ray Spectrometer (GRS), which marks elevated hydrogen and chlorine (Figure ??) when compared to the rest of the equatorial region of Mars (Boynton et al. 2004, Keller et al. 2006, Taylor et al. 2006, Dohm et al. 2008). The elevated abundances could indicate possible long-term, magma-water interaction, among other possibilities, including

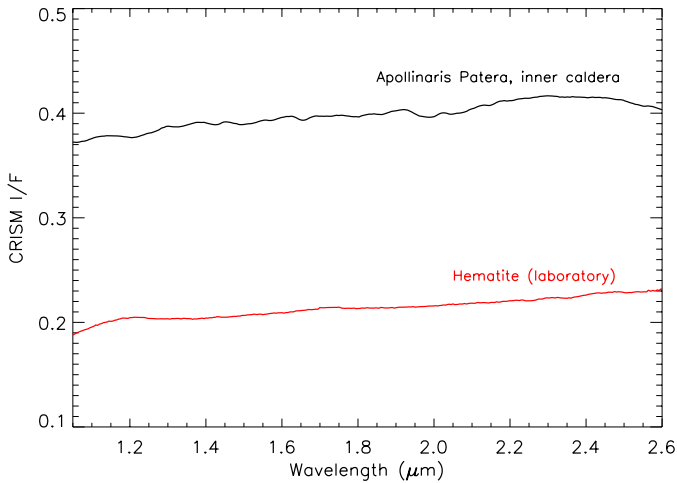
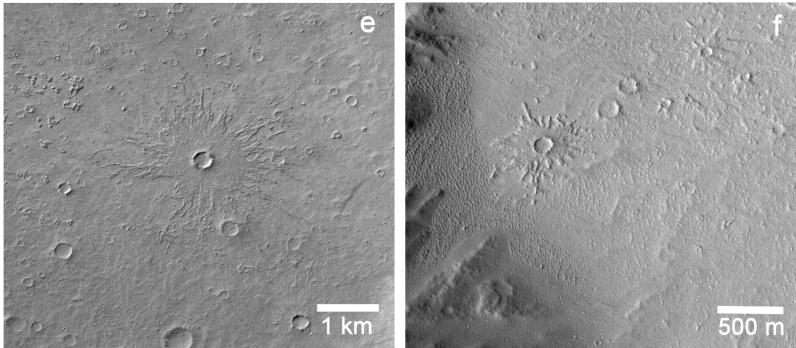


Figure 4.17: A CRISM spectra from Apollinaris inner caldera (black). As discussed in the text, the spectra are fairly featureless with a slight positive slope that could be indicative of iron oxides. As a comparison, a lab spectrum of hematite at the same spectral range (red) is shown. CRISM image ID: HRL0000C68B, Hematite lab spectrum: CRISM spectral library, Sample ID: CAGR04 (Credit: Giuseppe Marzo).

the reaction of the fine-grained volcanic materials of Medusae Fossae materials, such as ignimbrite material (Malin 1979), with acid-fog emissions from either the Tharsis volcanoes or from other local source vents that have since been buried or destroyed (Keller et al. 2006, Dohm et al. 2008).

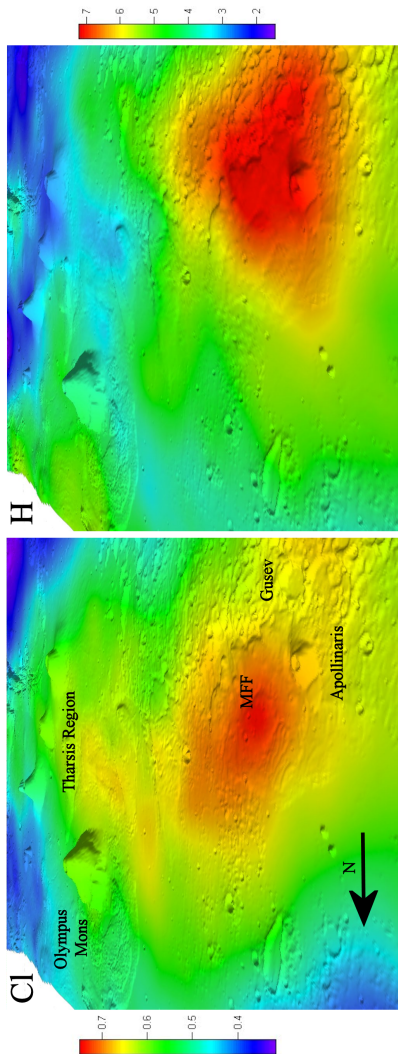


Figure 4.18: Chlorine GRS elemental map (left) and water-equivalent hydrogen (right) draped over a 3D construction of the northern plains including Apollinaris, the MFF deposits and the Tharsis Plateau. Elemental concentrations are in wt%. The elevated abundances could indicate possible long-term, magma-water interaction, among other possibilities (Credit: Trent Hare, USGS).

4.3.6 Similarity to terrestrial analogs

Since liquid water coupled to some form of endogenic heat is often considered to be a requirement for the evolution of primitive life (e.g., Dohm et al. 2004, Fairén et al. 2005, Furfaro et al. 2008), environments where there is a spatial and temporal association among magmatism, tectonism, and aqueous activity are considered prime environments of elevated potential for life (Dohm et al. 2004, Warren-Rhodes 2007, Hock et al. 2007, Schulze-Makuch et al. 2007, Furfaro et al. 2008). This is exemplified in the Atacama Desert of Earth and the Tharsis/Elysium corridor region of Mars, which includes the Apollinaris Patera and surrounding terrains (Dohm et al. 2008). In the Atacama Desert, examples include: (1) fractures and faults which form conduits for the migration of subsurface and surface flow of magma and water and other volatiles (e.g., groundwater sources from the Andes, migrating across the Atacama Desert in the subsurface along basement structures, transecting the Coastal Range, and eventually debouching into the Pacific Ocean), (2) erosion- and collapse-related structures along basement structures associated with the withdrawal of fluids or the dissolution of materials such as salt (e.g., prevalent in evaporite deposits such as salts of the Atacama Desert), and vent structures and often associated tectonic structures, which includes faults and fractures and collapse structures (e.g., see Chong Diaz et al. 1999). Both examples are plausible activities of the Apollinaris Patera and surrounding region.

The 4000 yrs old Solfatara Crater from Italy has been proposed as a terrestrial analog of hydrothermal activity for the Tharsis/Elysium corridor of Mars (Dohm et al. 2008). The volcanic activity of the Solfatara Crater comprises explosive and effusive eruptions (e.g., Chioni et al. 1984), similar to the activity proposed for the Tharsis/Elysium corridor. Solfatara is a flat-bottomed caldera with steep, 80-85 m-high walls, located in southern Italy. It is part of the Campi Flegrei volcanic district, represented by a nested 12-km-wide structure of calderas and small volcanic edifices. Campi Flegrei has been active during the Quaternary (at least since 47,000 years ago) and is linked to the extensional tectonics of the Tyrrhenian margin. This district is connected with the Somma-Vesuvio volcanic complex to the southwest.

Today, Solfatara exhibits ongoing fumarolic activity and emissions of sputtering mud in a few mud pools. The hydrothermal system is vapor dominated and fed by a 1.5 km deep geothermal aquifer of mixed magmatic-meteoritic origin (Chioni et al., 1984). Fluid temperatures range from 40-50°C to ≈160°C with a pH of approximately 1.7. Hydrogen sulfide and CO₂ are the dominant components of the hydrothermal fluids, whereas HCl, CH₄, and H₂ occur as minor constituents (Valentino et al. 1999). Such chemistry produces predominantly anoxic and reducing environmental conditions with oxic/anoxic transition zones found at the surface. Mineral assemblages of the deposits include sulfur, sulfates (gypsum, barite), hydrous sulfates (alunite), and pyrite minerals. Chemical processes of aqueous hydrothermal weathering, which dominate Solfatara's environment, have been recently suggested as a viable option for Martian surface alteration processes (Dohm et al. 2009b,c, McCubbin et al. 2008, 2009, Mangold et al. 2010).

4.4 Discussion

Evidence highlighted above of water enrichment and activity, magmatism, and tectonism at and surrounding the prominent volcano, Apollinaris Patera, often interrelated, collectively point to a long-term hydrothermal environment. Yet further evidence discussed below are a possible volcanic crater paleolake in the caldera complex and Apollinaris-forming materials that interfinger stratigraphically with MFF materials, which includes the volcano possibly sourcing the latter, as well as the exobiological significance of the Apollinaris Patera-influenced environment.

4.4.1 Possibilities for the past presence of a volcanic crater lake

There are multiple indicators that hint at the possible past presence of a volcanic lake at the summit of Apollinaris: (1) the evidence of near surface enrichment in volatiles as indicated by the impact craters with fluidized ejecta inside the inner caldera complex, (2) the evidence for major lahar events that appear to initiate from the summit, and (3) similarity to hydrothermal/magmatic systems on Earth with an associated volcanic lake.

Volcanic lakes are a common feature in many hydrothermal/magmatic systems on Earth ranging in composition from very dilute meteoric waters to highly acidic (<0.5 pH) brines. They can either have a purely meteoric origin or a hydrothermal/magmatic one, but mostly, they are a combination of both, forming through interaction of magmatic fluids with ground water (Varekamp et al. 2000). There are numerous examples for hydrothermal/magmatic-induced lakes such as the ones at Mt. Ruapehu, New Zealand (Christenson 2000), Kawah Ijen, Indonesia (Delmelle et al. 2000), Poás volcano, Costa Rica (Rowe et al. 1992), Copahue volcano, Argentina (Varekamp et al. 2004), and the Waimangu system, New Zealand (Scott 1995).

The Copahue volcano in particular, has been sited as a possible modern terrestrial analog for the MER Opportunity landing site (Varekamp 2004) since the region contains an acid lake and hot springs that deposit jarosite, gypsum and hematite; a suite of minerals detected by Opportunity at Terra Merdiani (Christensen et al. 2001, Hynek et al. 2002, Squyres et al. 2004a, 2004b, Klingelhofer et al. 2004). In addition, the Copahue environment can exist without a meteoric water cycle, since the hot spring fluids are 50-70% magmatic waters that are quenched by meltwater supplied from the summit glacier of Copahue (Varekamp 2004). Such an environment is highly plausible for Apollinaris in presumed periods of activity.

The suite of evidence discussed in the previous sections points to a long history of magma/water interaction making it likely that such a lake may have formed at the summit of Apollinaris. An Apollinaris lake would have persisted for a significant amount of time even under conditions similar to Mars today. The same arguments that have been put forward to show the longevity of impact-driven hydrothermal lakes (Newsom et al. 1996, Abramov and Kring 2005) hold for magmatic-driven ones that are expected to exhibit even longer lifetimes than impact-generated ones. On Earth, Volcanic lakes can reach temperatures of 70-80°C as a result of the heat influx from the magmatic parent body, fluid circulation, and fumarolic activity. On Mars, ambient temperatures are generally lower than Earth. Nevertheless, it is expected that magmatic activity would be capable of keeping the lake temperature above the freezing point for most of its life-time. Any

extensive magmatic episodes occurring in the vicinity of the lake would have breached the caldera rim triggering an overflow and possibly a lahar event similar to what happened at Mt. Ruapehu in 2007 (Kilgour et al. 2010).

Ghail and Hutchison (2003) were the first to suggest the past presence of a volcanic lake at Apollinaris based on their interpretation of the fan deposits as alluvial in origin. Their interpretation was based on their opinion that the high resolution data that were available at that time (partial set of the MOC data) did not reveal any of the features that could be associated with volcanic flows as was originally suggested by Robinson et al. (1993) to happen. It is clear that differentiating between the various proposed formation mechanisms for the fan deposits (volcanic flow, alluvial fan, ignimbrites) is not possible using geomorphology alone, but low-frequency radar sounding may constrain these possibilities. Preliminary analysis of Shallow Radar (SHARAD, Seu et al. 2007) data suggests the presence of layering in the fan deposits, which suggests that the mechanism of formation continued for some time and was multi-staged (see next chapter).

While direct geomorphological evidence for a lake in the caldera maybe lacking, we believe that the combined indirect and circumstantial ones are strong. It will be possible to search for mineralogical evidence in the caldera in the future with high resolution data from CRISM. Currently, the coverage of the caldera by CRISM data is poor (Figure 4.1). A positive identification of index minerals such as gypsum, jarosite, alunite, amorphous silica, hydrous Fe-oxides or carbonates would offer strong evidence for the past presence of a magmatic-driven volcanic lake or other surface expressions of a deeply rooted hydrothermal system.

4.4.2 Interfingering Apollinaris Patera and MFF materials

The Medusae Fossae Formation is an enigmatic deposit located along the highland-lowland boundary of Mars near the equator, stretching between 170 and 240 °E to the west and south of the Tharsis and Elysium volcanic provinces, respectively, and bordering the northern and eastern flanks of Apollinaris Patera. It has been mapped as one of the youngest deposits on Mars, relative-age dated as Amazonian (Scott and Tanaka, 1986). However, recent works point to an earlier age of formation for some of the materials, dating as far back as the Early Hesperian epoch (Kerber and Head, 2010). The geologic formation is divided into seven separate units (Scott and Tanaka, 1982). Kerber and Head (2010) investigated the contact between the MFF unit north of Apollinaris and the main edifice and concluded that a part of the Apollinaris volcanic material (interpreted as putative lahar deposits in the current study) is overlying MFF deposits citing this as partial evidence for a more ancient emplacement age. We have similarly investigated the relation between the northern flank of the edifice and the MFF materials (Figure 4.19). The MFF can be divided into at least three separate units that show distinct vertical separation and differences in morphology (Figures 4.19 and 4.20). All units comprise mounds and degraded craters. Unit MFF3 (Figures 4.19 and 4.20) displays yardangs, which are characteristic of MFF deposits, and overlies unit MFF2, which in turn overlies unit MFF1. Units MFF2 and MFF3, in particular, show extensive degradation with almost complete removal at some locations (Figures 4.20 and 4.21). In addition to the previously discussed relation between the MMF2 and the putative lahar material shown in Figure 4.15, there is another region at the northwest (unit Ha3) where it appears that a late activ-

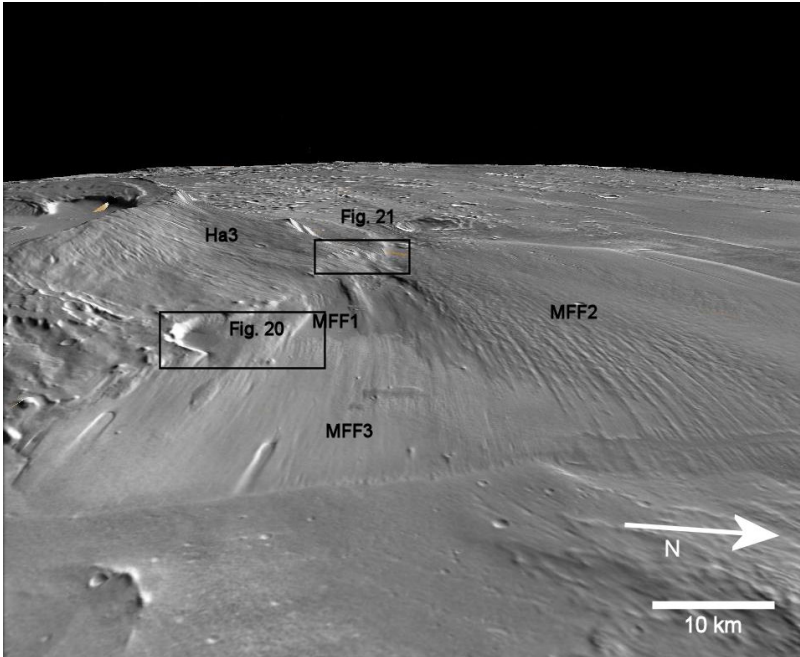


Figure 4.19: Digital terrain model (vertical exaggeration: 3x) of the northern MFF deposits. Three different units can be discerned on account of differences in morphology, texture, and stratigraphy with unit MFF3 being the youngest unit and MFF1 the oldest.

ity has draped the older edifice scarp and now overlies parts of the MFF2 unit (Figures 4.19 and 4.21). The results of our efforts are mostly consistent with Kerber and Head (2010) indicating that: (1) MFF deposits began to be emplaced much earlier than previously recognized from Viking-based geologic investigation (e.g., Scott and Tanaka, 1982, 1986), (2) MFF included multiple stages of development (i.e., at least three MFF units north of Apollinaris based on this investigation), (3) the MFF deposits are friable and thus impact craters readily destroyed, altering the crater retention ages (i.e., exhibiting an apparent younger relative age), (4) Apollinaris Patera-forming materials intermingle stratigraphically with the MFF deposits, and (5) the spatial and temporal relations among the Apollinaris materials and the MFF deposits point to Apollinaris as a candidate source for at least some of the MFF deposits. Similar to the MFF deposits with various stages of emplacement spanning the Early Hesperian through to the Late Amazonian, the fact that Apollinaris has produced materials that are younger than some of these deposits also hints at its long term activity.

In conclusion, our efforts support Kerber and Head (2010) conclusions of the probable older age (start of deposition) of the MFF and its formation through multiple stages by

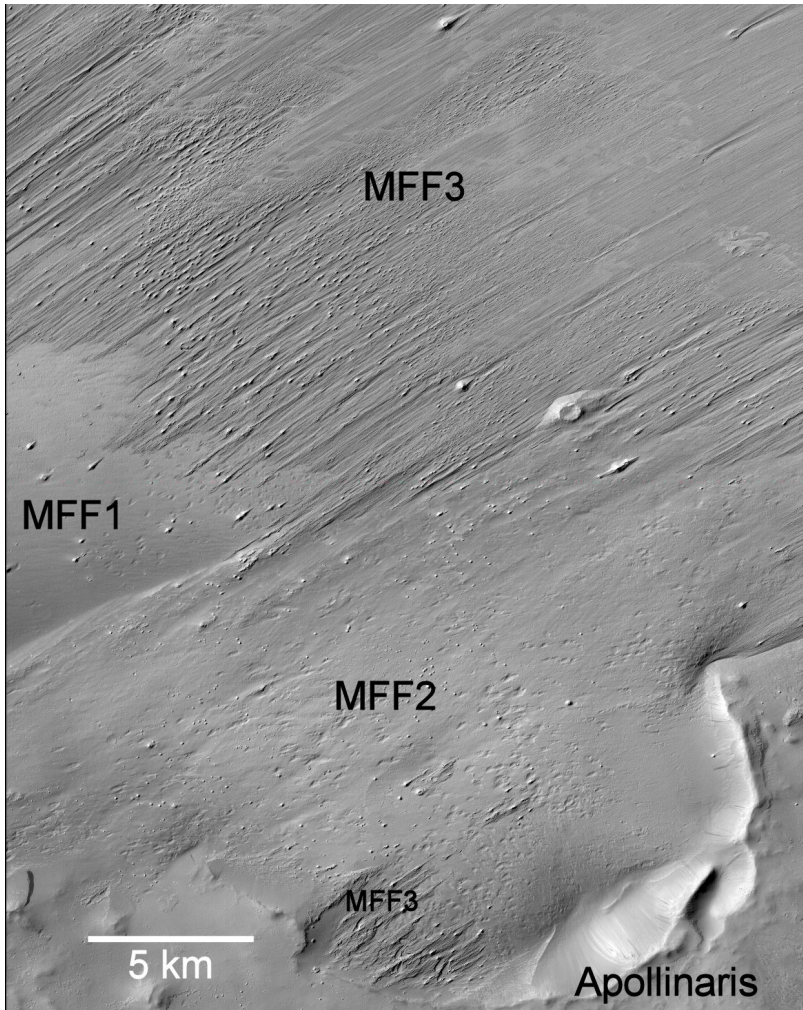


Figure 4.20: CTX cover of one of the contacts between Apollinaris and the MFF deposits. The three units can be seen along with their stratigraphical relations. MFF3 unit shows features interpreted as yardangs as is common for MFF. Mounds appear scattered throughout all the units. Image ID: P16_007236_1754.

identifying at least three MFF units north of Apollinaris in addition to the stratigraphic relations between various Apollinaris activities and the MFF deposits. The age of the MFF has been determined mainly through crater counting techniques and stratigraphic

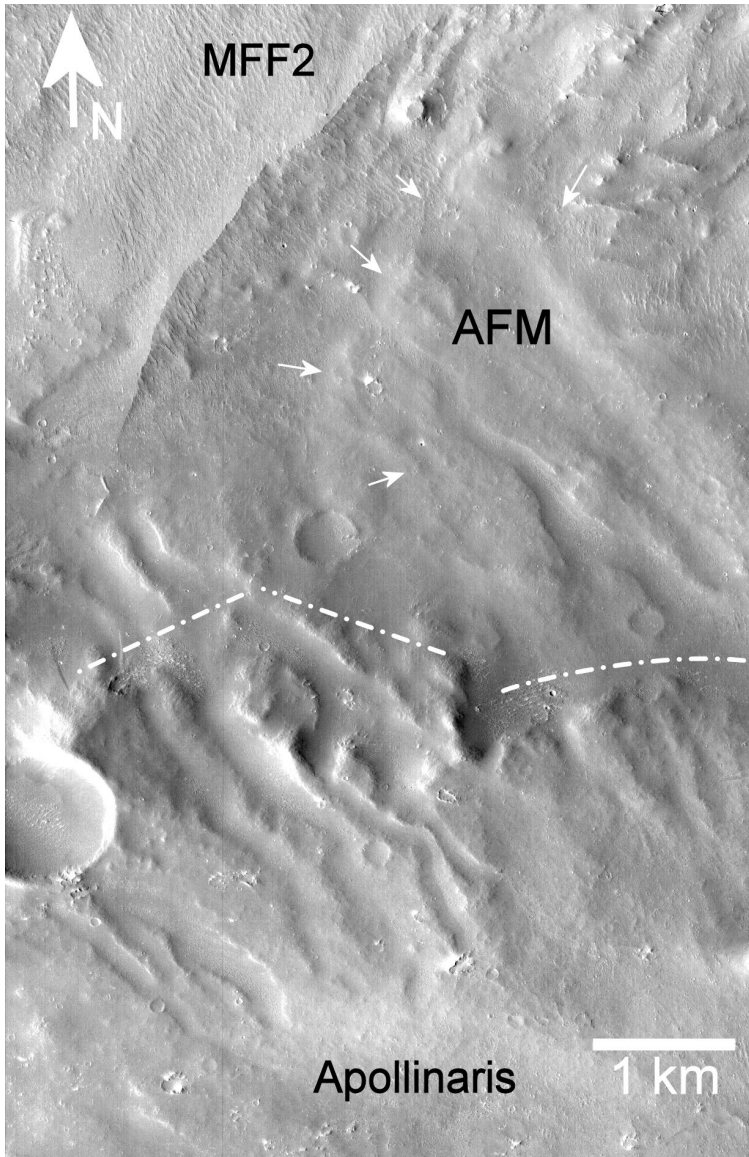


Figure 4.21: CTX cover of another contact between MMF and the main edifice. Young Apollinaris flow materials (AFM) appear to have draped and extended beyond the edifice's scarp and are now overlying the MFF deposits interpreted in this study as MFF2 unit. Image ID: B12_014132_1721.

relationships (Scott and Tanaka 1982). However, our mapping efforts show that the MFF deposits can be extremely friable, and thus easily degraded. This in turn could lead to faster degradation of impact features giving an "apparent" younger age for the deposits than they really are. Nonetheless, there is evidence that the MFF deposits were formed in various stages spanning the early Hesperian to middle and upper Amazonian, and the fact that Apollinaris has produced deposits that are younger than some of these units hints at a similarly long term activity at Apollinaris.

4.4.3 Implication for exobiology

The diverse evidence of past and present-day water/ice at the Martian surface, coupled with the dynamic geologic history as noted above, indicates that hydrothermal environments existed in the past and some may still be active today (Dohm et al. 1998, 2008, Mustard et al. 2006, Schulze-Makuch et al. 2007). These environments are considered prime targets for testing the hypothesis of whether life existed (or still exists) on Mars (Dohm et al. 2004). Assessing the past existence of hydrothermal systems on Mars has important exobiological implications because hydrothermal systems may have provided habitats for the origin and evolution of early life (Shock 1996, Farmer 2000, Schrenk et al. 2010). On Earth, life thrives in hydrothermal environments with low pH and temperatures close to the boiling point of water. Prokaryotes, which have dominated life on Earth for most of Earth's history, have adapted to environmental extremes of temperature, pH, pressure, salinity, and anoxic conditions (e.g., Nealson 1999, Schulze-Makuch and Irwin 2004).

It is possible that hydrothermal environments on Mars may also record biologic activity assuming that life began there. On Mars, such environments may have been extremely long-lived as in, for example, the case of Apollinaris Patera that was potentially active from the Late Noachian through the Late Hesperian epoch with a possible evolutionary phase extending over roughly 200 million years, according to the estimated absolute age based on impact crater statistics (Hartmann and Neukum 2001). As a result, we propose that the mound structures around Apollinaris should be prime targets for future landed missions to search for exobiological signatures in the area since they meet the scientific requirements of being strong candidates for evidence of long-term magma/water interaction.

4.5 Conclusion

Our most recent analysis using a group of recent remote sensing data supports the Viking-era geologic investigations and suggests Apollinaris Patera to be a prime site of magmatic/hydrothermal activity with significant life-habitability potential. This includes:

- (1) A valley system which dissects Medusae Fossae materials to the east of the volcano is now traced more accurately corroborating the previous assumptions about its nature as evidence of liquid water activity on the surface.
- (2) Ubiquitous presence of impact craters in both shield-forming (flank and caldera) materials and materials that surround the volcano that are indicative of water-rich

target materials at the time of impact such as impact layered ejecta deposits.

- (3) Some chaotic-terrain-composing mesas which display terraces along their margins and flows near their summits, possibly marking aqueous activity.
- (4) Numerous faults, fractures, and scarps possibly related to tectonism, which were not observed during Viking-era geologic mapping investigations.
- (5) Mounds of diverse geometric shapes, many of which display summit depressions and occur among faults and fractures, possibly marking venting.
- (6) Evidence on the flanks of the volcano for lahar events and a putative volcanic lake.
- (7) A possible association in time and space among shield-forming materials and Medusae Fossae materials.

These results also point to Apollinaris being a site of exobiological significance, and as such, we have proposed some candidate sites for future exploration. Finally, these results, obtained by employing a multidisciplinary approach, highlight the importance of using such an approach when dealing with planetary remote sensing where the geomorphological principle of equifinality plays a key role in the presence of multiple hypotheses, each with their own implications for our understanding of the geological evolution.

5 Geophysical Investigations by Ground-Penetrating Radar (GPR)

5.1 Introduction

As has been discussed and shown in previous chapters, IR radiation is capable of penetrating only the first 100 microns of the surface while GRS can go further to almost 1 meter deep. Electromagnetic remote sensing typically probes to greater depths in a target medium as the illuminating wavelength increases (frequency decreases). To penetrate typical near-surface crustal materials and characterize layers at significant depth, the active signal must have a wavelength of several meters or more (as opposed to IR radiation, for example, with wavelengths in the micrometer to centimeter range). Radio echo (radar) sounding is a technique that has been used before on Earth to study the subsurface characteristics of the ice sheets which can be many kilometers in thickness (e.g., Holt et al. 2006). Radar waves are sensitive to the variations in electrical properties of rocks and to the presence of water (either liquid or solid), whether on the surface or in the subsurface. For these reasons, radar sounders are considered to be one of the most promising geophysical techniques to investigate the distribution of subsurface water and constrain subsurface morphology and composition.

Currently, there are two low frequency radar sounders orbiting Mars: The Mars Express Mars Advanced Radar for Subsurface and Ionospheric Sounding (MARSIS, Picardi et al. 2005), and the MRO Shallow Radar (SHARAD, Seu et al. 2007). More technical information about these two instruments can be found in the appendix section (A.6). Both instruments operate under the principles of a synthetic aperture radar (SAR) where a target scene is repeatedly illuminated with pulses of radio waves at wavelengths anywhere from a meter down to millimeters. The many echo waveforms received successively at the different antenna positions are coherently detected and stored and then post-processed together to resolve elements in an image of the target region. MARSIS and SHARAD differ in their penetration depths. While MARSIS (in its subsurface mode) can reach depths of 2-10 km through its lower operational frequency, SHARAD's higher frequency has a less sampling depth of around 1 km but achieves a better vertical resolution, thereby allowing it to detect finer layering that cannot be seen by MARSIS. Both instruments have been used to detect layering in the polar ice deposits and infer their total thickness (Picardi et al. 2005, Plaut et al. 2007), study sedimentary features such as the Medusae Fossae Formation (Waters et al. 2007, Carter et al. 2009), the Vastitas Borealis Formation (Campbell et al. 2008), and debris aprons in the mid-latitudes (Plaut et al. 2009) in addition to testing fluvial versus volcanic origin hypotheses for certain areas such as

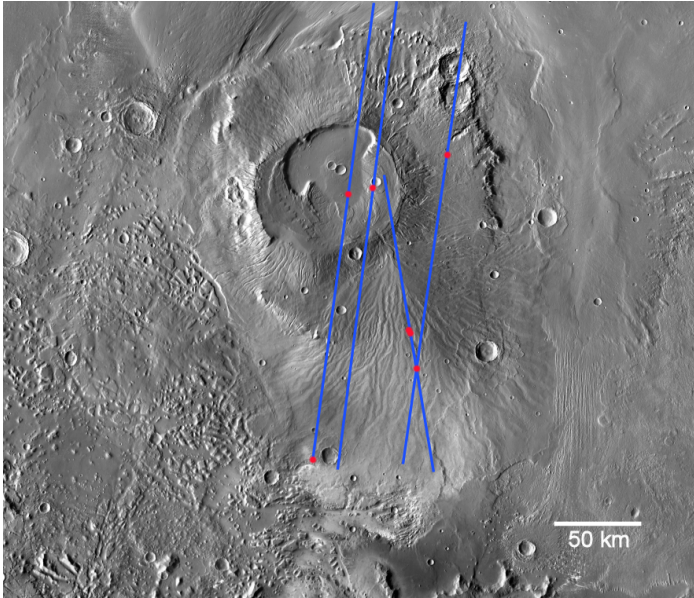


Figure 5.1: Groundtracks of the SHARAD cover over Apollinaris.

Athabasca Valles (Boisson et al. 2009). Radar sounding can be extremely useful in detecting subsurface manifestations of hydrothermal systems in a manner that other remote sensing techniques cannot achieve through the last application in particular (differentiating between fluvial and volcanic origins). As a case study, the rest of the chapter will deal with currently ongoing efforts to constrain the composition of the Apollinaris fan deposits discussed earlier in addition to looking for signs of a volcanic paleolake in the caldera complex by searching for a sedimentary signature inside the caldera (for details refer to chapter 4). It has to be noted that this work is currently in progress, and is being carried out as a collaborative work. However, the author would like to demonstrate here his personal efforts and insights on how such a technique may be viable for the search for shallow subsurface manifestations of hydrothermal systems.

5.2 Methods and dataset

Figure 5.1 shows the radar ground tracks in the Apollinaris region. These ground tracks are usually displayed in the form of radargrams (Figure 5.2) showing the radar backscattered echoes that are plotted in delay time versus latitude along the ground track. Usually a topographic profile as attached to the radargram to aid in the interpretation of the data. The derived information can be used to estimate the real part of the complex dielectric constant ϵ' (or permittivity) of the target medium using the equation:

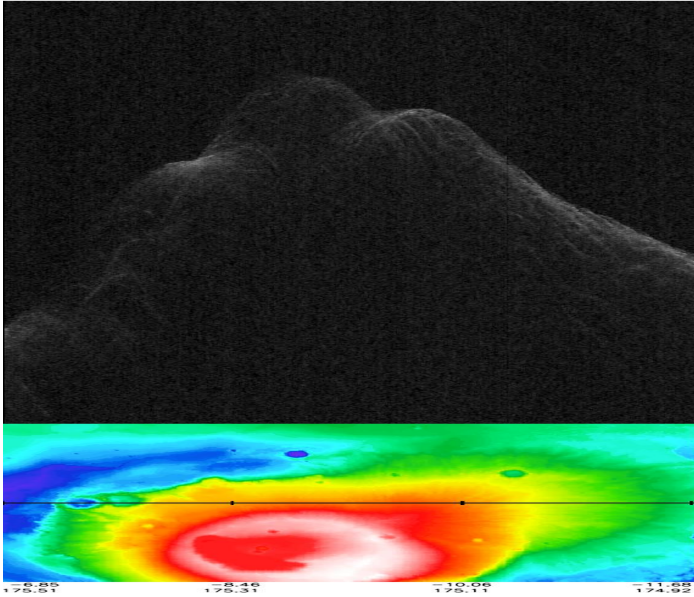


Figure 5.2: An example of a typical SHARAD radargram. The radar backscattered echoes are plotted in delay time versus latitude along the ground track. A topographic profile as attached to the radargram to aid in the interpretation of the data. The black horizontal line in the topographic profile shows the ground track of the radargram.

$$\varepsilon^r = \left(\frac{c\Delta t}{2h}\right)^2 \quad (5.1)$$

where h is the height relative to the surrounding plains as measured from MOLA topography and Δt is the two-way time delay between the surface and subsurface echoes measured from the radargram (see Carter et al. 2009). The real part of the dielectric constant can differentiate between volcanic flows with values ranging from 6 to 9, and sedimentary or ice-rich materials with values from 3 to 5 (Boisson et al. 2009, E. Heggy, personal communication). So in theory, by analyzing the radar signals from the fan deposits and the caldera flow we should be able to infer whether the material is consistent with a lava flow properties or with a sedimentary or ice-rich material. However, radar detection of the Martian subsurface is not trivial and remains poorly constrained. The ice dielectric signature inferred from the dielectric constant's real part cannot be distinguished from the one of low-loss silicate materials such as volcanic ashes, or loose, dry sediments (Boisson et al. 2010, Radar Sounding of temperate permafrost in Alaska: Analogy to the Martian Mid- to High-latitude Ice-rich Terrains, submitted manuscript). Therefore, analysis of Martian radar sounding data needs to take into account the imaginary part of the dielectric constant in order to make a unique interpretation (Heggy, personal communi-

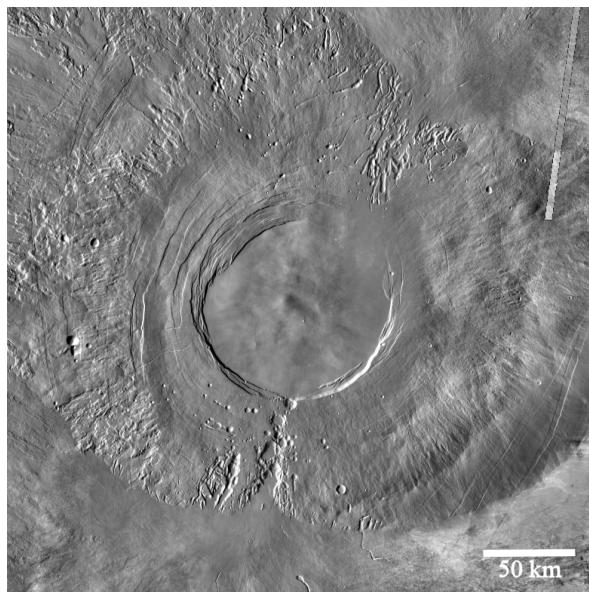


Figure 5.3: THEMIS IR mosaic for Arsia Mons in the Tharsis region. Arsia Mons is characterized by a relatively plain and young caldera making it ideal for a volcanic calibration.

tion). Moreover, Martian radar data analysis is subjected to uncertainties due to scattering losses, and while surface roughness can be relatively easily accounted for through the use of MOLA derived topography and roughness measurements (e.g. Neumann et al. 2003) to make a clutter model¹, subsurface scattering phenomena (which depend on the heterogeneity degree of the sounding subsurface) are more difficult to account for.

In view of these difficulties, we have devised a "calibration" technique to compare between the relative signal losses of the Apollinaris region and a site of known volcanic composition. For this calibration, we used Arsia Mons (9.2°S, 239.6°E, Figure 1.2 and Figure 5.3) which is a major volcanic edifice in the Tharsis region of Mars standing over 10 km above the surrounding terrain and having a relatively plain caldera that is almost 100 km wide. We chose Arsia Mons because of its caldera that has similar dimensions to those of Apollinaris (around 80 km) in addition to the relatively young age of Arsia Mons caldera (derived from crater counts) that suggests continuous volcanic activity from Late Noachian/Early Hesperian to a period as recent as 100 to 40 million years ago (Hartmann et al. 1999, Mougini-Mark and Rowland, 2008). The aim is to compare the signal losses in both calderas to infer if Apollinaris caldera is infilled with volcanic materials or sedimentary deposits that could be indicative of a paleolake or other surface manifestation of a long-lived magmatic/hydrothermal system. In total, there are currently 19 radar observations covering the Apollinaris region (12 MARSIS, 7 SHARAD) of which there are 5

observations of the inner caldera (4 MARSIS, 1 SHARAD). However, we have looked at the MARSIS data, and most of the images do not have the required quality due to ionospheric distortions. As a result, we concentrate our analysis on SHARAD data for both the caldera and fan deposits. For Arsia Mons, there are 3 radargrams available for the caldera.

5.3 Results and discussions

5.3.1 Calderas of Apollinaris and Arsia

Figures 5.4 and 5.5 show the radargrams for Apollinaris and Arsia. As can be seen, the Arsia caldera displays a single bright reflection surface suggesting the presence of volcanic material due to the strong attenuation of the radar signal. In the case of Apollinaris however, the caldera displays two reflecting planes that are not as bright as the one in Arsia which suggests that material in the caldera is not similar. In addition, the Apollinaris caldera is observed to be very smooth from the MOLA-derived pulse width surface roughness map (Figure 5.6, Neumann et al. 2003) that cannot be easily associated with volcanic surfaces. Fluvial deposits are known to exhibit smoother surface than volcanic ones in shield volcanoes where the rapid cooling of the effusive magma often leads to fracturing that increases the surface roughness at the meter-scale.

5.3.2 Fan deposits

The radar data in Figure 5.7 shows that the fan deposits display layering, which suggests that the mechanism of formation continued for some time and it was a multi-stage process. Furthermore, the surface roughness map derived from MOLA pulse width data suggest that the Apollinaris fan is also smoother than typical lava flows. However, these interpretations in addition to the ones about the calderas need to be verified through an accurate clutter analysis to ensure that the observed signals are indeed due to subsurface structures. Such an analysis needs specific software tools that are not available to the author at the time of writing, and therefore, is the focus of an ongoing collaborative work with members of the SHARAD science team.

¹In Radar terminology, "clutter" refers to any surface signal losses other than those due to the attenuation properties of the target medium such as surface roughness, slope difference, and scattering. As a result, it is a common practice to do a "clutter analysis" by modeling the signal losses due to heterogeneities in the surface alone for a certain area and then deducting that from the actual radargram data to isolate the losses due to subsurface attenuation.

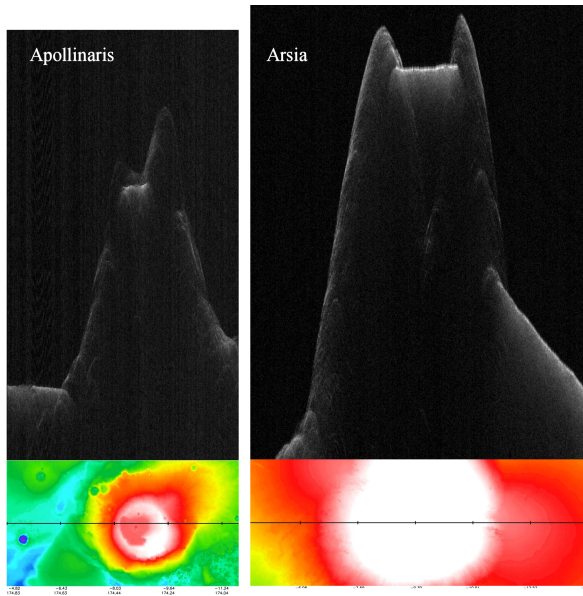


Figure 5.4: Radargrams of Apollinaris(left) and Arsia Mons(right).

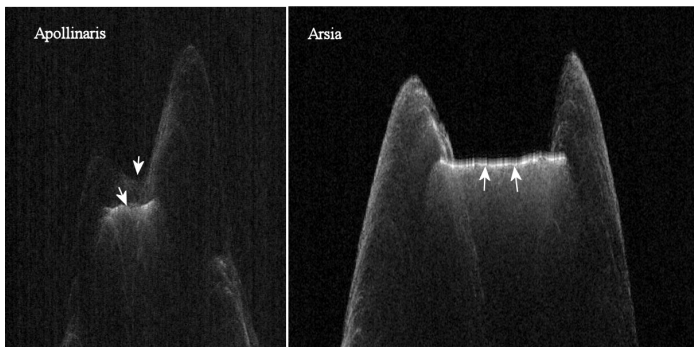


Figure 5.5: Closeup on the calderas of Apollinaris and Arsia Mons. The Arsia caldera displays a single bright reflection surface that is a strong indication of volcanic flows due to the strong attenuation and difficulty of penetration of the radar signal. In the case of Apollinaris however, the caldera displays two reflecting planes.

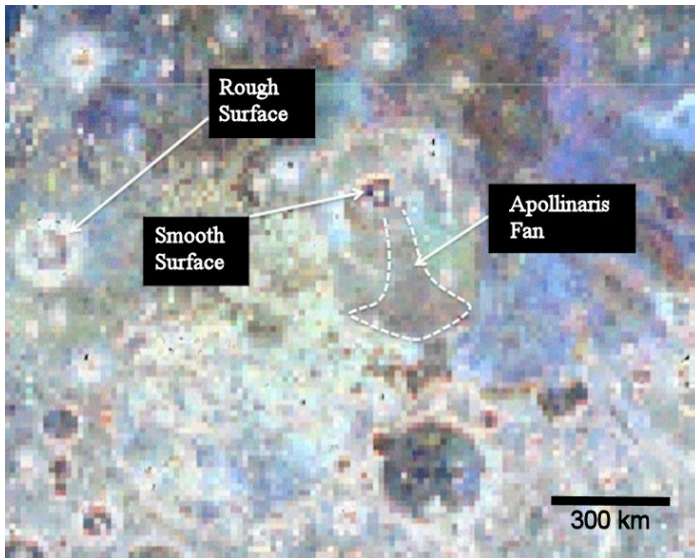


Figure 5.6: MOLA-derived roughness map for the Apollinaris region. Note the smoothness of the caldera region.

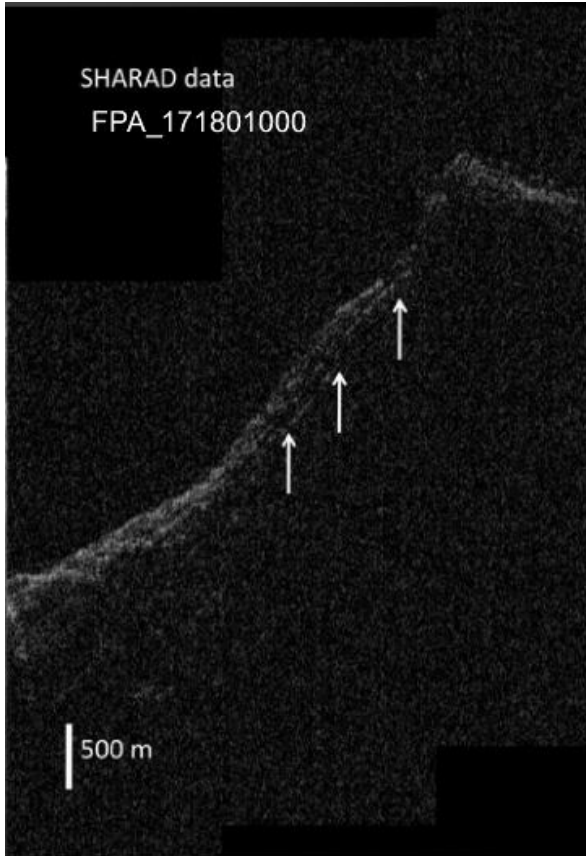


Figure 5.7: Radargram for fan deposits. Note the layering in the upper slopes.

6 Conclusions and Outlook for the Future

As it has been discussed and repeatedly stressed in the previous chapters, the key challenges in locating hydrothermal systems on Mars are the subsurface nature of the hydrothermal deposits making it rather hidden to remote sensing and indeed even in-situ ones that cannot penetrate below the first skin layer of the surface, and the usual similarity of these systems' surface manifestations to other surface features making it difficult to differentiate between them due to a principle of geomorphology termed equifinality.

In chapters 2 and 5, we dealt with two instruments that can tackle the first challenge. In chapter 2 we presented the GRS instrument that can probe into the first meter or so of the subsurface giving information about its general geochemistry, while in chapter 5 we introduced GPR with its ability to deduce the geophysical nature of the subsurface down to around 10 km of the surface as in the case for MARSIS. However, as discussed previously, the information gathered from these instruments attains increased significance when combined with data from other sources such as surface morphology and geologic context.

In chapters 3 and 4, we showed two interesting case studies that dealt with the second challenge: namely, CFPs and surface mounds. In the former, the morphological similarity between desiccation and thermal contraction cracks was demonstrated, and it was shown that through only the added constraints from a physical model it is possible to distinguish between both. In the latter case (i.e. the mounds), it was shown how the mounds can have a periglacial, phreatic, volcanic, glaciovolcanic or even a sedimentary origin yet end up with a morphologically similar surface manifestation. Furthermore, it was shown that only through the added knowledge of geological context and physical measurements of thermal inertia it became possible to at least constrain some of the possible formation mechanisms.

It is hoped that through this study, a deeper appreciation of the benefits of using multiple datasets to treat a given problem will be attained. In addition, while this work has concentrated mainly on combining theoretical work with remote sensing data, it should be noted that further improvements can be achieved through incorporating in-situ measurements as well. Indeed, Landers such as the Vikings, the MERs, and most recently Phoenix, have yielded data that would have been unattainable through remote sensing alone such as the geochemical analysis of scrapped and unscrapped rocks, physical and chemical properties of soils such as pH, electrical conductivity, mineralogy, magnetic properties, and microscopic structure, in addition to diurnal meteorological variations. Even on Earth, such a scheme of combining orbital and in-situ data has led to broader and

more complete understanding of the geological evolution and even habitability as in the case of, for example, the Atacama Desert in Chile (e.g. Piatek et al. 2007): one of the well-known terrestrial analogs for Mars.

The highlights of this work have been:

- The first ever global mapping and description of polygonal features inside Martian impact craters, along with the production of analytical and numerical models to differentiate between these polygonal features and common permafrost polygons allowing for their identification as desiccation cracks that are remnants of mostly impact-generated paleolakes.
- The use of various remote sensing techniques to identify a volcanic site with high potential for magmatic-driven hydrothermal activity through the detection of evidence for surface venting, lahar events, water activity in the vicinity of the volcano, and possibly a volcanic crater lake.
- A correlation for the first time between the GRS water-equivalent hydrogen map in the mid-latitudes and a map of crater density to assess the role of impact events in forming hydrous minerals on Mars.
- A newly devised approach to look for surface/shallow subsurface manifestations of hydrothermal systems using low frequency ground-penetrating radar.

Much remains to be done in perfecting the tools of combining datasets. If we are to address the specific points raised in this study, the devising of an appropriate numerical model of desiccation in Martian conditions remains one of the priorities of the author (see Appendix C for more details). In addition, now that there is a tool to differentiate between desiccation cracks and permafrost polygons, it will be extremely useful to search for them in other areas other than impact craters, for example, in areas of known past hydrologic activity. In regards to magmatic-driven system, Apollinaris can be looked upon as a prelude to larger and more complex areas on Mars where the lessons learnt here can be extended to regions such Elysium, Tharsis, and the Hellas regions. One thing is for sure, there is always more to be done, one more rock to be returned, one more image to be critically observed, and one more place to venture.

A Space Instruments used in this Study

A.1 Compact Reconnaissance Imaging Spectrometer for Mars (CRISM)

The Compact Reconnaissance Imaging Spectrometer for Mars (CRISM) is a hyperspectral imager on the Mars Reconnaissance Orbiter (MRO) spacecraft that has a spectral range of ≈ 0.3 to 4 microns and an ability to attain unprecedented spectral resolutions of ≈ 6 nm. CRISM's objectives are (1) to map the entire surface using a subset of bands to characterize crustal mineralogy, (2) to map the mineralogy of key areas at high spectral and spatial resolution, and (3) to measure spatial and seasonal variations in the atmosphere (Murchie et al. 2007). These objectives are addressed using three major types of observations. In multispectral mapping mode, data are collected at a subset of 72 wavelengths covering key mineralogic absorptions and binned to pixel footprints of 100 or 200 m/pixel. Nearly the entire planet can be mapped in this fashion. In targeted mode a region of interest is mapped at full spatial and spectral resolution (15-19 m/pixel, 362-3920 nm at 6.55 nm/channel). Ten additional abbreviated, spatially binned images are taken before and after the main image, providing an emission phase function (EPF) of the site for atmospheric study and correction of surface spectra for atmospheric effects. In atmospheric mode, only the EPF is acquired. Global grids of the resulting lower data volume observations are taken repeatedly throughout the Martian year to measure seasonal variations in atmospheric properties. The datasets can be browsed rather rapidly thanks to summary products based on multispectral parameters that are derived from reflectances in key wavelengths for every CRISM observation (Pelkey et al. 2007). There are 44 summary products formulated to capture spectral features related to both surface mineralogy and atmospheric gases and aerosols. The CRISM summary products are also used as an analysis tool to characterize composition as well as a targeting tool to identify areas of mineralogic interest to observe at higher spectral and spatial resolution.

A.2 Context Imager (CTX)

The Context Camera (CTX) on the Mars Reconnaissance Orbiter (MRO) is a telescopic camera that has a resolution of 6m/pixel. In any other mission, such an instrument would be considered the main high resolution camera onboard. However, this is not the case on the MRO, and the CTX serves as a context camera to the HiRISE one. CTX provides con-

text images for data acquired by other MRO instruments, observes features of interest to NASA's Mars Exploration Program (e.g., candidate landing sites), and conducts a scientific investigation, led by the Mars Color Imager team (MARCI), of geologic, geomorphic, and meteorological processes on Mars. CTX consists of a digital electronics assembly; a 350 mm f/3.25 Schmidt-type telescope of catadioptric optical design with a 5.7° field of view, providing a ≈30-km-wide swath from ≈290 km altitude; and a 5000-element CCD with a band pass of 500-700 nm and 7 μm pixels, giving ≈6 m/pixel spatial resolution from MRO's nearly circular, nearly polar mapping orbit. More technical information can be found in Malin et al. (2007).

A.3 Gamma Ray Spectrometer (GRS)

The Mars Odyssey Gamma-Ray Spectrometer (GRS) is designed to record the spectra of gamma rays emitted from the Martian surface as the spacecraft (Mars Odyssey) passes over different regions of the planet. The gamma rays arise from both radioactive decay and the nuclear interaction of elements with cosmic-ray particles. The energies of the gamma rays identify the elements responsible for the emissions, and their intensities determine the concentrations. In addition, the instrument also has the capability to determine the fluxes of thermal, epithermal, and high-energy neutrons coming from the surface of the planet (Boynton et al. 2004). The GRS instrument suite consists of the Gamma Subsystem (GS), Neutron Spectrometer (NS), and the High Energy Neutron Detector (HEND). The data used in this study is derived from the GS, which consists of a passively cooled, n-type, reverse biased, high-purity Ge detector mounted on a 6 m boom (Boynton et al. 2004). The gamma-ray detection system has no collimation or focusing system, which means that the gamma rays are recorded from all directions. 50% of the rays collected from the surface are from within a radius of 200-300 km from nadir (Boynton et al. 2004), which defines the GRS footprint. Consequently, the optimal way to use the GRS data is in the context of regional scales. The data is displayed as 5° by 5° bins in a cylindrical grid on the Martian surface (5° is equivalent to ≈300 km at the equator). These regions get smaller in area as they get closer to the poles, but they contain approximately the same number of spectra because the spacecraft passes over there more frequently.

The concentration of each element is directly related to the intensity of its emission line(s). However, for the lines produced via neutron interactions, such a direct approach is not accurate because the neutron flux is a function of composition. Instead, a pre-defined model is generated to predict the flux of gamma rays for an assumed surface composition; the observations are compared to the predictions. For the naturally radioactive elements, K and Th, no neutrons are involved and the model is easy to calculate. The surface emission rate can be calculated from an assumed model abundance of the element, the known disintegration rate for the gamma ray of interest, and the attenuation of that gamma ray from depth using mass attenuation coefficients for a typical Mars surface composition. For the other elements whose gamma rays are generated by interaction with neutrons, the calculations are a bit more complicated. The production of neutrons is modeled with a Monte Carlo code, MCNPX (McKinney et al. 2006); for an incoming flux of cosmic rays that interact with the atmosphere and the surface. While this approach appears to provide reasonable results in the equatorial and midlatitudes, the presence of large amounts of

water ice buried near the surface toward high latitudes makes the correction technique less effective due to both the strong influence of H on neutron flux and the effects of layering at the surface. As a result, the final data processing leads to the generation of maps of elemental mass percentages in the regions from 45°N to 45°S for non-radioactive elements, and 75°N to 75°S for naturally radioactive ones (e.g. K and Th). At the time of writing there are maps for the elements Cl, Fe, H, Si, K, Th, Ca, Al and S.

A.4 High Resolution Science Experiment (HiRISE)

HiRISE, as the name implies, is a high resolution telescopic camera on board the Mars Reconnaissance Orbiter (MRO) operating in a "push broom" mapping method. HiRISE includes broad-band color capability. In addition to the red-filter channels extending over the full swath width, the central 20% of the swath can be imaged with additional CCDs that are covered with blue-green or NIR filters. However, the most impressive part about this instrument is its ability to map the surface at an unprecedented resolution that may reach 25cm/pixel allowing for the detection of sub-meter structures such as small rocks and layering in sedimentary sequences. In addition, by taking images for the exact location on different flights, it allows for stereographic reconstruction and the creation of high resolution digital image models. More information can be found in McEwen et al. (2007).

A.5 Mars Orbiter Laser Altimeter (MOLA)

MOLA calculates topographical elevation by measuring round trip times of individual laser pulses between the Mars Global Surveyor and the Martian surface (Smith et al. 2001). The laser pulse is time-stamped with respect to the spacecraft's internal time with a time stamp resolution of 1/256 s. The precision of MOLA range measurements is almost 40 cm for smooth flat surfaces and ≈ 10 meters for rough tilted ($>30^\circ$) terrains. More technical aspects can be found in Smith et al. (2001).

A.6 Radar Sounders MARSIS and SHARAD

MARSIS (Mars Advanced Radar for Subsurface and Ionospheric Sounding) is a multi-frequency, synthetic-aperture, orbital sounding radar that has two observation modes: An ionospheric mode, and a subsurface one. In the subsurface mode, MARSIS operates in four frequency bands between 1.3 and 5.5 MHz. Lateral spatial resolution depends on surface roughness, but for most Mars surfaces, the cross-track footprint is 10-30 km, and the along-track is 5-10 km with a vertical resolution of ≈ 50 -100m. Because MARSIS images can be affected by ionospheric distortions, the higher frequency bands (4 and 5 MHz) and nighttime measurements are more commonly used to minimize the effect of the ionosphere.

SHARAD (SHallow RADar) is a sounding radar provided by Agenzia Spaziale Italiana (ASI) as a Facility Instrument on the Mars Reconnaissance Orbiter mission. Its

20-MHz center frequency and 10-MHz bandwidth complement the lower-frequency, relatively narrower bandwidth capability of the MARSIS sounding radar onboard Mars Express. Vertical and horizontal resolutions are, respectively, 10-20 m and 3-6 km (cross-track) by 0.3-1 km (along-track). The primary objective of the SHARAD experiment is to map, in selected locales, dielectric interfaces to several hundred meters depth in the Martian subsurface and to interpret these results in terms of the occurrence and distribution of expected materials, including competent rock, soil, water and ice. This is a seemingly cautious set of objectives, making no particular promises about the unique detection of any specific material (e.g., water). Nevertheless, the subsurface of Mars presents ample possibilities for dielectric contrasts.

The dielectric constant depends on both rock porosity and rock composition, so boundaries between materials with differences in these properties are dielectric reflectors. This dielectric contrast could arise, for example, from sedimentary materials in contact with basaltic rock, from ice in contact with solid rock, or from ice-saturated porous rock in contact with ice-free porous rock. These contrasts alone lead to a large variety of subsurface targets for SHARAD and MARSIS to map. Examples include mapping of (1) the polar layered deposits, both their internal layers and contact with underlying bedrock, (2) the layering within sedimentary rock sequences, (3) buried impact craters in the northern lowlands, (4) buried channels, (5) volcanic stratigraphy, (6) shallow ice bodies, and (7) potential shallow water accumulations (Seu et al. 2007).

A.7 The Thermal Emission Imaging System (THEMIS)

The Thermal Emission Imaging System (THEMIS) on 2001 Mars Odyssey investigates the surface mineralogy and physical properties of Mars using multi-spectral thermal-infrared images in nine wavelengths centered from 6.8 to 14.9 μm , and visible/near-infrared images in five bands centered from 0.42 to 0.86 μm (Christensen et al. 2004b). THEMIS has mapped the entire planet in both day and night multi-spectral infrared images at 100 m/pixel resolution, and >95% of the planet in one-band visible images at 18 m/pixel, in addition to significant parts of the planet in 5-band visible color. This dataset allows for determining the mineralogy of localized deposits associated with hydrothermal or sub-aqueous environments, study small-scale geologic processes and landing site characteristics using morphologic and thermophysical properties, investigate polar cap processes at all seasons using infrared observations at high spatial resolution, and allows for the derivation of other maps in high resolution such as thermal inertia maps.

B Mapped CFPs

Table B.1: Craters with CFPs in the northern hemisphere. Locations with image IDs or bold font signify CFPs that are either well preserved or in an interesting geologic context. Image IDs starting with "PSP" refer to HiRISE images, "M", "R" or "S" refer to MOC, while "P" refers to CTX images. Other acronyms in the tables are: Crater D.: Crater Diameter, Av. P.S.: Average polygon size, R: Rampart, G: Gullies, Sd: Sedimentary deposits, L: Layering, Ri: Ridges, ? : Tentative or unclear detection, Sh: Shoreline/Strandline, M: Mounds, T: Terraces, D: Delta, TCP: Thermal Contraction Polygons

#	Lat (N)	Lon (E)	Crater D. (km)	Av. P.S.	R/G	Lake Signs	Notes/Image ID
1	79.2	60.5	24	65	R	Sd, L	small patch visible beneath the ice
2	74.7	13.4	13	140	R	Sd	Clear remnants
3	71.1	157.5	13.5	120	R	Sd	Smaller TCPs embedded within
4	70.3	266.5	27	90	R	Sd	Flow lobes, younger TCPs overly the older larger CFPs
5	70.2	103.2	33	75	R	Ridges?	Louth Crater. Hight tentative troughs in ejecta
6	70.1	13.9	12.5	150	R	Sd	PSP_7650_2505
7	70.1	64.6	17	160	R	Sd	E1900409
8	69.8	64.8	18	165	R	Sd, Sh, M?	
9	69.4	162.6	15	100	R	Sd	
10	69.3	41.5	21	120	R	Sd	
11	69.1	123.3	15	165	R	Sd	P17_7501_2486

...continued on next page

Table B.1 – continued from previous page

#	Lat (N)	Lon (E)	Crater D. (km)	Av. P.S.	R/G	Lake Signs	Notes/Image ID
12	68.9	26.7	15	125	R	Sd, M, Sh?	Mound's diameter 220 meters
13	68.5	149	14	125	R	Sd	
14	68.5	12.9	14	135	R	Sd, Sh(Ri)	P17_7571_2487
15	68.4	189.4	12	160	R/G	Sh?	Cracks are very faint
16	68.4	212.3	12	130	R	Sd, Ri	
17	68.3	235.4	10	85	R	Sd	Heimdal Crater, 20 km from Phoenix, faint traces
18	68.3	266.3	5	125	R	Sd	
19	68.2	201.6	16	130	R	Sd,Sh,M?	P16_7195_2477
20	68.1	199.3	17	160	R	Sd	
21	68	173.2	9	140	R	Sd	
22	67.5	26.6	7	230	R	Sd	
23	67.3	97	7	160	R	Sd	
24	67.3	192.9	15	130	R	Ri?	
25	67.2	249.7	22	140	R	Sd, Sh	
26	67.2	24.8	4.5	115	R	Sd	Poor Visual conditions
27	67.2	47.8	14	120	R	Sd, M, Sh	PSP_7372_2475
28	67.1	97.5	18	230	R	Sd	Some Polygons are measuring up to 340 meters
29	67.1	113.5	20	100	R	Sd, L	
30	67.1	202.1	17	150	R	Sd	P16_7195_2477
31	67	252	10	160	R	Sd	
32	67	338.7	7	110	R	Sd	
33	66.9	343.7	13	150	R	Sd, Sh	P16_7348_2471
34	66.8	131.3	15	165	R	Ri	P17_7514_2470
35	66.7	97	12	150	R	Sd	P16_7212_2472
36	66.6	97.5	9	170	R	Sd	
37	66.6	25.2	5	115	R	Sd	Poor Visual conditions
38	66.4	144	28	100	R	Sd	
39	66.4	163.4	24	135	R	Sd, Sh?	Possible Phyllosilicates on the Crater rim

...continued on next page

Table B.1 – continued from previous page

#	Lat (N)	Lon (E)	Crater D. (km)	Av. P.S.	R/G	Lake Signs	Notes/Image ID
40	66.2	81.4	17.5	140	R	Sd, Ri	
41	65.8	26.7	5	130	R	Sd	
42	65.8	67	3	175	R	Sd	
43	65.6	329.4	20	110	R	Sd	Dunes overlying the polygons
44	65.6	338.7	18	120	R	Sd	Dunes overlying the polygons
45	65.5	128.5	26	145	R	Sd	P18_7936_2456
46	65.5	63.3	4	135	R	Sd	
47	65.3	257.8	7	90	R	Sd	
48	65.3	32.4	7	155	R	Sd	M1900047
49	65.2	243.8	8	115	R	Sd, T?	
50	65.2	339.1	8	140	R	Sd	
51	65.1	23.3	5	120	R	Sd	
52	65.1	70.7	12	100	R	Sd, Sh	
53	64.9	155.5	13	110	R	Sd, L	
54	64.9	31.2	20	125	R	Sd, M, Sh	
55	64.7	283	9	100	R	Sd	Faint fractures, poor visual conditions
56	64.5	67.3	17.5	175	R	Sd, M, Sh	Analgyph available
57	64.3	70.3	7	215	R	Sd, M	
58	64.2	37.4	4	130	R	Sd	
59	63.9	219.7	13	100	R	Sd, T	
60	63.9	4.9	8	125	R	Sd, Sh?	
61	63.8	171	9	120	R	Sd	
62	63.8	37.6	5	175	R	Sd, M	
63	63.6	170.1	15	125	R	Sd	
64	63.5	131.8	20	125	R	Sd	P17_7659_2438
65	63.2	165.1	15	150	R	Sd	
66	63.1	339.3	10	85	R/G	Sd	
67	63	320.1	18	110	R	Sd	Dunes overlying the polygons
68	62.9	254.1	4	80	R	Sd	Troughs rarely intersecting
69	62.4	103.4	13	175	R	Sd	
70	62.4	171	5	190	R	Sd	R1701759
71	62.4	336.3	9	120	R	Sd	

...continued on next page

Table B.1 – continued from previous page

#	Lat (N)	Lon (E)	Crater D. (km)	Av. P.S.	R/G	Lake Signs	Notes/Image ID
72	62.4	81.7	10	180	R	Sd, Sh?	
73	62.2	13.9	11	100	R	Sd, ?	Faint fractures, poor visual conditions
74	62.1	147.5	9	135	R	Sd	
75	62	351.7	8	95	R	Sd	Faint fractures, poor visual conditions
76	62	6.6	25	130	R	Sd	
77	62	61.6	4	145	R	Sd, M?, Sh?	
78	61.9	283.3	9	75	R	Sd, Sh?	Faint fractures, poor visual conditions
79	61.9	54.5	5	185	R	Sd	
80	61.7	171	16	200	R	Sd	PSP_007539_2420
81	61.7	70.7	12.5	120	R	Sd, Ri?	
82	61.5	21.8	13	140	R	Sd, M, Sh	P19_8375_2418, E2101593
83	61.4	151.2	6	160	R	Sd	
84	61.4	269.4	6	160	R	Sd	
85	61.3	78.5	7.5	135	R	Sd, Sh	
86	61.2	358.1	13	125	R	Sd	Faint fractures, poor visual conditions
87	61	24.1	12	135	R	Sd, M, Sh?	
88	61	43.2	6.5	100	R	Sd	
89	60.9	31.1	6	115	R	Sd	
90	60.7	151.1	7	180	R	N	
91	60.6	35.6	5	155	R	Sd, M?	
92	60.6	189.7	18	160	R	Sd, Sh?	Thermokarst Pits
93	60.6	72.2	17	130	R	Sd, M, Sh?	Binary Crater
94	60.6	89.7	20	110	R/G	Sd, Sh	
95	60.5	199.2	13	170	R	Sd, M?	
96	60.4	115.8	17	180	R	Sd	
97	60.4	147.7	20	125	R	Sd, Sh?	
98	60.4	83.8	11.5	130	R/G	Sd, Sh?	
99	60.3	123.5	12	120	R	Sd	
100	60.3	129.4	21	120	R	Sd	
101	60.3	271.6	14	90	R	Sd	

...continued on next page

Table B.1 – continued from previous page

#	Lat (N)	Lon (E)	Crater D. (km)	Av. P.S.	R/G	Lake Signs	Notes/Image ID
102	60.2	283.5	15	90	R	Sd, Sh?	Faint fractures, poor visual conditions
103	60.1	173.5	9	100	R	Sd	
104	60.1	213.8	14	155	R	Sd, T	
105	60.1	211.8	6	135	R	Sd	Nested in a larger weatherd crater
106	60.1	251.1	24	160	R	Sd, Sh?	
107	60.1	263.2	12	150	R	Sd	
108	60	56.5	14	140	R	Sd, M, Sh	
109	59.9	228.1	10	200	R	Sd, M?	Faint fractures/poor visual conditions
110	59.9	302.5	13.5	60	R/G	Sd	Traces below younger sediments
111	59.8	136	32	90	R	Sd	
112	59.7	157.8	7	150	R	Sd, M	Faint fractures, poor visual conditions
113	59.7	52.7	11.5	170	R	Sd	S1500448
114	59.5	151.3	7	195	R	Sd	Faint fractures, poor visual conditions
115	59.5	263.6	12	175	R	Sd, M	
116	59.4	302.5	23	50	R/G	Sd	Traces below younger sediments
117	59.2	181.5	8.5	205	R	Sd, M	
118	58.8	82.4	11.5	75	R/G	Sd	Remnants. Anal- glyph present
119	58.8	263.4	5	170	R	Sd, M	
120	58.3	67.7	14	135	R	Sd, Sh?	Thermokarst Pits
121	58.2	74.7	18	135	R/G	Sd	
122	58.1	62.2	22.5	135	R/G	Sd	
123	57.9	47.4	5.5	115	R	Sd	
124	57.6	187.1	11.5	160	R	Sd, M?, Sh	Faint fractures, poor visual conditions

...continued on next page

Table B.1 – continued from previous page

#	Lat (N)	Lon (E)	Crater D. (km)	Av. P.S.	R/G	Lake Signs	Notes/Image ID
125	56.4	263.2	13	180	R	Sd	
126	56.2	22.6	15	200	R	Sd, Sh?	R1901447
127	56.1	50.1	12	185	R	Sd, Sh?	
128	55.5	139.7	26	100	R	Sd	Thermokarst Pits
129	55.2	154.5	6	115	R	Sd	Faint fractures, poor visual conditions
130	53.2	101.5	16	200	R	Sd	Thermokarst Pits
131	51.2	347.9	11.5	160	R	Sd	
132	51	347.1	11	185	R	Sd	
133	50.7	341.6	12	125	R/G	Sd, M, Sh	PSP_001942_2310
134	49.8	317.6	9.5	155	R	Sd	R1602192
135	49.5	325.3	11.5	170	R/G	Sd, Sh?	
136	49.2	316.2	10.5	90	R/G	Sd	
137	48.8	318.3	7.5	135	R/G	Sd, M	Analgyph available
138	48.1	326.7	13	145	R/G	Sd	Binary Crater
139	47.1	322	10.5	225	R/G	Sd	
140	43.9	89.5	14	65	R	Sd, M?	Thermokarst Pits. Analgyph available
141	43.1	91	7.5	85	R	Sd	Traces. Thermokarst pits
142	41.5	87.7	18	90	R	Sd, L, Sh?	
143	38.6	137.2	29	60	R/G	Sd	Cracks in the Ejecta, PSP_8951_2185
144	36.5	351	55	85	N	Sd, Sh	P06_3445_2163
145	28	73.3	73	40	N	Sd, L, D	
146	27.7	67.2	60	50	N	Sd, L	Highly variable in size from 15 m up to 80 m
147	21.6	60.7	395	12	N	Sd, M, Sh	Antoniadi Crater, associated with inverted channels
148	20	79.4	72	50	N	Sd, D?, Sh?	Highly variable in size from 15 m up to 200 m

...continued on next page

Table B.1 – continued from previous page

#	Lat (N)	Lon (E)	Crater D. (km)	Av. P.S.	R/G	Lake Signs	Notes/Image ID
149	18.4	77.7	49	15	N	Sd, D, L, Sh?	Jezero Crater, PSP_3798_1985
150	15.2	333.2	56	135	N	Sd, L, Sh	old filled fractures
151	11.9	313.3	50	130	N	Sd, D, L, Sh	Edge of fan deposits,
152	8.2	310.6	72	20	N	Sd, D, L, T, Sh?	In delta deposits
153	1.2	134	45	30	R	Sd, Sh	Clear remnants, PSP_7923_1810

Table B.2: Craters with CFPs in the southern hemisphere.
Same acronyms apply

#	Lat (N)	Lon (E)	Crater D. (km)	Av. P.S.	R/G	Lake Signs	Notes/Image ID
1	-76.5	6.2	15	60	?	Sd, ?	Remnants, Smaller polygons embedded within
2	-76	248.5	17	100	R	Sd	Pedestal Crater
3	-75.9	101.3	10	100	R	Sd	Thermal contraction polygons embedded within
4	-75.5	86.6	7.5	80	?	Sd	
5	-72.8	259.9	13	70	R	Sd	
6	-72.2	98.7	35	120	R	Sd	Uniformly squared
7	-71.9	65.4	11	80	R	Sd	
8	-71.1	260	28	95	R	Sd, ?	
9	-70.7	48.3	13	220	R	Sd	In ejecta deposits
10	-70	216.9	4.5	70	R	Sd	
11	-69.3	96.6	27	80	R	Sd, M?	
12	-69.3	275.7	9.5	120	R	Sd, ?	
13	-69	29.9	7	65	R	Sd	
14	-68.9	118.9	7.5	120	R	Sd	
15	-68.9	273.9	17.5	90	R	Sd	
16	-68.9	297	12.5	120	N	Sd, ?	Nested
17	-68.7	260.9	15.5	120	R	Sd	
18	-68.7	61.8	20	120	R	Sd, ?	

...continued on next page

Table B.2 – continued from previous page

#	Lat (N)	Lon (E)	Crater D. (km)	Av. P.S.	R/G	Lake Signs	Notes/Image ID
19	-68.6	329.9	30	95	R	Sd	Poor visual conditions
20	-68.4	1.6	53	100	G	Sd, M, L?	Large gullied pit inside the crater
21	-68.2	215.4	4	40	N	Sd	Highly degraded crater
22	-68	100.4	27	160	N	Sd,?	
23	-67.9	102.1	9.5	120	R	Sd, M?	
24	-67.9	50.3	30	130	R	Sd, Sh	
25	-67.9	85	10	105	R	Sd	Nested Crater, Troughs in floor and ejecta
26	-67.5	289.2	30	150	R	Sd,?	
27	-67.5	22.5	14	75	R	Sd, Sh?	
28	-67.2	49.2	30.5	125	R	Sd, Sh	
29	-66.9	62	4.5	55	R	Sd	
30	-66.8	120.1	6	135	R	Sd	
31	-66.8	20.7	33.5	60	R	Sd, ?	
32	-66.7	303	11	100	R	Sd, M?	Poor visual conditions
33	-66.6	72.3	7.5	115	R	Sd, ?	
34	-66.4	65.6	12.5	75	R	Sd, ?	
35	-66.3	62	15	105	R	Sd	
36	-66.2	84	10	80	R	Sd, ?	
37	-65.6	301.9	7.5	120	N	Sd	
38	-65.4	21.1	34	140	R	Sd, ?	In crater floor and ejecta
39	-65.4	45.6	19	100	R	Sd, ?	
40	-65.3	85.9	23	90	N	Sd, M?	
41	-65.3	313.3	22	70	R/G	Sd, Sh	
42	-65.2	259.2	10.5	135	R	Sd	
43	-65.2	307.1	20.5	100	R	Sd,?	Very poor visual conditions
44	-65.2	312.3	27	110	R/?	Sd, Sh?	
45	-65	111.4	23	105	R	Sd,?	
46	-65	32.9	27.5	55	R	Sd, M, T?	
47	-64.9	6.6	20	70	N	Sd, M	
48	-64.6	99.2	12	100	R	Sd, ?	
49	-64.6	67	10.5	95	R	Sd, ?	

...continued on next page

Table B.2 – continued from previous page

#	Lat (N)	Lon (E)	Crater D. (km)	Av. P.S.	R/G	Lake Signs	Notes/Image ID
50	-64.5	236.6	8	135	R	Sd, M?	
51	-64.5	312.8	3	95	R	Sd	
52	-64.4	255.3	13	140	R	Sd	PSP_4082_1155
53	-64.3	79.8	15	80	N	Sd	Nested, and partially buried by fractured deposits
54	-64.1	312.5	4	90	R	Sd	
55	-63.7	127.4	6	120	R	Sd, M	Binary Crater
56	-63.7	247.7	11	150	R	Sd, M?	S1402148
57	-63.5	58.2	26	80	R	Sd	
58	-62.8	128.2	8	110	R	Sd	
59	-62.8	282.3	38	75	N	Sd, Sh?	
60	-62.8	320.6	4	100	N	Sd	Nested
61	-62.6	115.5	9	120	R	Sd	
62	-62	273.4	16	120	R	Sd, M?	
63	-62	49.7	12.5	130	R	Sd, ?	
64	-61.8	118.1	16	105	R	Sd	Nested
65	-61.5	25.8	18	140	R	Sd,?	
66	-61.1	27.6	13	110	R	Sd, M	
67	-60.8	36.5	13.5	200	R	Sd, M?	Remnants
68	-60	163.3	12.5	140	R	Sd	
69	-59.8	336.3	28	115	R	Sd, M	Remnants
70	-58.9	111.8	38	150	R	Sd, L?	
71	-58.6	17.9	12	70	R	Sd, M?	On the rim of a larger crater
72	-58.4	240.2	12	130	R	Sd	Tentative, Poor visual conditions
73	-58.4	40.4	22	100	R	Sd, T	
74	-57.6	215.6	12	160	R	Sd, ?	Clear remnants in the center
75	-57.5	274.4	10	110	R	Sd, M	Remnants
76	-57.4	33.8	21	120	R	Sd, ?	
77	-57.4	41.5	16	150	R	Sd	M0904950
78	-55.9	337.9	22	100	R	Sd	Remnants
79	-54.5	261.8	9	120	R	Sd	
80	-54.5	318.6	1800	140	N	Sd	Argyre, PSP_2128_1250
81	-54.4	293.5	12	100	R/G	Sd	Remnants
82	-51.6	308.4	1800	100	N	Sd	Argyre

...continued on next page

Table B.2 – continued from previous page

#	Lat (N)	Lon (E)	Crater D. (km)	Av. P.S.	R/G	Lake Signs	Notes/Image ID
83	-51.4	271.6	20	150	R	Sd	Remnants
84	-50.4	200	30	60	R/G	Sd, T	Weathered patterns
85	-48.5	234.8	10	120	R/G	Sd, M, Sh?	Degraded features
86	-47	324.5	1800	110	N	Sd	
87	-46.8	74.7	2300	100	N	Sd, L, Sh?	
88	-46.1	248.3	12	100	R	Sd	Nested
89	-45.9	45.8	14	95	R/G	Sd, M	Thermokarst pits
90	-45.8	284.7	10	90	R/G	Sd	Features on the crater wall
91	-43.4	0.5	20	95	R	Sd, Sh?	
92	-42.9	53	2300	80	N	Sd, L, Sh?	
93	-42.6	52.4	2300	90	N	Sd, L, Sh?	
94	-41.9	71.3	16	150	N	Sd	
95	-41.8	51.6	2300	50	N	Sd, L, Sh?	
96	-41.3	14.1	20	75	R	Sd, M	
97	-41.1	53	2300	V	N	Sd, L, Sh?	PSP_6911_1385
98	-40.5	54.3	2300	40	N	Sd, L, Sh?	Variable in diameter from 20m to 170m
99	-40.2	52.1	2300	100	N	Sd, L, Sh?	
100	-40.1	52.6	2300	120	N	Sd, L, Sh?	Hellas/ PSP_6555_1395
101	-39.7	54.1	2300	V	N	Sd, L, Sh?	
102	-39.6	56.7	34	80	R	Sd	Nested
103	-39.2	54.8	2300	V	N	Sd, L, Sh?	Hellas/ PSP_7346_1405
104	-39.2	53.5	2300	70	N	Sd, L, Sh?	
105	-39	181.8	50	15	R/G	Sd	PSP_3979_1410
106	-38.8	55.5	2300	85	N	Sd, L, Sh?	
107	-38.7	54.5	2300	150	N	Sd, L, Sh?	
108	-38.4	55.9	2300	20	N	Sd, L, Sh?	PSP_7781_1410
109	-38.1	217.9	30	110	R/G	Sd	
110	-38	144.3	50	100	R/G	Sd, D	Raised rims possibly dunes
111	-37.8	81.7	11	75	R/G	Sd, M?	Polygons on the crater wall
112	-37.5	51.3	10	60	R	Sd	Nested

...continued on next page

Table B.2 – continued from previous page

#	Lat (N)	Lon (E)	Crater D. (km)	Av. P.S.	R/G	Lake Signs	Notes/Image ID
113	-37.2	143.3	41	100	R/G	Sd, D, Sh	Raised rims possibly dunes
114	-37.1	10.3	6	45	N	Sd	Highly deformed
115	-35	156.2	26	250	G	Sd, Sh	
116	-27	180.4	60	15	N	Sd, Ev	Crater breached. Chloride deposits
117	-26.6	325.6	148	15	G	Sd, L, D, Ev, Sh?	Holden Crater
118	-23	15.7	160	10	R/G	Sd, D	Bakhuysen Crater, troughs in fan deposits
119	-14.5	175.5	150	10	N	D,T,Sd,Sh,M	Gusev Crater
120	-9.6	308.6	77	60	N	T, Sd, Sh	Morella Crater (Komatsu et al. 2009)
121	-5.3	137.8	152	40	N	Sd,M,Sh,L	Gale Crater
122	-5	180	20	15	R	Sd, D, Sh	Inverted relief
123	-2.9	353	160	7.5	N	Sd, Ev, Sh?	Miyamoto Crater (Wiseman et al. 2008)
124	-2.3	354.8	20	15	N	Sd, Ev, L	Endeavor Crater (Wray et al. 2009)

C A Numerical Model for Formation of Giant Desiccation Polygons on Mars

C.1 Preface

This section builds upon the work presented in chapter 3 by devising a numerical model for desiccation under Martian conditions. This is currently a work in progress, and as such only the results for a pre-fracture model will be presented here. This work has been already introduced at the 2009 Europlanet Science Congress in Rome, Italy, and the American Geophysical Union fall meeting in San Francisco, U.S. (see publication list).

C.2 Soil desiccation cracks: A review

Soils shrink in response to changes in stress condition. This can be achieved either through loss of volume in response to cooling, or through loss of volatile material such as ice or liquid water through desiccation. Desiccation is usually achieved through evaporation from the surface, or diffusion processes that can manifest either in the migration of liquid water due to differences in water potentials, or vapor transport due to changes in water vapor pressure. If the soil is not allowed to contract to account for the loss of volatiles, stress builds up till a point where it exceeds the strength of the soil at which point cracks appear and relieve the excess stress. As these cracks would tend to develop in both horizontal dimensions, they usually intersect and form polygonal networks. The depth and spacing of these cracks depends on many factors, but mainly on the thickness of the stressed zone (Lachenbruch 1961, 1962). As a result, desiccation cracking polygons can be in the order of centimeters if the stressed region is a thin surficial layer undergoing evaporation similar to common mud cracks, or it can be in the order of hundreds of meters if the stressed region is thick enough due to intense evaporation and lowering of the water table.

The degree to which a soil contracts with loss of volatiles (usually water) depends on its capacity for holding these volatiles on a macro scale through having a significant pore or void volume within the solid structure, and on a micro scale through its chemical activity and/or ability to accommodate volatile molecules within its crystal structure. Generally, the more clayey the soil is, the more it will shrink with desiccation. In addition, some clay minerals are known for their chemical affinity to swell and accommodate considerable amounts of water through formation of water interlayers on a molecular level.

This property ranges in clay minerals from being able to swell up to several magnitudes beyond their "dry" volume such as Na-rich montmorillonite, to other clays such as Kaolinite which entirely lack such a behavior.

C.3 Terrestrial analogs: Giant desiccation polygons

There are very few well-documented examples of giant desiccation polygons from the rock record (Loope and Haverland 1988). Desiccation polygonal cracks on Earth are usually centimeters up to a couple of meters at most. However, there are reported cases of giant desiccation polygons that can reach up to 300 meters in size (Neal et al. 1968). Such polygons usually occur in playa deposits, and are attributed to episodes of intense evaporation and lowering of the water table due to geological conditions or excessive human irrigation activities. Mineralogical investigations of soils that display such large features show them to be predominantly fine soils ($2\mu\text{m}$ on average) containing clay minerals (mainly montmorillonite, illite, vermiculite, and chlorite), carbonates, and analcites (Neal et al. 1968). More recent investigations on giant desiccation polygons that were witnessed in the process of formation showed the soil to be rich in Na-montmorillonite (Harris 2004), while other studies have confirmed that the fissures initiate at depth, forming linear cracking patterns at first (Messina et al. 2005).

Detailed field analysis by Neal et al. (1968) at 39 locations in the US containing giant desiccation polygons has shown that the sediments are remnant lacustrine clays and silts from former lakes. These sediments can often be more than 50 meters thick. Neal et al. (1968) concluded that these features are one-time ruptures that can take up to several years to form on account of the thickness of the stressed zone and the generally low permeability of the sediments in addition to substantial resistance to strain in the clays.

C.4 Modeling desiccation: principles and challenges

There is a significant lack of interest in modeling desiccation in the planetary science field as opposed to modeling thermal contraction. While there have been significant efforts put into modeling thermal contraction to explain permafrost polygons on Mars (e.g., Mellon et al. 1997, 2008), or putative small thermal contraction features on Venus, (Anderson and Smrekar 1999), little attention is given to desiccation. This is understandable since desiccation usually implies liquid water and warm conditions to support evaporation which are not conditions seen on other planetary bodies today. On the other hand, there has been extensive work done on modeling desiccation on Earth for civil engineering and agricultural applications (e.g., Konrad and Ayad 1997, Kodikara et al. 2004, Hu et al. 2006, Nahlawi and Kodikara 2006, Peron et al. 2009a, 2009b, Amarasiri et al. 2010) since shrinking/swelling behavior and desiccation of clayey soils can create hazardous situations for civil structures and underground pipes. As a result, we draw a lot of the foundations of our desiccation model from these works.

When dealing with desiccation it is usually both practical and convenient to model the desiccation process in isothermal conditions. That way, temperature-dependent parameters can be better constrained. This is needed in order to simplify the numerical models since most of the important parameters are additionally sensitive to the water content of

the soil. Notable soil parameters with such properties are the suction, elastic moduli such as Young's modulus and shear modulus, tensile and shear strengths, the hydric expansion/shrinkage coefficient, and hydraulic conductivity (better known as permeability to the planetary community). We discuss these parameters briefly.

When a saturated soil (all voids are filled with water) is subjected to a continuous decrease in water content, negative pressures or suctions develop in the porous network of the soil which keeps on increasing as moisture content is lowered. If the soil is unrestrained this leads to a buildup of effective stress (due to lowering of pore water pressure) that leads to shrinking of the soil through consolidation. Another outcome of the buildup of soil suction is the increase in the soil's strength and its elastic moduli as result of its increased stiffness (Towner 1987). The amount of shrinkage that occurs with desiccation is characteristic of a given soil depending on the void ratio (volume of pores/volume of solid material) and the physical and chemical affinity of the soil to absorb water. During a desiccation process, several stages can be identified (Towner 1987, Konrad and Ayad 1997, and references therein). In the first stage, the volume decrease of the soil is equal to the volume of water lost. During that stage, the soil remains saturated over a certain range of moisture content. In the second stage, air starts to enter the soil pore network as further moisture loss occurs. In this stage, the decrease in soil volume is significantly less than the volume of water loss. In the third stage, no significant change in soil volume occurs with loss of water, and this is called the zero shrinkage stage. In the case of a cohesive soil with high clay content, the initial shrinkage state is the most important one, and as a result we limit our desiccation model to that stage. An advantage of this approach is that the expansion/shrinkage coefficient and hydraulic conductivity can be considered constant through the first stage of desiccation since there is no significant loss of pore-water interconnectivity which can affect the system's hydraulic conductivity, and for the expansion/shrinkage coefficient, it will only depend on the soil's specific gravity and void ratio (see below).

Now we describe a desiccation pre-fracture model that can permit us to compute the evolution of soil parameters and resulting stresses in a restrained soil that is not allowed to strain until the stresses overcome the soil's strength.

C.5 The prefracture model and results

The total strain in the system can be thought of as a combination of elastic and hydric components acting in series.

$$\varepsilon_{ij} = \varepsilon_{ij}^e + \varepsilon_{ij}^h \quad (\text{C.1})$$

where e and h are the elastic and hydric components of the strain tensor. Note the absence of a thermal component since we are assuming an isothermal process for simplicity. The elastic component is related to stress σ by

$$\varepsilon_{ij}^e = \frac{1 + \nu}{E} \sigma_{ij} - \frac{\nu}{E} \sigma_{kk} \delta_{ij} \quad (\text{C.2})$$

where ν is Poisson's ratio, and E is Young's modulus. Due to natural symmetry of the ground, the second part of the equation will go away. Allowing E to be a function of

water content, the rate of elastic strain becomes

$$\dot{\epsilon}_{ij}^e = \frac{1 + \nu}{E} \dot{\sigma}_{ij} - \frac{1 + \nu}{E^2} \frac{\partial E}{\partial w} \dot{w} \sigma_{ij} \quad (C.3)$$

where w is the volumetric water content as a percentage of the total volume of the soil including the void volume ($\frac{V_{water}}{V_{soil}} \times 100$). Assuming the ground would expand and contact isotropically in response to changes in water content, we can express the hydric strain as

$$\epsilon_{ij}^h = \alpha(w - w_0) \delta_{ij} \quad (C.4)$$

where α is the hydric expansion coefficient that can be related to the void ratio e ($\frac{V_{void}}{V_{soil}}$) and specific gravity G_s of the soil in the following way

$$\alpha = \frac{G_s}{1 + e} \quad (C.5)$$

As discussed earlier, we can consider α constant in for the desiccation stage which we are interested in simulating. So, the rate of hydric strain is simply

$$\dot{\epsilon}_{ij}^h = \alpha \dot{w} \delta_{ij} \quad (C.6)$$

If we consider prefracture conditions where strain is zero, a principle coordinate system, and take into account the ground natural symmetry, we get

$$0 = \frac{1 + \nu}{E} \dot{\sigma} - \frac{1 + \nu}{E^2} \frac{\partial E}{\partial w} \dot{w} \sigma + \alpha \dot{w} \quad (C.7)$$

where $\sigma = \sigma_{11} = \sigma_{22}$, and $\sigma_{33} = 0$ neglecting overburden. In order to deduce E and its change with water content, we assume that water is lost only through diffusion. In that case, the water loss can be described by Fick's second diffusion law

$$\frac{dw}{dt} = D \frac{d^2 w}{dz^2} \quad (C.8)$$

here D is the diffusion constant in m^2/s , and we have assumed that diffusion is only in the vertical direction z to simulate a lowering of the water table or evaporation/deposition. Using Fick's law has certain limitation that will be discussed later in the text. If we assume uniform water content that only changes with depth due to overburden, then we can simply describe the water content in any given depth as

$$w(z) = w_0 \exp \frac{-z}{b} \quad (C.9)$$

where b is a scaling factor that equals 1070 m for Earth and 2800 m for Mars (Clifford 1993). A similar equation can be written to describe the change of diffusivity with depth which we assume changes in the same way that permeability does. However, this change is minimal if we consider depths less than 100 meters, so we can safely ignore it. As a result

$$\frac{d^2 w}{dz^2} = -\frac{1}{b} \quad (C.10)$$

Consequently,

Basic Properties of Werribee clay soil	
Specific gravity	2.66
Clay content (%)	62
Atterberg limits	
Liquid limit (%)	127
Plastic limit (%)	26
Plasticity index (%)	101
Linear shrinkage (%)	22
Mineralogy	
Quartz (%)	30
Feldspars (albite) (%)	8
Illiite (%)	10
Kaolinite (%)	10
Ca-smectite (%)	42

Figure C.1: Physical and chemical properties of Werribee clay as reported by Kodikara et al. (2004).

$$\frac{dw}{dt} = -\frac{D}{b} \tag{C.11}$$

and

$$w(t, z) = w_0(z) - \frac{tD}{b} \tag{C.12}$$

Now, we can use the water content to deduce E from the empirical equations in Amarasiri et al. (2010) for Werribee clay starting from a slurry (Kodikara et al. 2004). This soil is the residual clay of Quaternary basalt deposits found in Melbourne, Australia and contains significant amounts of smectites minerals, giving it high shrink-swell properties, and making it a good analog to work with. Basic properties of the Werribee clayey soil are given in Table C.1. From the empirical equations for this soil type, suction Ψ (in kPa) for any given water content can be calculated by

$$\Psi = \exp((136.5 - w)/9.92) \tag{C.13}$$

and from that we can estimate E using the equation

$$E = 24\Psi^{0.95}(1 - 2\nu) \tag{C.14}$$

Given all the necessary parameters using equation C. 8-C. 14, equation C. 7 can be solved using a 4th order Runge-Kutta method and integrated for 2 to 5 years, with time steps ranging from 3 to 5 days. It is worth noting that equation C. 7 is very similar to the final equation in Mellon (1997) for describing a prefracture model for thermal contraction polygons on Mars with two important differences: first, the thermal component in Mellon (1997) is replaced with the hydric part, with water content and shrinkage/expansion coefficient replacing temperature, and thermal expansion coefficient respectively. The other difference is the absence of a viscous creep component in our model. While stress relaxation through creep is believed to be significant for ice-rich soil with temperatures very close to the melting point of ice, this is not the case with our desiccation model where

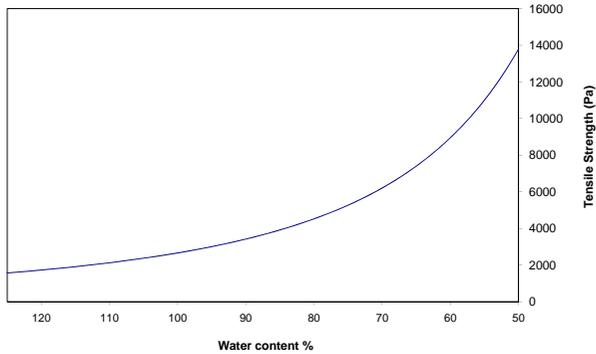


Figure C.2: Evolution of failure stress with disiccation for Werribee clay using the empirical equation given by Amarasiri et al. (2010).

the temperatures are way below the melting points of any of our soil components. As a result, we consider creep effects to be minimal even for a long term desiccation process. In addition, we investigate whether the resulting stresses are capable of inducing cracking using another empirical equation for computing the failure/tensile strength (in kPa) of the Werribee clay at different water contents which is given by Amarasiri et al. (2010, Figure C.2)

$$\sigma^F = 149,194w^{-2.3744} \quad (C.15)$$

Finally, the simulation starts near the liquid limit of the Werribee clay (125%) using the soil parameters listed in Table C.1, and is carried out for a range of diffusivities ranging from 10^{-6} to 10^4 . Some of the results are plotted in Figure C.3 for a range of the simulated diffusivities. As expected, the tensile stress in all cases is shown to rise monotonically with time. The stress at a given time varies logarithmically following the variation in diffusivities. It can be seen that while diffusivities below 10^{-4} are simply not capable of generating high enough stresses, values above 0.01 are too high thus leading to earlier and shallower cracks (i.e. smaller polygons). On the other hand, intermediate values between 10^{-2} and 10^{-3} create optimum conditions for the formation of cracks at the time scales suggested for the formation of giant desiccation polygons on Earth (Neal et al. 1968). In addition, the diffusivity range agrees excellently with measurements (2×10^{-2}) taken at hydrothermal lakes (Inferno Lake, New Zealand; Vandemeulebrouck et al. 2005), and clayey soils in general (Domenico and Schwartz 1998). Our next step is to extend the model to the crack initiation and propagation stage to model crack depths and size of polygons with different physical conditions and soil properties.

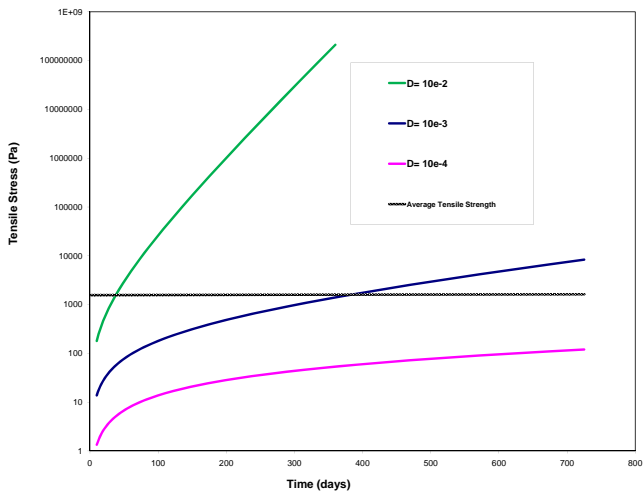


Figure C.3: Evolution of stress with time in a desiccating soil with different diffusivities. Intermediate values between 10^{-2} and 10^{-3} create optimum conditions for the formation of cracks at the time scales suggested for the formation of giant desiccation polygons on Earth.

D Used Image Dataset for Apollinaris Study

Image IDs	Central Lat.	Central Long.
CTX		
B01_010163_1712_XN_08S186W	-8	174
B05_011653_1714_XN_08S186W	-8	174
B07_012286_1730_XN_07S187W	-7	173
B08_012932_1703_XN_09S184W	-9	176
B09_013288_1724_XN_07S184W	-7	176
B12_014132_1721_XN_07S186W	-7	174
B12_014343_1737_XN_06S187W	-6	173
B12_014422_1688_XI_11S182W	-11	178
P02_001645_1726_XI_07S185W	-7	175
P02_001843_1716_XN_08S187W	-8	173
P02_001988_1709_XI_09S185W	-9	175
P04_002634_1707_XI_09S185W	-9	175
P06_003544_1703_XI_09S185W	-9	175
P08_003966_1721_XN_07S187W	-7	173
P10_004889_1704_XI_09S185W	-9	175
P11_005166_1695_XN_10S188W	-10	172
P12_005535_1732_XI_06S183W	-6	177
P13_006234_1664_XN_13S186W	-13	174
P15_007091_1668_XN_13S186W	-13	174
P16_007236_1754_XN_04S186W	-4	174
P16_007381_1694_XN_10S184W	-10	176
P18_007882_1703_XN_09S185W	-9	175
P18_008093_1661_XN_13S186W	-13	174
P22_009464_1693_XN_10S183W	-10	177
P22_009596_1706_XN_09S186W	-9	174
HiRISE		
ESP_017389_1690	-10.9	176
ESP_018167_1715	-8.3	174.8
PSP_001645_1725	-7.4	174.7

...continued on next page

Table D.1 – continued from previous page

Image IDs	Central Lat.	Central Long.
PSP_001988_1710	-9.1	174.7
PSP_002634_1725	-7.4	174.7
PSP_003966_1725	-7.3	172.5
PSP_004889_1705	-9.2	174.5
PSP_005100_1715	-8.5	173.2
PSP_006168_1705	-9.5	174.8
PSP_007671_1695	-10.5	176.4
PSP_008673_1710	-8.8	174.4
PSP_009464_1695	-10.2	176.4
PSP_009596_1705	-9.4	173.3
PSP_010163_1715	-8.5	173.9
PSP_010730_1715	-8.6	173.2
CRISM		
FRT000087B4	-9.4	172.4
FRT0000AD58	-8.7	174.4
FRT0000CB29	-8.4	173.8
HRL0000C68B	-8.4	173.8
HRL00003A0A	-9.1	174.7
HRL00008613	-9	174.6
HRL0000C01E	-9.3	173.3
HRS0000113D5	-9.6	172.6
HRS00008E7C	-9.6	172.7
MOC		
E0200496	-11.5	171.6
E0301324	-11.4	171.7
M0904224	-11.5	172.3
M1700504	-11	171.6
M2301786	-11.6	171.7
R1500299	-12.1	172.2
R1701282	-11.9	171.9
R2000613	-8.9	175.4
S0900611	-12.7	170.8
S1700362	-8.2	175.2

Bibliography

- Abramov , O. and D. A. Kring, 2005, Impact-induced hydrothermal activity on early Mars, *J. Geophys. Res.*, 110, E12S09, doi:10.1029/2005JE002453
- Allen C.C., 1979, Areal distribution of Martian rampart craters, *Icarus*, 39 (1), pp. 111-123
- Allen C.C., and D.Z. Oehler, 2008, A case for ancient springs in Arabia Terra, Mars. *Astrobiology*, vol. 8, num.6, p.1093
- Altheide, T. S., V. F. Chevri er, E. G. Rivera-Valentin, and J.J. Wray, 2009, Modeling the Stability of an Ancient Paleolake in Columbus Crater, Terra Sirenum, Mars. Workshop on Modeling Martian Hydrous Environments, held June 1-3, 2009 in Houston, Texas. LPI Contribution No. 1482, p.11-12
- Amarasiri A.L., Kodikara J.K., and Costa S., 2010, Numerical modeling of desiccation cracking, Numerical and Analytical methods in Geomechanics, DOI: 10.1002/nag.894
- Anderson, F., and S. Smrekar, 1999, Tectonic effects of climate change on Venus, *J. Geophys. Res.*, 104(E12), p. 30743-30756
- Anderson T. L., 2005, *Fracture Mechanics: Fundamentals and Applications*, 3rd edition. CRC Press
- Anderson, R.C., Dohm, J. M., Golombek, M.P., Haldemann, A., Franklin, B.J., Tanaka, K.L., Lias, J., Peer, B., 2001, Significant centers of tectonic activity through time for the western hemisphere of Mars, *J. Geophys. Res.* 106, p. 20,563-20,585
- Anderson, R.C., J.M. Dohm and 4 others 2008, Centers of tectonic activity in the eastern hemisphere of Mars. *Icarus*, doi:10.1016/j.icarus.2007.12.027
- Arvidson R.E., Carusi, A. Coradini, M. Fulchignoni, C. Federico, R. Funicello, and M. Salomone, 1976, Latitudinal variation of wind erosion of crater ejecta deposits on Mars, *Icarus*, 27, p. 503-516, doi:10.1016/0019-1035(76)90166-4
- Arvidson, R.E., and 62 colleagues, 2006, Overview of the Spirit Mars Exploration Rover Mission to Gusev Crater: Landing site to Backstay Rock in the Columbia Hills, *J. Geophys. Res.*, 111, E02S01, doi:10.1029/2005JE002499
- Arvidson, R.E., and 32 colleagues, 2008, Spirit Mars Rover Mission to the Columbia Hills, Gusev Crater: Mission overview and selected results from the Cumberland Ridge to Home Plate, *J. Geophys. Res.*, 113, E12S33, doi:10.1029/2008JE003183

- Arvidson, R. E., et al., 2010, Spirit Mars Rover Mission: Overview and selected results from the northern Home Plate Winter Haven to the side of Scamander crater, *J. Geophys. Res.*, 115, E00F03, doi:10.1029/2010JE003633
- Aydin, A., and J. M. DeGraff, 1988, Evolution of polygonal fracture patterns in lava flows, *Science*, 239, p. 471-476
- Baker V. R., 2001, Water and the martian landscape, *Nature* 412, 228-356
- Baker, V.R., and D.J. Milton, 1974, Erosion by catastrophic floods on Mars and Earth: *Icarus*, v. 23, p. 27-41
- Baker V.R., R.G. Strom, V.C. Gulick, J.S. Kargel, G. Komatsu, and V.S. Kale, 1991, Ancient oceans, ice sheets, and the hydrological cycle on Mars, *Nature*, 352, 589-594
- Baker, V.R., Strom, R.G., Dohm, J.M., Gulick, V.C., Kargel, J.S., Komatsu, G., Ori, G. G., Rice, J.W., 2000, Mars' Oceanus Borealis, ancient glaciers, and the MEGAOUTFLO hypothesis, 31st Lunar Planet. Sci. Conf., abstract no. 1863
- Bandfield, J. L., 2006, Extended surface exposures of granitoid compositions in Syrtis Major, Mars, *Geophys. Res. Lett.*, 33, L06203, doi:10.1029/2005GL025559
- Bandfield, J. L., 2008, High-silica deposits of an aqueous origin in western Hellas Basin, Mars, *Geophys. Res. Lett.*, 35, p. 12205, doi: 10.1029/2008GL033807
- Bandfield, J. L., Hamilton V.E., Christensen P.R., and McSween, H.Y., 2004, Identification of quartzofeldspathic materials on Mars, *J. Geophys. Res.*, 109, p. 10009
- Barlow N. G., Mars Global Database (version 1). Source: USGS Planetary GIS Web Server PIGWAD
- Barlow N. G., 1993, Depth-Diameter Ratios for Martian Impact Craters: Implications for Target Properties and Episodes of Degradations, Mars: Past, Present, and Future. Results from the MSATT Program, Part 1 p 1
- Barlow, N. G., 1995, The degradation of impact craters in Maja Valles and Arabia, Mars, *J. Geophys. Res.*, 100(E11), 23307-23316
- Barlow, N. G., 1998, Crater size-frequency distributions and a revised Martian relative chronology, *Icarus*, 75, p. 285-305, doi: 10.1016/0019-1035(88)90006-1
- Barlow, N. G., 2004, Martian subsurface volatile concentrations as a function of time: Clues from layered ejecta craters, *Geophys. Res. Lett.*, 31, L05703, doi:10.1029/2003GL019075
- Barlow, N.G., Bradley, T.L., 1990, Martian impact craters: Correlations of ejecta and interior morphologies with diameter, latitude, and terrain. *Icarus* 87, p. 156-179
- Barlow, N., J. Boyce, F. Costard, R. Craddock, J. Garvin, S. Sakimoto, R. Kuzmin, D. Roddy, and L. Soderblom, 2000, Standardizing the nomenclature of Martian impact crater ejecta morphologies, *J. Geophys. Res.*, 105(E11), 26733-26738

- Barlow, N. G., J. Koroshetz, and J. M. Dohm, 2001, Variations in the onset diameter for Martian layered ejecta morphologies and their implications for subsurface volatile reservoirs, *Geophys. Res. Lett.*, 28(16), p. 3095-3098, doi:10.1029/2000GL012804
- Barnhart C.J., Nimmo F., and Travis B.J., 2010, Martian post-impact hydrothermal systems incorporating freezing, *Icarus*, p. 101-117
- Bibring J.P et al., 2004, OMEGA: Observatoire pour la minéralogie, l'Eau, Les Glaces et l'Activité, In: *Mars Express: The scientific payload*. Ed., ESA Publications Division, p. 37-49
- Bibring J.P et al., 2005, Mars surface diversity as revealed by the OMEGA/Mars Express observations, *Science*, 307, p. 1576-1581
- Bibring J.P et al., 2006, Global Mineralogical and Aqueous Mars History Derived from OMEGA/Mars Express Data. *Science* 312, 400. DOI: 10.1126/science.1122659
- Bishop J.L., Murad E., Lane M.D., Mancinelli R.L., 2004, Multiple techniques for mineral identification on Mars: a study of hydrothermal rocks as potential analogues for astrobiology sites on Mars, *Icarus*, 169, p. 311-323, doi: 10.1016/j.icarus.2003.12.025
- Bleacher J.E., Wet A.P., Garry W.B., Zimbelman J.R., and Trumble M.E., (2010), Volcanic or fluvial: Comparison of an Ascræus Mons, Mars, braided and sinuous channel with features of the 1859 Mauna Loa flow and Mare Imbrium flows. 41st Lunar and Planetary Science Conference, abstract #1612
- Boisson, J., and 10 colleagues, 2009, Sounding the subsurface of Athabasca Valles using MARSIS radar data: Exploring the volcanic and fluvial hypotheses for the origin of the rafted plate terrain, *J. Geophys. Res.*, 114, E08003, doi:10.1029/2008JE003299
- Boynton, W.V., and 24 colleagues, 2002, Distribution of Hydrogen in the Near Surface of Mars: Evidence for Subsurface Ice Deposits, *Science* 297, p. 81-85
- Boynton, W.V., and 28 colleagues, 2004, The Mars Odyssey Gamma-Ray Spectrometer Instrument Suite: *Space Science Reviews*, v. 110, p. 37-83
- Boynton, W.V., and 27 colleagues, 2007, Concentration of H, Si, Cl, K, Fe, and Th in the low- and mid-latitude regions of Mars, *J. Geophys. Res.*, 112, 10.1029/2007JE002887
- Brown A.J., et al., 2010, Hydrothermal formation of Clay-Carbonate alteration assemblages in the Nili Fossae region of Mars, *E. & P.S.L.*, 297, p. 174-182
- Burnham C.W., 1979, *Magmas and Hydrothermal Fluids*, in *Geochemistry of hydrothermal deposits*, John Wiley & Sons, New York, p. 71-136
- Cabrol N. A., and E. Grin, 1999, Distribution, Classification, and Ages of Martian Impact Crater Lakes, *Icarus* 142, p. 160-172
- Cabrol N. A., E. A. Grin, H. E. Newsom, R. Landheim and C. P. McKay, 1999, Hydrogeologic evolution of Gale crater and its relevance to the exobiological exploration of Mars. *Icarus* 139, p. 235-245

- Cabrol N. A., and E. Grin, 2002, Overview on the formation of paleolakes and ponds on Mars, *Global and Planetary Change* 35, p. 199-219
- Campbell, B., L. Carter, R. Phillips, J. Plaut, N. Putzig, A. Safaeinili, R. Seu, D. Biccari, A. Egan, and R. Orosei, 2008, SHARAD radar sounding of the Vastitas Borealis Formation in Amazonis Planitia, *J. Geophys. Res.*, 113, E12010, doi:10.1029/2008JE003177
- Carr, M. H., 1979, Formation of Martian Flood Features by Release of Water From Confined Aquifers, *J. Geophys. Res.*, 84(B6), 2995-3007
- Carr M. H., 1983, Stability of streams and Lakes on Mars, *Icarus* 56, p. 476-495
- Carr, M.H., 1986, Mars: A water rich planet?, *Icarus* 68, p. 187-216
- Carr, M.H., 1996, *Water on Mars*, Oxford University Press, 248 pp
- Carr, M. H.; Crumpler, L. S.; Cutts, J. A.; Greeley, R.; Guest, J. E.; Masursky, H., 1977, Martian impact craters and emplacement of ejecta by surface flow, *J. Geophys. Research*, vol. 82, p. 4055-4065
- Carr M. H, S. S. Wu, R. Jordan, and F. J. Schafer, 1987, 18th Lunar and Planetary Science Conference, abstract, 155-156
- Carr, M. H., Head, J.W., 2009, Geologic history of Mars, *Earth Planet. Sci. Lett.*, doi: 10.1016/j.epsl.2009.06.042
- Carter L.M. and 11 colleagues, 2009, Shallow Radar (SHARAD) sounding observations of the Medusae Fossae Formation, Mars, *Icarus*, 199, p. 295-302
- Chapman M.G., and K.L. Tanka, 2001, Related magma-ice interactions: Possible origins of chasmata, chaos, and surface materials in Xanthe, Margaritifer, Meridiani Terrae, Mars. *Icarus*, 155 (2), pp. 324-339
- Chioni, R., Corazza, E., Marini, L., 1984, The gas/steam ratio as indicator of heat transfer at the Solfatara fumarole, Phlegrean Fields (Italy): *Bull. Volcanol.*, v. 47, p. 295-302
- Chong Diaz, G., Mendoza, M., Garcia-Veigas, J., Pueyo, J.J., Turner, P., 1999, Evolution and geochemical signatures in a Neogene forearc evaporitic basin: the Salar Grande (Central Andes of Chile): *Paleogeography, Paleoclimatology, Paleoecology*, v. 151, p. 39-54
- Christensen, P.R., and 10 colleagues, 2004a, The Thermal Emission Imaging System (THEMIS) for the Mars 2001 Odyssey mission. *Space Sci. Rev.* 101, p. 85-130
- Christensen, P.R., and 15 colleagues, 2004b, Detection of crystalline hematite mineralization on Mars by the Thermal Emission Spectrometer: Evidence for near-surface water, *J. Geophys. Res.*, 105, p. 9623-9642, doi: 10.1029/1999JE001093
- Christenson B.W., 2000, Geochemistry of fluids associated with the 1995/96 eruption of Mt. Ruapehu, New Zealand: signatures and processes in the magmatic-hydrothermal system, *J. Volcanol. Geotherm. Res.* 97 (2000), p. 1-30

- Christiansen E.H., 1989, Lahars in the Elysium region of Mars, *Geology* 17, p. 203-206
- Ciaramella, M., Napoli, A., Rossi, M., 2005, Another extreme genome: how to live at pH 0: *Trends in microbiology*, v. 13, p. 49-51
- Clifford, S. M., 1993, A Model for the Hydrologic and Climatic Behavior of Water on Mars, *J. Geophys. Res.*, 98(E6), 10,973-10,978, doi:10.1029/93JE00225
- Clifford, S. M. and T. J. Parker, 2001, The Evolution of the Martian Hydrosphere: Implications for the Fate of a Primordial Ocean and the Current State of the Northern Plains, *Icarus* 154, 40-79
- Corte A., and Higashi A., 1964, Experimental research on Desiccation cracks in Soil. CRREL Research report 66. U.S. Army Material Command, Hanover
- Costard, F. M., and Kargel, J. S., 1995, Outwash plains and thermokarst on Mars. *Icarus*, 114, p. 93-112
- Crown, D.A., Price, K.H., Greeley, R., 1992, Geologic evolution of the east rim of the Hellas basin, Mars: *Icarus*, v. 100, p. 1-25
- Davis P.A. and K.L. Tanaka, 1995, Curvilinear ridges in Isidis Planitia, Mars - The result of mud volcanism?, 14th Lunar and Planetary Science Conference abstract, p. 321-322
- Delmelle P., A. Bernard, M. Kusakabe, T. Fischer and B. Takano, 2000, Geochemistry of the magmatic-hydrothermal system of Kawah Ijen volcano, East Java, Indonesia, *J. Volcanol. Geotherm. Res.* 97, p. 31-53
- Di Achille, G., Hynek, B.M., 2010, Ancient ocean on Mars supported by global distribution of deltas and valleys: *Nature Geoscience*, v. 3, p. 459-463
- Di Achille, G., Marinangeli, L., Ori, G.G., Hauber, E., Gwinner, K., Reiss, D., and Neukum, G., 2006, Geological evolution of the Tyras Vallis paleolacustrine system, Mars: *J. Geophys. Res.*, v. 111, E04003, doi:10.1029/2005JE002561
- Dohm, J.M., 1995, Origin of Stoneman Lake, and volcano-tectonic relations of Mormon and San Francisco volcanic fields, Arizona: Thesis, Northern Arizona University, Flagstaff, Arizona, pp. 101
- Dohm, J.M., Anderson, R.C., Tanaka, K.L., 1998, Digital structural mapping of Mars: *Astron. & Geophys.*, v. 39, p. 3.20-3.22
- Dohm, J.M., Tanaka, K.L., Hare, T.M., 2001a, Geologic map of the Thaumasia region of Mars: US Geol. Survey Map I-2650
- Dohm, J.M., Ferris, J.C., Baker, V.R., Anderson, R.C., Hare, T.M., Strom, R.G., Barlow, N.G., Tanaka, K.L., Klemaszewski, J.E., Scott, D.H., 2001b, Ancient drainage basin of the Tharsis region, Mars: potential source for outflow channel systems and putative oceans or paleolakes: *J. Geophys. Res.*, v. 106, p. 32,942-32,958

Bibliography

- Dohm, J.M., Ferris, J.C., Barlow, N.G., Baker, V.R., Mahaney, W.C., Anderson, R.C., Hare, T.M., 2004, The Northwestern Slope Valleys (NSVs) region, Mars: A prime candidate site for the future exploration of Mars: *Planet. Space Sci.* v. 52, p. 189-198
- Dohm, J.M., et al., 2007, Possible ancient giant basin and related water enrichment in the Arabia Terra province, Mars: *Icarus*, v. 190, p. 74-92, doi: 10.1016/j.icarus.2007.03.006
- Dohm, J.M., and 21 others, 2008, Recent geological and hydrological activity on Mars: The Tharsis/Elysium Corridor: *Planet. Space Sci.*, v. 56, p. 985-1013
- Dohm, J.M., and 19 others, 2009a, GRS evidence and the possibility of ancient oceans on Mars, *Special Planet. & Space Sci.*, v. 57, p. 664-684
- Dohm and 15 other authors, 2009b, New evidence for a magmatic influence on the origin of Valles Marineris, Mars: *J. Volcanol. Geotherm. Res.* 185, p. 12-27
- Dohm and 13 other authors, 2009c, Claritas rise: Pre-Tharsis magmatism, *Journal of Volcanology and Geothermal Research*, v. 185, p. 139-156
- Dominico P.A., and Schwartz F.W., 1998, *Physical and Chemical Hydrogeology*, second edition, John Wiley & Sons Inc., 506 pp
- Dundas C.M. and A.S. McKewen, 2010, An assessment of evidence for pingos on Mars using HiRISE, *Icarus* 205, 244-258
- Ehlmann, B. H., et al., 2008a, Orbital Identification of Carbonate-bearing Rocks on Mars, *Science* 322, 1828, DOI: 10.1126/science.1164759
- Ehlmann, B. H., et al., 2008b, Clay minerals in delta deposits and organic preservation potential on Mars, *Nature Geoscience* 1, p. 355-358
- Ehlmann, B. L., and 11 colleagues, 2009, Identification of hydrated silicate minerals on Mars using MRO-CRISM: Geologic context near Nili Fossae and implications for aqueous alteration, *J. Geophys. Res.*, 114, E00D08, doi:10.1029/2009JE003339
- El Maarry M.R., and Gasnault O., 2009, A Preliminary Assessment of the Role of Impact Craters in Forming Hydrous Minerals on the Surface of Mars. 40th Lunar and Planetary Science Conference, abstract no. 1883
- El Maarry M.R., Gasnault O., Toplis M., Baratoux D., Dohm J. M., Newsom H. E., Boynton W. V., Karunatillake S., 2009, Chemical composition of Martian volcanics at Tharsis from gamma-ray data: New constraints on the depth of the mantle source region, *J. Volcanol. Geotherm. Res.* 185, p. 116-122
- El Maarry M.R., Markiewicz W.J., Mellon M., Goetz., Dohm J., and Pack A., 2010, Crater Floor Polygons : Desiccation Patterns of Ancient Lakes on Mars?, *J. Geophys. Res.*, doi:10.1029/2010JE003609
- Evans L.G., et al., 2008, Detection of Additional Elements from the Mars Odyssey GRS Measurements, 39th Lunar and Planetary Science Conference abstract no. 1391

- Fairén, A.G., Dohm, J.M., Baker, V.R., de Pablo, M.A., Ruiz, J., Ferris, J.C., Anderson, R.C., 2003, Episodic flood inundations of the northern plains of Mars: *Icarus*, v. 165, p. 53-67
- Fairén, A.G., Dohm, J.M., Uceda, E.R., Rodríguez, A., Baker, V.R., Fernández-Remolar, D., Schulze-Makuch, D., Amils, R., 2005, Prime candidate sites for astrobiological exploration through the hydrogeological history of Mars: *Planet. Space Sci.* 53, p. 1355-1375
- Fairén, A.G., Chevrier, V., Abramov, O., Marzo, G.A., Gavin, P., Davila, A.F., Tornabene, L.L., Bishop, J.L., Roush, T.L., Gross, C., Kneissl, T., Uceda, E.R., Dohm, J.M., Schulze-Makuch, D., Rodriguez, J.A.P., Amils, R., McKay, C.P. (2010-accepted) Noachian and more recent phyllosilicates in impact craters on Mars. *PNAS* 107, I2095-I2100
- Farmer, J.D., 1996, Hydrothermal systems on Mars: An assessment of present evidence. In *Evolution of Hydrothermal Systems on Earth (and Mars?)*, Ciba Found. Symp., Wiley, Chichester, p. 273-299
- Farmer, J.D., 2000, Hydrothermal systems: doorways to early biosphere evolution: *GSA Today*, v. 10, p. 1-9
- Farrand, W. H., L. R. Gaddis, and L. Keszthelyi, 2005, Pitted cones and domes on Mars: Observations in Acidalia Planitia and Cydonia Mensae using MOC, THEMIS, and TES data, *J. Geophys. Res.*, 110, E05005, doi:10.1029/2004JE002297
- Fassett, C. I., and J. W. Head III, 2005, Fluvial sedimentary deposits on Mars: Ancient deltas in a crater lake in the Nili Fossae region, *Geophys. Res. Lett.*, 32, L14201, doi:10.1029/2005GL023456
- Feldman W.C., and 12 colleagues, 2002, Global Distribution of Neutrons from Mars: Results from Mars Odyssey, *Science* 297, p. 75-78
- Ferguson, R. L., P. R. Christensen, and H. H. Kieffer, 2006, High-resolution thermal inertia derived from the Thermal Emission Imaging System (THEMIS): Thermal model and applications, *J. Geophys. Res.*, 111, E12004, doi:10.1029/2006JE002735
- Flores, G., Liu, Y., Ferrera, I., Beveridge, T.J., and Reysenbach, A.L., 2008, *Sulfurihydrogenibium kristjanssoni* sp. nov., a hydrogen and sulfur-oxidizing thermophile isolated from a terrestrial Icelandic hot spring: *Int. J. Syst. Evol. Micro.*, v. 58, p. 1153-1158
- Forsythe, R. D., and C. R. Blackwelder, 1998, Closed drainage crater basins of the Martian highlands: Constraints on the early Martian hydrologic cycle, *J. Geophys. Res.*, 103(E13), p. 31,421-31,431
- Friedman, J. D., C. E. Johansson, N. Oskarsson, H. Svenson, S. Thorarinnsson, and R. S. Williams, 1971, Observations on Icelandic Polygon Surfaces and Palsa Areas. *Photo Interpretation and Field Studies*, Geografiska Annaler, Vol. 53, Ser A, 115-145

Bibliography

- Furfaro, R., et al., 2008, The search for life beyond Earth through fuzzy expert systems, *Planet. & Space Sci.*, v. 56, p. 448-472
- Futterer et al., 2004, Genome sequence of *Picrophilus torridus* and its implications for life around pH 0: *Proc. Natl. Acad. Sci. U. S. A.*, v. 101, p. 9091-9096
- Gellert, R., 14 colleagues, 2004, Chemistry of Rocks and Soils in Gusev Crater from the Alpha Particle X-ray Spectrometer: *Science*, v. 305, p. 829-832
- Gendrin A. et al., 2005, Sulfates in Martian layered terrains: the OMEGA/Mars Express view, *Science*, 307, p. 1587-1591
- Ghail R. C. And Hutchison J. E., 2003, An alluvial fan at Apollinaris, Mars, 34th Lunar and Planetary Science Meeting, abstract no. 1775
- Glamoclija, M., Garrel, L., Berthon, J., Lopez-Garcia, P., 2004, Biosignatures and bacterial diversity in hydrothermal deposits of Solfatara Crater, Italy: *Geomicrobio. Jour.*, v. 21, p. 529-541
- Gold L. W., 1958, Some observations of the dependence of strain in stress for ice. *Can. J. Phys.*, 36, p. 1265-1275
- Gooding J.L., 1992, Soil mineralogy and chemistry on Mars - Possible clues from salts and clays in SNC meteorites, *Icarus*, 99, no. 1, p. 28-41
- Goorissen, H.P., Boschker, H.T.S., Stams, A.J.M., and Hansen, T.A., 2003, Isolation of thermophilic *Desulfotomaculum* strains with methanol and sulfite from solfataric mud pools, and characterization of *Desulfotomaculum solfataricum* sp. Nov: *Int. J. Sys. Evol. Microbiol.*, v. 53, p.1223-1229
- Greeley, R., F. H. Bernard, H. Y. McSween, G. Neukum, P. Pinet, M. van Kan, S. C. Werner, D. A. Williams, and T. E. Zegers, 2005, Fluid lava flows in Gusev crater, Mars, *J. Geophys. Res.*, 110, E05008, doi:10.1029/2005JE002401
- Grin E. A. and N. A. Cabrol, 1997, Limnologic analysis of Gusev crater paleolake, Mars, *Icarus* 130, 461-474
- Grizzaffi, Patricia, and Schultz, P.H., 1989, Isidis basin: site of ancient volatile-rich debris layer, *Icarus*, 77, p. 358-381
- Grossenbacher K.A. and McDuffie S.M., 1995, Conductive cooling of lava: columnar joint diameter and stria width as functions of cooling rate and thermal gradient, *J. Volc. Geo. Res.* 69, p. 95-103
- Gulick, V.C., 1998, Magmatic intrusions and a hydrothermal origin for fluvial valleys on Mars, *J. Geophys. Res.*, 103(E8), p. 19365-19387
- Gulick V.C., 2001, Origin of the valley networks on Mars: a hydrological perspective, *Geomorphology*, 37, p. 241-268

- Gulick, V., and V. Baker, 1989, Fluvial valleys and Martian paleoclimates, *Nature*, 341, p. 514-516
- Gulick, V., and V. Baker, 1990, Origin and Evolution of Valleys on Martian Volcanoes, *J. Geophys. Res.*, 95(B9), p. 14325-14344
- Haberle R. M., C.P. McKay, J. Schaeffer, M. Joshi, N.A. Cabrol and E.A. Grin, 2000, Meteorological control on the formation of paleolakes on Mars. 31st Lunar and Planetary Science Conference, abstract no. 1509
- Hagerty J.J. and Newsom H.E., 2003, Hydrothermal alteration at the Lomar Lake impact structure, India: Implications for impact cratering on Mars, *Meteoritics and Planetary Science*, 38, p. 365-381, doi: 10.1111/j.1945-5100.2003.tb00272.x
- Hahn, B. C., and 12 colleagues, 2007, Mars Odyssey Gamma Ray Spectrometer elemental abundances and apparent relative surface age: Implications for Martian crustal evolution, *J. Geophys. Res.*, 112, E03S11, doi:10.1029/2006JE002821
- Hapke, B., 1981, Bidirectional reflectance spectroscopy. 1. Theory, *J. Geophys. Res.* 86, p. 4571-4586
- Harris, A.C. and Golding, S.D., 2002, New evidence of magmatic-fluid-related phyllic alteration: Implications for the genesis of porphyry Cu deposits, *Geology* 30, n. 4, p. 335-338
- Harris R.C., 2004, Giant desiccation cracks in Arizona, *Arizona Geology*, vol. 34, n.2
- Hartmann, W. K., 2005, Martian cratering 8: Isochron refinement and the chronology of Mars, *Icarus*, 174, p. 294-320, doi:10.1016/j.icarus.2004.11.023
- Hartmann, W.K., and Neukum, G., 2001, Cratering chronology and the evolution of Mars: *Spa. Sci. Rev.*, v. 96, p. 165-194
- Hartmann W.K, Malin M., McEwen A., Carr M., Soderblom L., Thomas P., Danielson E., James P., and Vererka J., 1999, Evidence for recent volcanism on Mars from crater counts, *Nature*, 397, p. 586-589
- Head J.W., and Wilson L., 2002, Mars: A review and synthesis of general environments and geological settings of magma-water interactions, *Geol. Soc. Lond. Spec. Publ.* 202, p. 27-57
- Hock, A.N., Cabrol, N.A., Dohm, J.M., and 24 others, 2007, Scoring system for habitability and the robotic exploration for life: *J. Geophys. Res.*, v. 112, G04S08
- Hodges, C.A., Moore, H.J., 1994, Atlas of Volcanic Landforms on Mars: U.S. Geol. Surv. Prof. Pap. 1534, 194 pp
- Hoefen T. M. , Clark R.N., Bandfield J.L., Smith M.D., Pearl J.C., and Christensen P.R., 2003, Discovery of Olivine in the Nili Fossae Region of Mars, *Science* 302, 627, doi: 10.1126/science.1089647

- Holm, R.F., 2001, Cenozoic paleogeography of the central Mogollon Rim-southern Colorado Plateau region, Arizona, revealed by Tertiary gravel deposits, Oligocene to Pleistocene lava flows, and incised streams: *GSA Bull.*, v. 113, p. 1467-1485
- Holt, J. W., D. D. Blankenship, D. L. Morse, D. A. Young, M. E. Peters, S. D. Kempf, T. G. Richter, D. G. Vaughan, and H. F. J. Corr, 2006, New boundary conditions for the West Antarctic Ice Sheet: Subglacial topography of the Thwaites and Smith glacier catchments, *Geophys. Res. Lett.*, 33, L09502, doi:10.1029/2005GL025561
- Hood L.L., Keith P. Harrison, Benoit Langlais, Robert J. Lillis, Francois Poulet, David A. Williams, 2010, Magnetic anomalies near Apollinaris Patera and the Medusae Fossae Formation in Lucus Planum, Mars. *Icarus*, 208, p. 118-131
- Hu L.B., Péron H., Hueckel T., and Laloui L., 2006, Numerical and phenomenological study of desiccation of soil. *ASCE Geotechnical Special Publication: Advances in unsaturated soil, seepage and environmentals*, 2006, p. 166-173
- Hynek, B. M., R. E. Arvidson, and R. J. Phillips, 2002, Geologic setting and origin of Terra Meridiani hematite deposit on Mars, , 107, 5088, doi:10.1029/2002JE001891
- Jaeger W.L., L.P. Keszthelyi, A.S. McEwen, C.M. Dundas and P.S. Russel, 2007, HiRISE observations of Athabasca Valles, Mars: A lava-draped channel system, *Science* 317 (2007), p. 1709-1711
- Jakosky B.M., and Jones J.H., 1994, Evolution of water on Mars, *Nature*, 370, p. 328-329
- Kargel, J.S., 2004, Mars: A Warmer Wetter Planet, 557 pages, Praxis-Springer
- Kargel, J.S., Strom, R.G., 1992, Ancient glaciation on Mars: *Geology*, v. 20, p. 3-7
- Karunatillake S., J. J. Wray, S. W. Squyres, G. J. Taylor, O. Gasnault, S. M. McLennan, W. Boynton, M.R. El Maarry, and J. M. Dohm, 2009, Chemically striking regions on Mars and Stealth revisited, *J. Geophys. Res.*, 114, E12001
- Keller, J. M., 17 colleagues, 2006, Equatorial and midlatitude distribution of chlorine measured by Mars Odyssey GRS: *J. Geophys. Res.*, v. 111, E03S08, doi:10.1029/2006JE002679
- Kerber L., and Head J.W., 2010, The age of the Medusae Fossae Formation: Evidence of Hesperian emplacement from crater morphology, stratigraphy, and ancient lava contacts. *Icarus* 206, 669-684
- Kieffer S.W. and Simonds C.H., 1980, The role of volatiles and lithology in the impact cratering process, *Reviews in Geophysics and Space Physics*, 18, p. 443-481
- Kilgour G., V. Manville, F. Della Pasqua, A. Graettinger, K.A. Hodgson and G.E. Jolly, 2010, The 25 September 2007 eruption of Mount Ruapehu, New Zealand: directed ballistics, surtseyan jets, and ice-slurry lahars, *J. Volcanol. Geotherm. Res.* 191, p. 1-14
- Kodikara J.K., Nahlawi H., and Bouazza A., 2004, Modeling of curling in desiccating clay, *Canadian Geotechnical J.*, 41, 560-566

- Komatsu G., G. D. Achille, C. Popa, S. D. Lorenzo, A. P. Rossi, and J. P. Rodriguez, 2009, Paleolakes, paleofloods, and depressions in Aurorae and Ophir Plana, Mars: Connectivity of surface and subsurface hydrological systems, *Icarus* 201, 474-491
- Komatsu G., Ori G.G., Cardinale M., Dohm J., Baker V.R., Vaz D.A., Ishimaru R., Namiki N., and Matsui T., 2010, Roles of methane and carbon dioxide in geological processes on Mars, *Icarus*, in press
- Komor, S.C., Valley J.W., and Brown, P.E., 1988, Fluid-inclusion evidence for impact heating at the Siljan Ring, Sweden, *Geology* 16, p. 711
- Konrad J.M., and Ayad R., 1997, An idealized framework for the analysis of cohesive soils undergoing desiccation, *Canadian Geotechnic J.*, 34, p. 477-488
- Kuzmin R. O., and Zabalueva E. V., 2003, Polygonal Terrains on Mars: Preliminary Results of Global Mapping of their Spatial Distribution, LPSC XXXIV, abstract no. 1912
- Lachenbruch A. H., 1961, Depth and Spacing of Tension Cracks. *J. Geophys. Res.* 66(12), p. 4273-4292
- Lachenbruch A. H., 1962, Mechanics of Thermal Contraction Cracks and Ice-Wedge Polygons in Permafrost, Spec. Pap. Geological society of America, 70, 69 pp
- Lang , N. P., H. Y. McSween, L. L. Tornabene, C. J. Hardgrove, and P. R. Christensen, 2010, Reexamining the relationship between Apollinaris Patera and the basalts of the Gusev crater plains, Mars, *J. Geophys. Res.*, 115, E04006, doi:10.1029/2009JE003397
- Langevin Y., Poulet F., Bibring J.P. and Gondet B., 2005, Sulfates in the north polar regions of Mars detected by OMEGA/Mars Express, *Science*, 307, p. 1584-1586
- Langlais B., and M. Purucker, 2007, A polar magnetic paleopole associated with Apollinaris Patera, Mars, *Planet. Space Sci.* 55, p. 270-279
- Leverington, D. W., 2004, Volcanic rilles, streamlined islands, and the origin of outflow channels on Mars, *J. Geophys. Res.*, 109, E10011, doi:10.1029/2004JE002311
- Lerouge C., A. Kunov, C. Fléhoc, S. Georgieva, A. Hikov, J.L. Lescuyer, R. Petrunov and N. Velinova, 2006, Constraints of stable isotopes on the origin of alunite from advanced argillic alteration systems in Bulgaria, *Journal of Geochemical Exploration*, vol. 90, n. 3, p. 166-182
- Levy, J., J. Head, and D. Marchant, 2009, Thermal contraction crack polygons on Mars: Classification, distribution, and climate implications from HiRISE observations, *J. Geophys. Res.*, 114, E01007, doi:10.1029/2008JE003273
- Limonov A.F., J. Woodside, M. Cita and M. Ivanov, 1996, The Mediterranean Ridge and related mud diapirism, a background. *Mar. Geol.* 132, p. 7-19

Bibliography

- Loope D.B., and Haverland Z.E., 1988, Giant desiccation fissures filled with calcareous eolian sand, Hermosa Formation (Pennsylvanian), southern Utah. *Sedimentary Geology*, 56, p. 403-413
- Lucchitta, B.K., 1981, Mars and Earth: comparison of cold-climate features, *Icarus*, 45, p. 264-303
- Lucchitta B. K., 1983, Permafrost on Mars: Polygonally fractures ground, in *Permafrost: Fourth International Conference Proceedings*, Natl. Acad. Press, Washington, D. C.
- Mackay, J. R., 1966, Pingos in Canada, *Permafrost International Conference, Proceedings*. National Research Council, vol. 1287. National Academy of Science, Ottawa, Canada, p. 71-76
- Mahaney, W.C., Milner, M.W., Netoff, D., Malloch, D., Dohm, J.M., Baker, V. R., Miyamoto, Hideaki, Hare, T.M., and Komatsu, G., 2004, Ancient wet Aeolian environments on Earth: clues to presence of fossil/live microorganisms on Mars, *Icarus*, 171, p. 39-53
- Mahaney, W., H. Miyamoto, J.M. Dohm, and 4 others, 2007, Rock glaciers on Mars: Earth-based clues to Mars' recent paleoclimatic history: *Planetary and Space Sciences*, v. 55, p. 181-192
- Major J.J., and Newhall C.G., 1989, Snow and ice perturbation during historical volcanic eruptions and the formation of lahars and floods. *Bulletin of Volcanology* 52, p. 1-27
- Malin, M.C., 1979, Mars: evidence of indurated deposits of fine materials, *NASA Conf. Pub.* 2072, 54 pp
- Malin, M., G. Danielson, A. Ingersoll, H. Masursky, J. Veverka, M. Ravine, and T. Soulanille, 1992, Mars Observer Camera, *J. Geophys. Res.*, 97(E5), 7699-7718
- Malin, M. C., and M. H. Carr, 1999, Groundwater formation of martian valleys, *Nature* 397, p. 589-591
- Malin, M.C., and K.S. Edgett, 2001, Mars Global Surveyor Mars Orbiter Camera: Interplanetary cruise through primary mission: *J. Geophys. Res.*, v. 106, p. 23,429-23,570
- Malin, M.C., and Edgett, K.S., 2003, Evidence for persistent flow and aqueous sedimentation on Mars: *Science*, v. 302, p. 1931-1934, doi:10.1126/science.1090544
- Malin, M., G. Danielson, A. Ingersoll, H. Masursky, J. Veverka, M. Ravine, and T. Soulanille, 1992, Mars Observer Camera, *J. Geophys. Res.*, 97(E5), p. 7699-7718
- Malin, M.C., and 13 colleagues, 2007, Context Camera investigation on board the Mars Reconnaissance Orbiter. *J. Geophys. Res.* 112, E05S04
- Maloolf, A. C., J. B. Kellogg, and A. M. Anders, 2002, Neoproterozoic sand wedges: Crack formation in frozen soils under diurnal forcing during a snowball Earth, *Earth Planet. Sci. Lett.*, 204, 1-15, doi:10.1016/S0012-821X (02)00960-3

- Mangold N., 2005, High latitude patterned grounds on Mars: Classification, distribution and climatic control. *Icarus* 174, p. 336-359, doi:10.1016/j.icarus.2004.07.030
- Mangold, N., et al., 2007, Mineralogy of the Nili Fossae region with OMEGA/Mars Express data: 2. Aqueous alteration of the crust, *J. Geophys. Res.*, 112, E08S04, doi:10.1029/2006JE002835
- Mangold N., Roach L., Milliken R., Le Mouelic S., Ansan V., Bibring J.P., Masson P., Mustard J.F., Murchie S., Neukum G., 2010, A late Amazonian alteration layer related to local volcanism on Mars, *Icarus*, Volume 207, Issue 1, p. 265-276
- Marzo G. A., T. L. Roush, S. Fonti, V. Orofino, and A. Blanco (2009). Evidence Of Water-related Minerals In Putative Paleolakes On Mars As Seen By MRO/CRISM. *American Astronomical Society*, 41st DPS meeting, no. 35.09
- Marzo, G.A. et al., 2010, Evidence for Hesperian impact-induced hydrothermalism on Mars. *Icarus*, doi:10.1016/j.icarus.2010.03.013
- Masursky, H., 1973, An Overview of Geological Results from Mariner 9, *J. Geophys. Res.*, 78(20), p. 4009-4030
- McCauley, J., 1973, Mariner 9 Evidence for Wind Erosion in the Equatorial and Mid-Latitude Regions of Mars, *J. Geophys. Res.*, 78(20), p. 4123-4137
- McCubbin, F.M. and Nekvasil, H., 2008, Maskelynite-hosted apatite in the Chassigny meteorite: Insights into Late-stage magmatic volatile evolution in Martian magmas: *American Mineralogist*, v. 93, p. 676-684
- McCubbin F.M., Tosca N.J., Smirnov A., Nekvasil H., Steele A., Fries M., and Lindsley D.H., 2009, Hydrothermal jarosite and hematite in a pyroxene-hosted melt inclusions in Martian meteorite Miller Range (MIL) 03346: Implications for magmatic-hydrothermal fluids on Mars: *Geochimica et Cosmochimica Acta*, v. 73, p. 4907-4917
- McEwen, A.S., and 14 colleagues, 2007, Mars Reconnaissance Orbiter's High Resolution Imaging Science Experiment (HiRISE). *J. Geophys. Res.* 112, E05S02
- McGill G. E., and Hills L. S., 1992, Origin of Giant Martian Polygons. *J. Geophys. Res.*, 97, E2, p. 2633-2647
- McGuire, P.C., et al., 2009, An improvement to the volcano-scan algorithm for atmospheric correction of CRISM and OMEGA spectral data, *Planetary and Space Sci.*, 57, p. 809-815
- McKay C.P. and W.L. Davis, 1991, Duration of liquid water habitats on early Mars, *Icarus*, 90, p. 214-221
- McKay C.P., G. Clow, R. Wharton Jr. and S.W. Squyres, 1985, Thickness of ice on perennially frozen lakes, *Nature*, 313, p. 561-562

- McKinney, G. W., D. J. Lawrence, T. H. Prettyman, R. C. Elphic, W. C. Feldman, and J. J. Hagerty, 2006, MCNPX benchmark for cosmic ray interactions with the Moon, *J. Geophys. Res.*, 111, E06004, doi:10.1029/2005JE002551
- McLennan S.M., et al., 2010, Distribution of Sulfur of Mars Determined by the 2001 Mars Odyssey Gamma Ray Spectrometer, 42nd Lunar and Planetary Science Conference abstract no. 1533
- Melling, D. R., Watkinson, D. H., Fox, P. E. and Cameron, R. S., 1990, Carbonatization and propylitic alteration of fragmental basaltic rocks, Quesnel River gold deposit, Central British Columbia, *Mineralium Deposita* 25, issue 1, p. S115-S124
- Mellon M. T., 1997, Small-scale Polygonal features on Mars: Seasonal thermal contraction cracks in permafrost. *J. Geophys. Res.* 102, E11, p. 25,617-25,628
- Mellon M. T., and Jakosky B. M., 1993, Geographic variations in the thermal and diffusive stability of ground ice on Mars. *J. Geophys. Res.*, 98, p. 3345-3364
- Mellon, M. T., R. E. Arvidson, J. J. Marlow, R. J. Phillips, and E. Asphaug, 2008, Periglacial landforms at the Phoenix landing site and the northern plains of Mars, *J. Geophys. Res.*, 113, E00A23, doi: 10.1029/2007JE003039
- Melosh, H.J., 1989, *Impact Cratering: A Geologic Process*. Oxford University Press, 245 pp
- Messina P., P. Stoffer, and W.C. Smith, 2005, Macropolygon morphology, development, and classification on North Panamint and Eureka playas, Death Valley National Park CA. *Earth-Science Reviews*, 73, p. 309-322
- Milliken R. E., et al., 2008, Opaline silica in young deposits on Mars, *Geology*, 36, p. 847-850
- Molnár F., Watkinson D.H. and Everest J.O., 1999, Fluid-inclusion characteristics of hydrothermal Cu-Ni-PGE veins in granitic and metavolcanic rocks at the contact of the Little Stobie deposit, Sudbury, Canada, *Chemical Geology* 154, N. 1-4, p. 279-301
- Moore J. M., and D. E. Wilhelms, 2001, Hellas as a Possible Site of Ancient Ice-Covered Lakes on Mars, *Icarus*, 154, p. 258-276
- Morris R.V., et al., 2006, Mossbauer mineralogy of rock, soil and dust at Gusev crater, Mars: Spirit's journey through weakly altered olivine basalt on the plains and pervasively altered basalt in the Columbia Hills, *J. Geophys. Res.*, 111, doi: 10.1029/2005JE002584
- Mouginis-Mark, P., 1979, Martian Fluidized Crater Morphology: Variations With Crater Size, Latitude, Altitude, and Target Material, *J. Geophys. Res.*, 84(B14), p. 8011-8022
- Mouginis-Mark, P. J., 1987, Water or ice in the Martian regolith?: Clues from rampart craters seen at very high resolution, *Icarus*, 71(2), p. 268-286

- Mouginis-Mark, P.J., 1990, Recent water release in the Tharsis region of Mars: Icarus, v. 84, p. 362-373
- Mouginis-Mark P.J. and Rowland S.K., 2008, Lava flows at Arsia Mons, Mars: Insights from a graben imaged by HiRISE, Icarus, 198, p. 27-36
- Murchie, S., and 49 colleagues, 2007, Compact Reconnaissance Imaging Spectrometer for Mars (CRISM) on Mars Reconnaissance Orbiter (MRO). J. Geophys. Res. 112, E05S03
- Murchie, S.M., and 16 colleagues, 2009, A synthesis of Martian aqueous mineralogy after one Mars year of observations from the Mars Reconnaissance Orbiter, J. Geophys. Res., 114, E00D06, doi:10.1029/2009JE003342
- Mustard, J. F. and Hays, J. E., 1997, Effects of Hyperfine Particles on Reflectance Spectra from 0.3 to 25 μm , Icarus 125, p. 145-163
- Mustard, J.F., Poulet, F., Mangold, N., Bibring, J.-P., Milliken, R.E., Pelkey, S., 2006, Aqueous alteration and evidence of habitability in Nili Fossae: Abstract in: First Landing Site Workshop for the 2009 Mars Science Laboratory, May 31 - June 2, 2006, Pasadena, CA
- Mustard, J.F., and 35 colleagues, 2008, Hydrated silicate minerals on Mars observed by the Mars Reconnaissance Orbiter CRISM instrument. Nature 454, p. 305-309
- Mutch T. A., Arvidson R. E., Head J. W., Jones K. L., and Sainders R. S., 1976, The Geology of Mars, Princeton University Press, Princeton, NJ.
- Mutch T. A., Arvidson R. E., Binder A. B., Guinness E. A., and Morris E. C., 1977, The Geology of the Viking Lander 2 Site. J. Geophys. Res., 82, N.O. 28, p. 4452-4467
- Müller G., 1998, Starch columns: Analog model for basalt columns. J. Geophys. Res. 103, p. 15,239-15,253
- Nahalawi H., and Kodikara J.K., 2006, Laboratory experiments on desiccation cracking of thin soil layers. Geotechnical and Geological Engineering, 24, p. 1641-1664
- Nakagawa, S., Shtaih, Z., Banta, A., Beveridge, T.J., Sako, Y., and Reysenbach, A.-L., 2005, Sulfurihydrogenibium yellowstone sp. nov., an extremely thermophilic, facultatively heterotrophic, sulfur-oxidizing bacterium from Yellowstone National Park and amended descriptions of the genus Sulfurihydrogenibium, S. subterraneum, and S. azurensis: Int J Syst Evol Microbiol, v. 55, p. 2263-2268
- Naumov M., 2002, Impact-generated hydrothermal systems: Data from Popigai, Kara, and Puchezh-Katunki impact structures, In Impacts in Precambrian Shields, edited by Plado J. and Personen L.J., Springer, p. 117-172
- Naumov M.V., 2005, Principle features of impact-generated hydrothermal circulation systems: mineralogical and geochemical evidence, Geofluids, 5, p. 165-184

Bibliography

- Neal J. T., Langer A. M., Kerr P. F, 1968, Giant Desiccation Polygons of Great Basin Playas. *Geo. Soc. Amer. Bulletin*, V.79, p. 69-90
- Nealson, K.H., 1999, The search for extraterrestrial life: Engineering & Science, California Institute of Technology, LXII, p. 31-40
- Neumann, G. A., J. B. Abshire, O. Aharonson, J. B. Garvin, X. Sun, and M. T. Zuber, 2003, Mars Orbiter Laser Altimeter pulse width measurements and footprint-scale roughness, *Geophys. Res. Lett.*, 30, 1561, doi:10.1029/2003GL017048
- Newsom H.E., 1980, Hydrothermal alteration of impact melt sheets with implications to Mars, *Icarus* 44, p. 207-216
- Newsom, H.E., Sowards T., Keil K., and Graup G, 1986, Fluidization and hydrothermal alteration of the suevite deposit at the Ries Crater, West Germany, and implications for Mars, *J. Geophys. Res.*, 91, p. 239
- Newsom, H. E., G. E. Brittelle, C. A. Hibbitts, L. J. Crossey, and A. M. Kudo, 1996, Impact crater lakes on Mars, *J. Geophys. Res.*, 101(E6), 14,951-14,955, doi:10.1029/96JE01139
- Newsom H.E., Hagerty J.J., and Thorsos I.E., 2001, Location and sampling of aqueous and hydrothermal deposits in Martian impact craters. *Astrobiology* vol. 1, no. 1, p. 71
- Newsom H.E. and 11 colleagues, 2007, Geochemistry of Martian soil and bedrock in mantled and less mantled terrains with gamma ray data from Mars Odyssey, *J. Geophys. Res.*, 112E11, p. 3, DOI: 10.1029/2006JE002680
- Oberbeck V.R., 2009, Layered ejecta craters and the early water/ice aquifer on Mars, *Meteoritics and Planetary science*, Volume 44, p. 43-54
- Oehler D.Z., and C.C. Allen, 2010, Evidence for pervasive mud volcanism in Acidalia Planitia, Mars. *Icarus* 208, p. 636-657
- O'Neill, A.H., Liu, Y., Ferrera, I., Beveridge, T.J., and Reysenbach, A.-L., 2008, *Sulfurihydrogenibium rodmanii* sp. nov., a sulfur-oxidizing chemolithoautotroph from the Uzon Caldera, Kamchatka Peninsula, Russia, and emended description of the genus *Sulfurihydrogenibium*: *Int J Syst Evol Microbiol*, v. 58, p. 1147-1152
- Ori, G.G., Marinangeli, L., and Baliva, A., 2000a, Terraces and Gilbert-type deltas in crater lakes in Ismenius Lacus and Memnonia (Mars): *J. Geophys. Res.*, v. 105, p. 17,629-17,642.
- Ori, G.G., Marinangeli, L., Komatsu, G., 2000b, Gas (methane?)-related features on the surface of Mars and subsurface reservoirs: 31st Lunar Planetary Science Conference, abstract no. 1550
- Osterloo M. M., Hamilton V.E. , Bandfield J.L., Glotch T.D., Baldrige A.M., Christensen P.R., Tornabene L.L., and Anderson F.S., 2008, Chloride-bearing materials in the southern highlands of Mars. *Science* 319, 1651; DOI: 10.1126/science.1150690

- Osterloo M. M., Anderson F.S., Hamilton V.E., and Hynes B.M., 2010, Geologic context of proposed chloride-bearing materials on Mars, *J. Geophys. Res.*, 115, E14, p. 10012, doi: 10.1029/2010JE003613
- de Pablo M. A., and G. Komatsu, 2009, Possible pingo fields in the Utopia basin, Mars: Geological and climatical implications, *Icarus*, 199, p. 49-74
- Parente, M., 2008, A new approach to denoising CRISM images, 39th Lunar and Planetary Science Conference, Abstract no. 2528
- Parker A. P., 1999, Stability of arrays of multiple edge cracks, *Engineering Fracture Mechanics*, Volume 62, Issue 6, p. 577-591
- Parker, T. J., D. S. Gorsline, R. S. Saunders, D. C. Pieri, and D. M. Schneeberger, 1993, Coastal Geomorphology of the Martian Northern Plains, *J. Geophys. Res.*, 98(E6), p. 11,061-11,078
- Parnell, J., Boyce, A., Thackrey, S., Muirhead, D., Lindgren, P., Mason, C., Taylor, C., Still, J., Bowden, S., Osinski, G. & Lee, P., 2010, Sulfur isotope signatures for rapid colonization of an impact crater by thermophilic microbes: *Geology*, v. 38, p. 271-274
- Pechmann J. C., 1980, The origin of Polygonal Troughs on the Northern Plains of Mars, *Icarus*, 42, p. 185-210
- Pelkey, S.M., et al., 2007, CRISM multispectral summary products: Parameterizing mineral diversity on Mars from reflectance, *J. Geophys. Res.*, 112, E08S14, doi:10.1029/2006JE002831
- Peron H., Delenne J.Y., Laloui L., and El Youssoufi M.S., 2009a, Discrete element modeling of drying shrinkage and cracking of soils. *Computers and Geotechnics*, 36, p. 61-69
- Peron H., Hueckel T., Laloui L., and Hu L.B., 2009b, Fundamentals of desiccation cracking of fine-grained soil: experimental characterization and mechanisms identification. *Canadian Geotechnic J.* 46, p. 1177-1201
- Piatek, J. L., et al., 2007, Surface and subsurface composition of the Life in the Atacama field sites from rover data and orbital image analysis, *J. Geophys. Res.*, 112, G04S04, doi:10.1029/2006JG000317
- Picardi G., and 33 colleagues, 2005, Radar Soundings of the Subsurface of Mars, *Science*, 310, p. 1925-1928, doi: 10.1126/science.1122165
- Pirajno, F., 2009, *Hydrothermal Processes and Mineral Systems*, Springer, 1250 pp
- Plaut J.J. and 23 colleagues, 2007, Subsurface Radar Sounding of the South Polar Layered Deposits of Mars, *Science*, 316, p. 92-95, doi: 10.1126/science.1139672
- Plaut, J. J., A. Safaeinili, J. W. Holt, R. J. Phillips, J. W. Head, R. Seu, N. E. Putzig, and A. Frigeri, 2009, Radar evidence for ice in lobate debris aprons in the mid-northern latitudes of Mars, *Geophys. Res. Lett.*, 36, L02203, doi:10.1029/2008GL036379

- Pondrelli, M., A. Baliva, S. Di Lorenzo, L. Marinangeli, and A. P. Rossi, 2005, Complex evolution of paleolacustrine systems on Mars: An example from the Holden crater, *J. Geophys. Res.*, 110, E04016, doi:10.1029/2004JE002335
- Pondrelli, M., Rossi, A.P., Marinangeli, L., Hauber, E., Gwinner, K., Baliva, A., di Lorenzo, S., 2008, Evolution and depositional environments of the Eberswalde fan delta, Mars: *Icarus*, v. 197, p. 429-451
- Poulet F., and 8 colleagues, 2005, Phyllosilicates on Mars and implications for early martian climate, *Nature* 438, p. 623-627
- Putzig N.E., Mellon M.T., Kretke K.A., and Arvidson R.E., 2005, Global thermal inertia and surface properties of Mars from the MGS mapping mission, *Icarus*, 173, p. 325-341, doi: 10.1016/j.icarus.2004.08.017
- Rathbun, J.A., and Squyres, S.W., 2002, Hydrothermal systems associated with Martian impact craters: *Icarus*, v. 157, p. 362-372
- Reed M.H., 1997, Hydrothermal Alteration and its Relation to Ore Fluid Composition, In Barnes H.L. (ed) geochemistry of hydrothermal ore deposits, 3rd edn., John Wiley & Sons, p. 303-366
- Requia K. and Fontboté L., 1999, Hydrothermal alkali metasomatism in the Salobo iron oxide Cu (-Au) deposit, Carajas mineral province, northern Brazil, In Stanley, C.J., et al., eds., *Mineral deposits: Processes to processing*: Rotterdam, Balkema, p. 1025-1028
- Reynolds, T. J. and Beane, R. E., 1985, Evolution of hydrothermal fluid characteristics at the Santa Rita, New Mexico, porphyry copper deposit, *Economic Geology* 80, n.5, p. 1328-1347, doi:10.2113/econgeo.80.5.1328
- Rowe G.L., S.L. Brantley, M. Fernandez, J.F. Fernandez, A. Borgia and J. Barquero, 1992, Fluid-volcano interaction in an active stratovolcano: the volcanic lake system of Poás Volcano, Costa Rica, *J. Volcanol. Geotherm. Res.* 49, p. 23-51
- Robinson, M. S., P. J. Mouginis-Mark, J. R. Zimbelman, S. S. C. Wu, K. K. Ablin, and A. E. Howington-Kraus, 1993, Chronology, eruption duration, and atmospheric contribution of the Martian volcano Apollinaris Patera, *Icarus*, 104, p. 301-323
- Rodriguez, J.A.P., Sasaki, S., Kuzmin, R.O., Dohm, J.M., Tanaka, K.L., Miyamoto, H., Kurita, K., Komatsu, G., Fairen, A.G., Ferris, J.C., 2005, Outflow channel sources, reactivation, and chaos formation, Xanthe Terra, Mars: *Icarus*, v. 175, p. 36-57
- Romanek C.S. et al., 1994, Record of fluid-rock interactions on Mars from the meteorite ALH84001, *Nature*, 372, p. 655-657
- Rossbacher, L.A., and Judson, S., 1981. Ground ice on Mars: inventory, distribution, and resulting landforms, *Icarus*, 45, p. 39-59
- Rudolph M. L., 2009, Fracture penetration in planetary ice shells. *Icarus*, 199, p. 536-541

- Russell, P. S., and J. W. Head, 2003, Elysium-Utopia flows as mega-lahars: A model of dike intrusion, cryosphere cracking, and water-sediment release, *J. Geophys. Res.*, 108(E6), 5064, doi:10.1029/2002JE001995
- Schmidt, M.E., Ruff, S.W., McCoy, T.J., Farrand, W.H., Johnson, J.R., Gellert, R., Ming, D.W., Morris, R.V., Cabrol, N., Lewis, K.W., Schroeder, C., 2008, Hydrothermal origin of halogens at Home Plate, Gusev Crater: *J. Geophys. Res.*, v. 113, E06S12, doi:10.1029/2007JE003027
- Schrenk, M.O., Huber, J.A., and Edwards, K.J., 2010, Microbial provinces in the sub-seafloor: *Ann. Rev. Mar. Sci.*, v. 2, p. 279-304
- Schulze-Makuch, D., Irwin, L.N., 2004, *Life in the Universe: Expectations and Constraints*: Springer, Berlin
- Schulze-Makuch D., J.M. Dohm, C. Fan, A.G. Fairen, J.A.P. Rodriguez, V.R. Baker and W. Fink, 2007, Exploration of hydrothermal targets on Mars, *Icarus*, 189, p. 308-324
- Schwenzer, S.P., Kring, D.A., 2008, Inferred impact-generated hydrothermal mineral assemblages in basaltic regions of Mars, In *Lunar and Planetary Institute Science Conference Abstracts*, vol. 39, Abstract no. 1817
- Schwenzer, S.P., Kring, D.A., 2009, Impact-generated hydrothermal alteration on Mars: Clay minerals, oxides, zeolites, and more, In *Lunar and Planetary Institute Science Conference Abstracts*, vol. 40, Abstract no. 1421
- Schwenzer, S.P., Kring, D.A., 2010, Evaluating the Effect of Sulfur on Alteration Assemblages in Impact Cratered Terrains on Mars, 41st Lunar and Planetary Science Conference, Abstract no. 1533
- Scott B.J., 1995, Cyclic activity in the crater lakes of Waimangu Hydrothermal System, New Zealand, *Geothermics* 23, No 5/6, p. 555-572
- Scott, D. H., and Tanaka, K.L., 1982, Ignimbrites of Amazonis Planitia Region of Mars, *J. Geophys. Res.*, 87(B2), p. 1179-1190, doi:10.1029/JB087iB02p01179
- Scott, D.H and Tanaka, K.L., 1986, Geologic map of the western equatorial region of Mars. USGS Misc. Invest. Ser. Map I-1802-A
- Scott, D.H., Dohm J., and Applebee D., 1993, Geologic map of science study area 8, Apollinaris Patera region of Mars. USGS maps, map I-2351
- Scott, D.H., Dohm, J.M., Rice, J.W.Jr., 1995, Map of Mars showing channels and possible paleolake basins, USGS Misc. Inv. Ser. Map I-2461
- Seibert N. M. and Kargel J. S., 2001, Small-scale Martian Polygonal Terrain: Implications for Liquid Surface Water. *Geophys. Res. Lett.*, 28, NO. 5, p. 899-902
- Seu, R., et al., 2007, SHARAD sounding radar on the Mars Reconnaissance Orbiter, *J. Geophys. Res.*, 112, E05S05, doi:10.1029/2006JE002745

- Sheridan M.F., and K.H. Wohletz, 1983, Hydrovolcanism: Basic considerations and review. *Journal of Volcanology and Geothermal Research*, 17, p. 1-29
- Shock, E.L., 1996, Hydrothermal systems as environments for the emergence of life. In: *Evolution of hydrothermal ecosystems on Earth (and Mars?)*: Wiley, Chichester (Ciba Foundation Symposium 202) p. 40-60
- Skinner J.A. Jr. and K.L. Tanaka, 2007, Evidence for and implications of sedimentary diapirism and mud volcanism in the southern Utopia highland-lowland boundary plain, Mars, *Icarus* 186, p. 41-59
- Smith, D.E., and 23 colleagues, 2001, Mars Orbiter Laser Altimeter: Experiment summary after the first year of global mapping of Mars, *J. Geophys. Res.* 106, p. 23689-23722
- Soare R. J., , D. M. Burr, and J. M. Wan Bun Tseung, 2005, Possible pingos and a periglacial landscape in northwest Utopia Planitia, *Icarus*, 174, Issue 2, p. 373-382
- Soare R. J., Osinski G. R., and Roehm C. L., 2008, Thermokarst lakes and ponds on Mars in the very recent (late Amazonian) past. *Earth & Planet. Sci. Lett.* 272, p. 382-393
- Squyres S. W., 1989, Urey Prize Lecture: Water on Mars, *Icarus* 79, p. 229-288
- Squyres, S.W., and 49 colleagues, 2004, The Spirit Rover's Athena Science Investigation at Gusev Crater, Mars, *Science*, 305, p. 794-799
- Squyres S.W., et al., 2006, Two years at Meridiani Planum: Results from the Opportunity Rover, *Science*, 313, p. 1403-1407
- Tanaka, K. L., and G. J. Leonard, 1995, Geology and landscape evolution of the Hellas region of Mars, *J. Geophys. Res.*, 100(E3), p. 5407-5432
- Tanaka, K.L., Dohm, J.M., Lias, J.H., Hare, T.M., 1998, Erosional valleys in the Thaumasia region of Mars: Hydrothermal and seismic origins: *J. Geophys. Res.*, v. 103, p. 31,407-31,419
- Tanaka, K.L., Skinner, J.A.Jr., Hare, T.M., 2005, Geologic map of the northern plains of Mars, U.S. Geological Survey Scientific Investigations Map SIM-2888
- Taylor, G. J., and 26 colleagues, 2006, Variations in K/Th on Mars, *J. Geophys. Res.*, 111112, E03S06, doi:10.1029/2006JE002676
- Taylor H.P., 1997, Oxygen and hydrogen isotope relationships in hydrothermal mineral deposits. In Barnes H.L. (ed) *geochemistry of hydrothermal ore deposits*, 3rd edn., John Wiley & Sons, p. 229-302
- Toramaru, A., and T. Matsumoto, 2004, Columnar joint morphology and cooling rate: A starch-water mixture experiment, *J. Geophys. Res.*, 109, B02205, doi:10.1029/2003JB002686

- Towner G.D., 1987, The Mechanics of Cracking of Drying Clay. *J. Agric. Engng.*, 36, p. 115-124
- Valentino, G.M., Cortecchi, G., Franco, E., Stanzione, D., 1999, Chemical and isotopic compositions of minerals and waters from Campi Flegrei volcanic system, Naples, Italy: *J. Volc. Geoth. Res.*, v. 91, p. 329-344
- Vandemeulebrouck, J., D. Stemmelen, T. Hurst, and J. Grangeon, 2005, Analogue modeling of instabilities in crater lake hydrothermal systems, *J. Geophys. Res.*, 110, B02212, doi:10.1029/2003JB002794
- Varekamp, J. C., 2004, Copahue Volcano: A modern terrestrial analog for the Opportunity landing site. *Eos*, 85, no. 41, 12, p. 401-407
- Varekamp J.C., G.B. Pasternack and Jr Rowe, 2000, Volcanic lake systematics II. Chemical constraints, *J. Volcanol. Geotherm. Res.* 97 (2000), p. 161-179
- Varekamp, J.C., Ouimette, A. and Kreulen. R., 2004, The magmato-hydrothermal system of Copahue volcano, Argentina. *Proceedings of the 11th Water Rock Interaction Symposium*, (eds Wanty, R.B. & Seal, R.R.), v.1, p. 215-218
- Versh, E., Kirsimäe K., Jõelett, A., and Plado J., 2005, Cooling of the Kärddla impact crater: I. The mineral paragenetic sequence observation, *Meteoritics and Planetary Science*, 40, p. 3, doi: 10.1111/j.1945-5100.2005.tb00361.x
- Warren-Rhodes, K., et al., 2007, Searching for microbial life remotely: Satellite-to-rover habitat mapping in the Atacama Desert, Chile: *J. Geophys. Res.*, v. 112, G04S05, doi:10.1029/2006JG000283
- Watters T.R., and 12 colleagues, 2007, Radar Sounding of the Medusa Fossae Formation Mars: Equatorial Ice or Dry, Low-Density Deposits?, *Science*, 318, p. 1125-1128, doi: 10.1126/science.1148112
- Wharton R. A. Jr., J. M. Crosby, C. P. McKay and J. Rice, Jr., 1995, Paleolakes on Mars. *J. Paleolimnology* 13, p. 267-283
- Willden R. and Don R. Mabey, 1961, Giant Desiccation Fissures on the Black Rock and Smoke Creek Deserts, Nevada. *Science* 133, 1359, DOI: 10.1126/science.133.3461.1359
- Williams P., C. Pigram and D. Dow, 1984, Melange production and the importance of shale diapirism in accretionary terrains. *Nature* 309, p. 145-146
- Williams-Jones, A.E., Heinrich, C.A., 2005, 100th Anniversary Special Paper: Vapor transport of metals and the formation of magmatic-hydrothermal ore deposits, *Economic Geology* 100, n.7, p. 1287-1312
- Wiseman, S. M., et al., 2008, Phyllosilicate and sulfate-hematite deposits within Miyamoto crater in southern Sinus Meridiani, Mars, *Geophys. Res. Lett.*, 35, L19204, doi:10.1029/2008GL035363

- Wray, J. J., B. L. Ehlmann, S. W. Squyres, J. F. Mustard, and R. L. Kirk, 2008, Compositional stratigraphy of clay-bearing layered deposits at Mawrth Vallis, Mars, *Geophys. Res. Lett.*, 35, L12202, doi:10.1029/2008GL034385
- Wray, J. J., E. Z. Noe Dobrea, R. E. Arvidson, S. M. Wiseman, S. W. Squyres, A. S. McEwen, J. F. Mustard, and S. L. Murchie, 2009, Phyllosilicates and sulfates at Endeavour Crater, Meridiani Planum, Mars, *Geophys. Res. Lett.*, 36, L21201, doi:10.1029/2009GL040734
- Yen A.S., et al., 2008, Hydrothermal processes at Gusev Crater: an evaluation of Paso Robles class soils, *J. Geophys. Res.*, 113, doi: 10.1029/2007JE002987
- Yoshikawa K., (2000), Contraction cracking and ice wedge polygons in Mars. Mars Polar Science workshop. Abstract no. 4045
- Zürcher, L. and Kring, D.A., 2004, Hydrothermal alteration in the core of the Yaxcopoil-1 borehole Chicxulub impact structure, Mexico, *Meteoritics and Planetary Science* 39, p. 1199-1221, doi: 10.1111/j.1945-5100.2004.tb01137.x

Publications

Peer-reviewed Publications

- **El Maarry M.R.**, J.M. Dohm, G. Marzo, R. Ferguson, E. Heggy, W. Goetz, A. Pack, and W.J. Markiewicz, 2010, Searching for evidence of hydrothermal activity at Apollinaris Patera, Mars, Icarus, submitted
- **El Maarry M.R.**, Markiewicz W.J., Mellon M., Goetz., Dohm J., and Pack A., 2010, Crater Floor Polygons : Desiccation Patterns of Ancient Lakes on Mars?, J. Geophys. Res., doi:10.1029/2010JE003609
- **El Maarry M.R.**, Gasnault O., Toplis M., Baratoux D., Dohm J. M., Newsom H. E., Boynton W. V., Karunatillake S. 2009, Chemical composition of Martian volcanics at Tharsis from gamma-ray data: New constraints on the depth of the mantle source region, Journal of Volcanology and Geothermal Research. Volume 185, p. 116-122. Tectonic and volcanic history of the Tharsis province, Mars
- Karunatillake S., J. J. Wray, S. W. Squyres, G. J. Taylor, O. Gasnault, S. M. McLennan, W. Boynton, **M.R. El Maarry**, and J. M. Dohm, 2009, Chemically striking regions on Mars and Stealth revisited, J. Geophys. Res., 114, E12001
- Goetz W., W.T. Pike, S.F. Hviid, M.B. Madsen, R.V. Morris, M.H. Hecht, U. Staufer, E. Hemmig, J. Marshall, J.M. Morookian, D. Parrat, H. Sykulska, S. Vijendran, B.J. Bos, **M.R. El Maarry**, H.U. Keller, R. Kramm, W.J. Markiewicz, L. Drube, K. Leer, D. Blaney, R.E. Arvidson, J.F. Bell III, R. Reynolds, P.H. Smith, P. Woida, R. Woida, and R. Tanner, 2009, Microscopy analysis of soils at the Phoenix landing site, Mars: Classification of soil particles and description of their optical and magnetic properties, J. Geophys. Res., 115, E00E22, doi:10.1029/2009JE003437

Conference and meeting proceedings

- **El Maarry M.R.**, J. Kodikara, W. Markiewicz and W. Goetz. Numerical modeling of a desiccation mechanism for formation of Crater Floor Polygons on Mars, American Geophysical Union Fall meeting, 2010, abstract no. 965832
- **El Maarry M.R.**, W. Markiewicz, J. Kodikara, W. Goetz, and J. Dohm, Numerical modeling of a desiccation hypothesis for Crater Floor Polygons on Mars, Europlanet Science Congress, 2010

- **El Maarry M.R.**, W. Markiewicz, M. Mellon, W. Goetz, Crater Floor Polygons (CFPs): Signs of desiccated Paleolakes on Mars?, 41st Lunar and Planetary Science Conference, 2010
- **El Maarry M.R.**, W. Markiewicz, M. Mellon, W. Goetz. Crater Floor Polygons: Desiccation Patterns of Crater Paleolakes on Mars?, Europlanet Science Conference, 2009, 13-18 Sep, 2009. Abstract no. 222
- **El Maarry M.R.**, W. Markiewicz, M. Mellon, W. Goetz, Crater Floor Polygons: Desiccation Patterns of Crater Paleolakes?, Workshop on Modeling Martian Hydrous Environments, June 1-3, 2009 in Houston, Texas, LPI Contribution 1482, p. 25-26
- **El Maarry M.R.**, and Gasnault O., A Preliminary Assessment of the Role of Impact Craters in Forming Hydrous Minerals on the Surface of Mars. 40th Lunar and Planetary Science Conference, 2009, abstract no. 1883
- **El Maarry M.R.**, and Sierks H., Geological, Geochemical and Engineering Considerations for Choosing a Landing Site on the Jovian Moon Europa. 40th Lunar and Planetary Science Conference, 2009
- **El Maarry M.R.** and the Phoenix team, Preliminary Geology Results from the Phoenix Mission to Mars, Cairo University, Dec, 2008 (Invited)
- **El Maarry M.R.** and the Phoenix team, Preliminary Results from the Phoenix Mission to Mars, Student Planetary Workshop, ESTEC, 9-10 Oct, 2008
- **El Maarry M.R.**, Toplis M., Gasnault O, and Baratoux D., Gamma-Ray Data of the Tharsis Region, Mars: A Signature of Partial Melting of the Martian Mantle?, 39th Lunar and Planetary Science Conference, 2008
- W. Goetz, S. F., Hviid, M. B. Madsen, W. T. Pike, M. H. Hecht, R. V. Morris, K. Leer, L. Drube, H. Sykulska, K. E. Herkenhoff, N. A. Cabrol, **M.R. El Maarry**, H. U. Keller, W. J. Markiewicz, R. E. Arvidson, and P. H. Smith, Comparison of some Phoenix and Gusev soil types: Inferences on possible origins and global distribution, 41st Lunar and Planetary Science Conference, 2010
- H. U. Keller, **M.R. El Maarry**, W. Goetz, S. F. Hviid, W. J. Markiewicz, M. Hecht, M. Madsen, M. Mellon, D. Ming, W. T. Pike, P. Smith, U. Staufer, and A. Zent, Physical Properties of the Icy Soil at the Phoenix Landing Site, 40th Lunar and Planetary Science Conference, 2009
- Karunatillake S., S. W. Squyres, J. J. Wray, G. J. Taylor, O. Gasnault, S. M. McLennan, W. Boynton, **M.R. El Maarry**, and J. M. Dohm, Chemically striking Martian regions and stealth revisited, 40th Lunar and Planetary Science Conference, 2009
- Keller, H., Markiewicz, W. J., Hviid, S. F., Goetz, W., Mellon, M. T., **El Maarry M.R.**, Madsen, M. B., Smith, P., Pike, W., Zent, A., Hecht, M. H., Ming, D., Staufer, U., Physical Properties of the Icy Soil at the Phoenix Landing Site. American Geophysical Union, Fall Meeting 2008, abstract no. U14A-06

- Markiewicz W. J., Keller H. U., Kossacki K. J., Mellon M. T., Stubbe H. F., Bos B. J., Woida R., Drube L., Leer K., Madsen M. B., Goetz W., **El Maarry M.R.**, Smith P., Sublimation of Exposed Snow Queen Surface Water Ice as Observed by the Phoenix Mars Lander, American Geophysical Union, Fall Meeting 2008, abstract no. U11B-0026
- Toplis M., **M.R. El Maarry**, Baratoux D., Gasnault O., Pinet, P. C., Are Small Differences in Phosphorous Content Responsible for Large Differences in the Composition of Terrestrial and Martian Magmatic Rocks?, 39th Lunar and Planetary Science Conference, 2008

Acknowledgements

There are many people in my life who must take credit for making this work possible, exciting, and a fantastic experience overall. First, I thank God for giving me the strength and perseverance to achieve my childhood dreams and a goal I set to myself when I finished high school. I am grateful for two men: Sven Molin and Dieter Schmitt; the coordinators of the Space Master program and the IMPRS respectively, for the opportunity they have given me. I would like to thank my supervisors in the Institute and Göttingen University, respectively; Walter Goetz and Andreas Pack who have been a great help for the last 3 years keeping me focused on the job at hand and offering guidance whenever needed.

This work would not have been possible without the help of some remarkable scientists and mentors. I would like to show my gratitude to James Dohm for being my Geology mentor and on top of that a very good friend for the past 4 years, Wojtek Markiewicz for all the help and the constructive discussions regarding the physical modeling of CFPs and the numerical model for desiccation, Olivier Gasnault, my Masters supervisor, for his continuing help even throughout my PhD studies, Horst Owe Keller for the lively discussions, and Stubbe Hviid for help with IDL. Additionally, I'm indebted to the co-authors on my publications who have truly enriched them, and I am grateful for all the things I learnt from all of them. I thank Ceci, Daniel, and Roberto for their help with Latex and proof-reading the thesis. I also thank the library staff at the institute for all their help throughout the three years. Finally, a warm thanks to all the members of the Phoenix team for making me part of their mission at the start of my studies.

Surely, considering the delights Lindau has to offer, the past 3 years would have been way less tolerable without the friends I have made here. Ceci, Cleme, Elias, Luca! Thank you for the laughter and fun we've shared in this time (and in the case of Ceci and Elias, for the many rides to the station, for inviting me to your wedding, and the countless weekend get-togethers). An honorable mention goes to the loony Italian-Artist-Geologist Roberto (Bob) Bugiolacchi. Thank you for co-holding the geological fort in the institute, and for your light-hearted (let's leave it there!) view of life. I would like to thank all the students for nominating me as a student representative! I hope I have served You all in the best way possible, my dancing buddies; Maria and Philippe for the dancing nights, and the competitive football bunch, Wieland, Yeon joo, Megha, Jeff, Naja, Rado, Juan Jo, Ray, Hana, and the old guards, Sufianne, Michao, Jean Baptiste for keeping me in shape! ... No guys, I haven't forgotten you of course; the Italian/International Coffee group! Anne, Chris, Daniel, Dave, Jonas, Judith, Manu, Peter, Richard, Shahin, Tijmen. Thank you all for making the 13:00 to 13:30 (13:45 on Fridays!) time slot absolutely fun and an excuse to check the most bizarre Wikipedia links!

In the end, I owe my deepest gratitude to my family for supporting me all this time and believing in me. Being away from them has been my worst regret. Mom, Dad, Sis, Aunt,

Acknowledgements

and Uncle, I miss you all the time. This work is dedicated to You! Last but certainly, in no way the least, my sweetheart and softer half; Marmori. You have been responsible for everything good in my life in the past 3 and half years, having lent me your USB stick to use at my interview at the MPS, agreeing to come here and share your life with me (no small feat), and being absolutely supportive and understanding of my constant and prolonged absence at work. I hope I am worth the wait.

Curriculum Vitae

Studium

- **M.Sc.**, Université Paul Sabatier in Toulouse, Frankreich, Astrophysik und Planetologie, 2007
- **M.Sc.**, Luleå Technische Universität in Schweden, Space Technology, 2007
- **B.A.**, Kairo Universität, Ägypten, Doppelabschluss in Geologie und Chemie, 2002

Persönliche Daten

- **Geburtsdatum:** 16 Januar 1981
- **Geburtsort:** Kairo, Ägypten
- **Staatsangehörigkeit:** Ägyptisch
- **Familienstand:** Verheiratet